THE UNIVERSITY OF
SYDNEY

Using Asteroseismology to Determine Membership of Stellar Clusters Observed by the *Kepler* Mission

Beau R. Bellamy

A thesis submitted for the degree of
Masters of Science
at the University of Sydney

June 18, 2015

Abstract

If we can measure the speed of sound in a gas, we have information about the pressure and density of that gas. From the equation of state, we can constrain the temperature and chemical composition. Therefore, by measuring the sound speed in stars we can deduce these same characteristics of the star being measured. The goal of asteroseismology is to use oscillations to measure this sound speed throughout the star to determine these fundamental stellar parameters. Asteroseismology accomplishes this by extracting the oscillation frequencies of the sound at the stellar surface, and combining this with models to infer the sound speed and density inside the star.

The *Kepler* space telescope has initiated a revolution in asteroseismology. The *Kepler* mission is a NASA space-based photometric telescope, designed to detect Earth-size planets around Sun-like stars. *Kepler* has observed one patch of sky for a continuous four year period. The high photometric precision of the data in conjunction with the long time span also makes it ideal for measuring the frequencies of the sound-wave induced by oscillations at the stellar surface.

I use a new technique to determine the cluster membership of red giant stars in two open clusters using asteroseismology. By determining the oscillation frequencies of a number of red giants in the region of two clusters in the *Kepler* field, I can determine whether they are consistent with membership of the cluster or are field stars in the foreground or background. This thesis focuses on the evolved stars, which have left the hydrogen-core burning phase on the main sequence to become hydrogen shell-burning subgiants, or red giants. I was able to use the *Kepler* long-cadence (29.4 min) data to measure the oscillation frequencies of the red giants, and thus infer their fundamental stellar parameters.

Stars in a cluster are believed to share a common age and initial composition, being formed from the same interstellar cloud. This allows for membership to be inferred from photometric studies by using models of isochrones in a color-magnitude diagram. As a result, this technique is dependent on knowing distance and interstellar extinction. Alternatively, the common space velocity can also be used to determine membership status, however, this relies on the field stars not randomly aligning with the cluster motion. Recently, Stello et al. (2010b) introduced a new technique based on asteroseismology to determine cluster membership that is dependent only on the internal properties of the stars.

I detect the oscillation frequencies to measure the *frequency of maximum oscillation power*, $\nu_{\rm max}$ and the *large frequency separation*, $\Delta\nu$. These parameters are related to surface gravity and the mean density of the star respectively, and are therefore known to scale with the M, L and $T_{\rm eff}$ (where M is the mass, L is the luminosity and $T_{\rm eff}$ is the surface temperature) of the star (Ulrich 1986; Kjeldsen & Bedding 1995). The common initial conditions of the cluster allow us to compare the parameters of individual stars in the vicinity of the cluster with the mean of the cluster. A ratio of 1.0 for the measured to scaled parameter indicates a likely member of the cluster independent of distance or interstellar absorption.

I analysed over 400 red giant stars in the vicinity of two clusters in the *Kepler* field of view, NGC 6791 and NGC 6819. By measuring the asteroseismic parameters of each star and comparing them with the solar scaled values, I was able to confirm the members of Stello et al. (2011b) and to identify 45 new red giant members distributed over the two clusters. This has increased the red giant population by almost 40% for NGC 6791 and almost 10% for NGC 6819, which will allow stellar evolution models to be constrained.

Statement of originality

I, Beau Bellamy, hereby declare that all work presented in this thesis is based on research conducted by me during my Masters candidature at the Sydney Institute for Astronomy, University of Sydney, from March 2013 to June 18, 2015. I declare that none of this work has been submitted to obtain another degree at this or any other university. All work presented in this thesis was performed by me except where explicitly indicated. To the best of my knowledge, this thesis contains no copy or paraphrase of work by others, except where clearly acknowledged in the text.

June 18, 2015

Beau R. Bellamy | Date

Publications

The following publications have benefited from work presented in this thesis:

Bellamy B., Stello D., 2013, Correcting for the jumps in Kepler light curves of M giants. Poster presented at Kepler Asteroseismic Science Consortium 6, Sydney, Australia

Bellamy B., Stello D., 2014, New seismic members in NGC 6791 and NGC 6819. Poster presented at Kepler Asteroseismic Science Consortium 7, Toulouse, France

Banyai E., Kiss L. L., Bedding T. R., Bellamy B. et al. Variability of M giant stars based on Kepler photometry: General characteristics, 2013, MNRAS, 436, 1576

Stello D., Compton D., Bedding T. R., Bellamy B. et al. Non-radial oscillations in M-giant Semi-regular Variables: Stellar Models and Kepler Observations, 2014, ApJ, 788, L10

García R. A., Mathur S., Pires S., Bellamy B. et al. Impact on asteroseismic analysis of regular gaps in Kepler data, 2014, A&A, 568, A10

Kuehn C. A., Drury J., Stello D., Bellamy B. et al., 2014, in IAU Symposium, Vol. 301, IAU Symposium, Guzik J. A., Chaplin W. J., Handler G., Pigulski A., eds., Photometry using Kepler superstamps of open clusters NGC 6791 & NGC 6819, pp. 445-446

Acknowledgments

Firstly, I would like to thank my supervisor, Dennis Stello who has provided support and advice on all aspects of my research, as well as career development. As a mature age postgrad student, I have appreciated your honesty and guidance throughout my candidature. I would also like to express my gratitude to my associate supervisor, Tim Bedding for being there at the beginning. The enthusiasm and excitement you show about science is contagious. I also want to thank Tara Murphy and Sean Farrell who gave me much needed advice on my career.

Collaboration is a significant part of professional astronomy and I was no exception. I have been a part of a large group of international astronomers who have influenced the direction of research. There are far too many people to mention individually, but the Kepler Asteroseismic Science Consortium (KASC) has been the textbook example of how large collaborations should be run. Particular thanks to Hans Kjeldsen, Jørgen Christensen-Dalsgaard and Bill Chaplin. The *Kepler* Science team has provided us with the most outstanding asteroseismic data. Thank you to all involved.

I would like to thank the members of the Stellar Astrophysics Centre in Aarhus for the support and opportunity to travel to Toulouse, France for a conference. I had a wonderful experience and discussed my research with others, an opportunity that I may not have had otherwise. Their scientific and financial support have allowed me to get the most out of my Masters research.

I would like to thank Rafael García for your insight on correcting and aligning the timeseries. I would also like to thank Daniel Huber especially, who spent many months writing the SYD pipeline and hours more explaining it to me so I could understand it enough to make modifications without breaking it.

Thank you to all my friends in the School of Physics. Due to the open plan office, we weren't confined to a stuffy office and it allowed for many heated discussions, usually nothing to do with science. Many of these gave a well needed distraction to maintain my sanity. Thanks to Craig Anderson, John Ching, Sarah Reeves, Barnaby Norris, Ben Pope, Joe Callingham, Charles Kuehn, Othman Benoumar, Simon Murphy, Tim White, Jason Drury, and not to forget Chris Betters who is going through the writing up stage with a thesis beard, good luck Chris. I can't wait to see how it goes. I definitely wont forget Jane Kaczmarek and Pascal Elahi for twisting my arm to have a beer when things weren't working out. Your friendship and expertise has been appreciated.

A special thanks to two very important people. Firstly my girlfriend Louise, thanks for the support you have given me. I know it must have been hard dating a guy at this age, that is still studying while working two or three part time jobs to pay the bills. My research and jobs didn't leave much time for you, and I thank you for your patience, love and support while I chase a dream of scientific research. I'd also like to thank Leah, a great friend who always knows how to deal with a frustrated uni student, because she is one herself. Your distractions and insight into a different realm of science gave me what I needed, when I needed it.

Finally, to my family, especially Mum and Dad. You have always been supportive of me and the direction I choose in life. I appreciate the sacrifices you have made to allow me to get here now, I especially want to thank you for letting me move back home for a few months after you thought you had finally got rid of me. The love of a parent will never fade, and I thank you for that.

Contents

Chapter 1

Background

1.1 Introduction

> *Space is big. You just won't believe how vastly, hugely, mind-bogglingly big it is. I mean, you may think it's a long way down the road to the drug store, but that's just peanuts to space.* - Douglas Adams

Everyone will, at one point in their lives, look up at the night sky and contemplate the *mind-bogglingly* vastness of space and the universe, what that means for them, and how their everyday lives are affected. Some will answer by saying it doesn't affect their lives at all. That the stars, galaxies, and everything else are too far away to make any difference. Others have considered this question in more detail, how understanding the evolution of the universe may in turn, affect us directly. One might say that we are nothing without the stars, as the atoms and molecules that form our body were created in a massive supernova millions of years ago. So understanding the stars and their evolution is vital to understanding our own existence.

The thousands of stars visible to the naked eye are but a minuscule fraction of the total number of stars in our own galaxy, let alone the universe. These stars may appear to be indistinguishable from one other, but this is far from the truth. The stars basic properties are determined at birth by its initial conditions. The initial chemical composition and mass of a star are, therefore, a major factor in its evolution.

Knowledge of the complex processes that go on within a star can inform other fields of astrophysics, from exoplanets to cosmology. Most exoplanets have been observed indirectly through observations of their host stars. By understanding the properties of the host star, we can provide vital information on the properties of the planets, from their size and density to whether they are in the so called habitable zone. The age of the star and therefore the planets are important for the possibility of life evolving on these planets. Many of the oldest stars are a significant fraction of the age of the universe, providing a time capsule into the conditions of the early universe, which is a significant tool for cosmology and galactic archeology (Freeman & Bland-Hawthorn 2002). Most stars form in groups or clusters and thus have common ages and initial compositions. These common properties enable the cluster to be treated as an ensemble, providing a unique laboratory for probing stellar evolutionary theories. Individual stellar properties within these clusters provide snapshots ("isochrone", (Monteiro, Dias & Caetano 2010; Oliveira et al. 2013)) of stellar evolution at the age of the cluster (Stello et al. 2010a; Basu et al. 2011), based on differing initial conditions, i.e mass.

Direct measurement of the mass and radius of a star are generally limited to the nearest and brightest stars. For these, we can determine the masses of stars in nearby binary systems using Kepler's Third Law. The radius of nearby stars can be measured using parallax measurements and interferometry. The temperature and chemical composition at the surface can be measured using spectroscopy through analysis of the absorption lines. For other stellar characteristics, such as mixing and internal properties, we generally rely on stellar models. These observations are compared to the models to provide insight into the physical processes within the star. When the models and observations do not match, the stellar models are iteratively improved upon, as the models are reconciled with observations. We are then able to constrain the models using accurate parameters for the fundamental properties.

Even with improvements made to the models we are generally limited to the global properties, such as mass, radius, or surface properties like effective temperature and chemical composition. What about the stellar interior? Until recently we lacked the observational evidence to support our understanding of the physical processes that go on deep inside stars. Eddington considered this problem in 1926 in "The Internal Constitution of the Stars":

> *At first sight it would seem that the deep interior of the Sun is less accessible to scientific investigation than any other region of the universe. Our telescopes may probe farther and farther into the depths of space, but how can we ever obtain certain knowledge of that which is hidden behind substantial barriers? What appliance can pierce the outer layers of a star and test the conditions within?* (Eddington 1926)

When Eddington wrote this, he did not have such a pessimistic view that the science of the internal structure of the star was inaccessible. He believed that it would be possible to interpret the gravitational fields and radiant energy from the interior to infer the interior properties of the star. However, he was not satisfied with theory providing the answers without direct observational evidence. Eddington warned against placing too much faith in theoretical inferences that are detached from observational tests. Had he been alive today, he would be astounded to learn that there is a way we can see beyond the substantial barriers of the outer layers of a star. Asteroseismology is the answer to the direct observational evidence Eddington sought.

Asteroseismology (from Greek aster = *star* +seismos = *earthquake* +logos = *reasoning*) is the study of the internal structure of stars through their oscillations. The properties of these oscillations depend on the internal structure of the star producing them. Therefore the oscillations can be used to probe the internal structure, providing Eddington with the *appliance* with which to pierce the outer layers of the star.

Asteroseismology is analogous to seismology of the Earth, geoseismology. The sound and other waves generated by earthquakes traveling through the Earth, and are measured by a seismometer. Knowledge of details of the Earths interior, such as the solid iron inner core, the liquid iron and sulfur outer core, and the mantle which consists of molten magma are a direct result of measuring the varying velocity of the waves as they travel through the Earth. With asteroseismology, we measure the frequencies of oscillations caused by the sound waves inside the star to infer details about its structure.

In this thesis, I am concerned principally with asteroseismology of cool, low mass stars which oscillate due to convection. Observing these oscillations has typically been difficult due to the low amplitude of these oscillations. Until recently, only a handful of stars have had clear detections of solar-like oscillations, i.e. oscillation driven by convection, (Bedding & Kjeldsen 2003). The number of stars with detected solar-like oscillations has exploded in a revolution for asteroseismology due to the launch of the space missions CoRoT (Convection Rotation and planetary

Transits (Michel et al. 2008; De Ridder et al. 2009)) and *Kepler* (Gilliland et al. 2010; Chaplin et al. 2011). Thousands of stars are now being analysed, individually and in clusters, to gain further understanding of the internal physics of stars. This thesis aims to show how asteroseismology can be applied to cluster stars to identify membership to the clusters in order to help constrain the evolutionary theories.

1.2 Stellar Evolution

1.2.1 Pre-Main Sequence

Stellar evolution begins with a molecular cloud under a gravitational collapse forming an optically thick sphere of gas. The temperature of the gas increases, leading to an increase in pressure, mainly in the core, which will resist further collapse. At this point the gas cloud forms a protostar under hydrostatic equilibrium reaching a maximum of $8M_{\odot}$, where $M_{\odot}$ is the mass of the Sun (Ryan & Norton 2010), which consists mainly of hydrogen and enters the pre-main sequence phase. These stars will travel down the *Hayashi track* in the Hertzsprung-Russel (HR) diagram (the near vertical blue lines seen in Figure 1.1), becoming significantly less luminous while maintaining a roughly constant temperature as they contract further. This continues until a radiative zone forms and the star turns off the Hayashi track and on to the *Henyey track*, the near horizontal lines seen in Figure 1.1, of near constant luminosity and increasing temperature. As the temperature in the core continues to increase, energy begins to be transported by radiation. Contraction continues, increasing the mass of the radiative region, until most of the star becomes radiative. The core temperature increases to a point where nuclear fusion begins to increase the luminosity. Some of the hydrogen burning reactions of the proton-proton, (p-p) chain begin at a few million degrees well before the complete chain is turned on. Contraction ceases and the p-p chain is turned on completely forming helium-4 (^{4}He) in the core. The protostar soon settles into an equilibrium as it is born on to the *zero-age main sequence* (ZAMS), see Figure 1.2, point 1 on the $1.7M_{\odot}$ track.

1.2.2 Main Sequence

During the main sequence stage, the star is in a stable equilibrium while it burns hydrogen in the core. The structure of the star changes from nuclear reactions in the core which slowly modify the chemical composition on the nuclear time scale. Approximately 90% of its life will be spent on the main sequence. The actual amount of time spent on the main sequence will depend on the initial mass of the star, and hence the available fuel and energy production process. In the lower main sequence stars, i.e. $< 1.5M_{\odot}$ (Karttunen et al. 2007), the p-p chain discussed above is the dominant form of energy production, while in the upper main sequence, the energy produced will be dominated by the CNO cycle (Salaris & Cassisi 2005), which is a catalytic cycle using carbon, nitrogen and oxygen isotopes. At higher temperatures, the CNO cycle is more efficient than the p-p chain process where the CNO cycle dominates and becomes self sustaining at $\sim$15 million K (Bethe 1939; Karttunen et al. 2007). While the lower main sequence stars are dominated by the p-p chain, the CNO cycle will produce some fraction of the energy, approximately 1.7% of ^{4}He for the Sun (Ryan & Norton 2010).

The core in a lower main sequence star is radiative due to the relative thermal stability of the p-p chain reaction, compared to the CNO cycle. Since there is no mixing in the core, the hydrogen abundance increases outwards because the hydrogen is consumed at the centre through the nuclear reactions. The lower temperature in the outer layers of the star means the opacity is

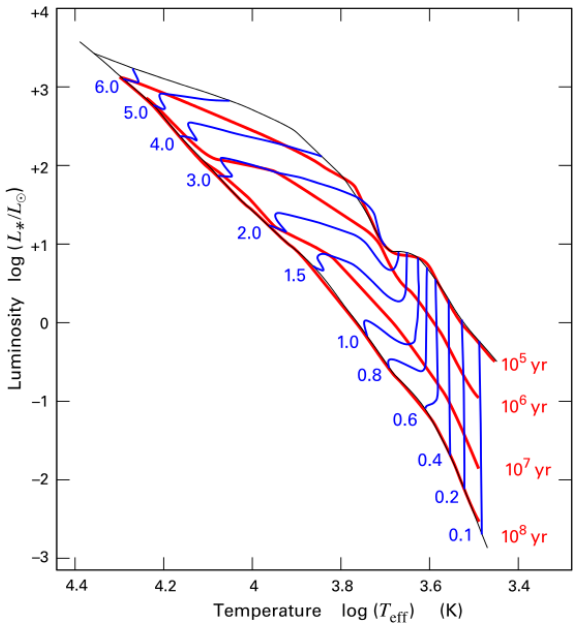

Figure 1.1: Hertzsprung Russel diagram showing the pre main sequence tracks (blue lines) of stars ranging from $0.1M_\odot$ to $6M_\odot$. Isochrones (red lines) indicate the ages of the stars that lie along the line. Low mass stars have nearly vertical evolution track to the HR diagram down the Hayashi track. The more massive stars will bend onto the Henyey track before reaching the main sequence. The most massive stars will be born directly on the Henyey track.
Figure credit: (Stahler & Palla 2004)

high and energy can no longer be transported through radiation. At this point, the energy is also transported via convection.

Figure 1.2 shows the evolutionary tracks after the main sequence stage of four stellar models of varying mass. I will follow the model that is consistent with a cool, low mass, $1.7M_\odot$ star. As the star converts the hydrogen to helium, it will slowly move up along the main sequence, becoming slightly brighter and cooler. Material mixing allows the convective core to maintain a uniform decrease in hydrogen abundance with time within the convective region. Outside the core, the energy is transported by radiation where no nuclear reactions take place. As the hydrogen is consumed in the core, the core mass will gradually diminish as it moves to the upper right of the HR diagram from point 1 to point 2 in Figure 1.2, where the luminosity increases and the surface temperature decreases. Here, the core of the star begins to shrink rapidly as the central supply of hydrogen is exhausted. The star quickly moves to the upper left as the surface temperature increases, creating the characteristic hook feature, shown at point 3 in Figure 1.2. The contraction of the core increases the temperature in the hydrogen shell just outside the core and eventually burning will set in, in a shell surrounding the core at point 3.

1.2.3 Subgiant and Giant Phase

As the star leaves the main sequence, the hydrogen burning continues in a shell surrounding the helium core, increasing the mass of the core and leading to an expanding envelope. This expansion reduces the temperature of the envelop and helps to maintain an almost constant luminosity, as it moves to the right on the HR diagram through the sub giant phase, from point 3 towards point 4 on Figure 1.2.

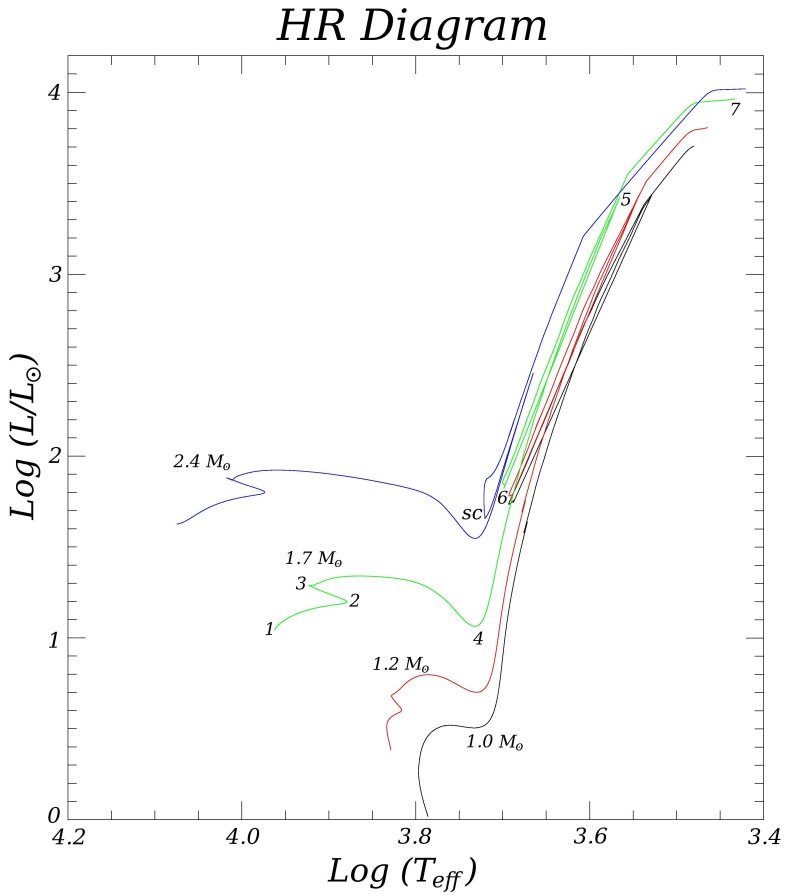

Figure 1.2: This Hertzsprung-Russel diagram indicates four stellar evolutionary tracks that span the range of masses that are representative of the clusters discussed here. The tracks begin as they start the main sequence, the numbers following the $1.7M_{\odot}$ track indicate significant stages in the stars evolution, which are discussed in the text. Model tracks were obtained from BaSTI (http://basti.oa-teramo.inaf.it/index.html)

The star then approaches the Hayashi track as the convective envelope continues to expand. This causes the star to climb the Hayashi track as the temperature remains almost constant, as seen in moving from point 4 to point 5 in Figure 1.2. The star has now reached the *red giant branch* (RGB). The core density of a low mass star, $< 2.3M_{\odot}$, increases as the core mass grows. The core will eventually become degenerate and have a uniform temperature due to the high thermal conductivity of the degenerate gas. If the star is massive enough, i.e M $> 0.26M_{\odot}$, the temperature of the central region will rise until it reaches sufficient temperatures, $\sim$100 million K, to burn helium into carbon via the triple alpha process.

As the helium burning sets in, the core temperature rises in the central region, leading to a further acceleration in the nuclear reaction rates. However, since the degeneracy pressure dominates thermal pressure, the degenerate core cannot expand to release the pressure. The degeneracy of the gas is removed once the temperature reaches the point where thermal pressure dominates, occurring in a matter of a few seconds, allowing the core to violently expand in an explosion of helium ignition, termed the *helium flash*, point 5 in Figure 1.2. The majority of the energy generated in the helium flash is absorbed by the outer layers, leaving the star mostly intact. However, some loss of the envelope may occur (Karttunen et al. 2007). The luminosity will drop significantly due

to the expansion of the core and the contraction of the envelope, leaving a sharp peak in the HR diagram. The star is then able to settle into a new state, where it will burn helium into carbon and oxygen in the core.

The lower mass stars, i.e $< 1.9M_{\odot}$ (Girardi et al. 1998), will all experience helium ignition at similar luminosities due to a nearly constant core mass (Girardi 1999). Stars experiencing the helium flash will result in a large population of stars in a region of the HR diagram, termed the *red clump* found at approximately point 6 in Figure 1.2.

The higher mass stars, i.e. $> 2.3M_{\odot}$, will not have a degenerate core, allowing for helium burning without the need for a violent ignition in the core. These stars are slightly hotter than the lower mass stars because of their different envelope mass, and will burn helium at lower luminosities than the *red clump* stars. This will result in a secondary population of stars at lower luminosities, termed the *secondary clump*, labeled as SC on the evolution track of the $2.4M_{\odot}$ model in Figure 1.2 (Girardi 1999).

The core helium burning phase will occur at similar luminosities as a result of the similar core mass between the low mass and higher mass stars.

Similar to the main sequence, the central helium supply will become exhausted to form a carbon and oxygen core which contracts. Helium will begin to burn in an inner shell around the core, while still burning hydrogen in an outer shell. The star will ascend the *asymptotic giant branch* (AGB), towards point 7 in Figure 1.2, where temperature decreases and luminosity increases.

It should be noted that I have not provided a complete account of the evolutionary processes that take place within a star. I have not considered processes such as diffusion, rotation, magnetism or the amount of mixing, which are beyond the scope of this thesis.

Chapter 2

Stellar Oscillations and Asteroseismology

2.1 Asteroseismology

As a young philosopher, Pythagoras often wondered about the world around him. He came to believe that there was a natural harmony in everything that surrounded him. So much so, that he began to regard the movements of the celestial bodies as a musical harmony. Legend has it that Pythagoras himself could hear this *music of the spheres* and that the common man was not able to hear it because his soul was engrossed in material possessions. Pythagoras wrote about the common man:

> *When he liberates himself from the bondage of the lower world with its sense limitations, the music of the spheres will again be audible as it was in the Golden Age*
> Pythagoras (c 427 -347 BC)

Until recently, the concept of the music of the spheres never really took off as a scientific idea worthy of exploration. Astronomers have recently discovered that the stars "ring" like a bell playing a harmony of music, Pythagoras' " music of the spheres". Perhaps the golden age approaches once again with the advent of asteroseismology.

This "ringing" is caused by a star undergoing oscillations. These oscillations are manifested through the rarefaction and compression of the gas that propagates through the star caused by standing sound (pressure) waves. If we make the assumption that the star is an ideal gas, then the relationship of the speed of sound that depends on temperature and the chemical composition of the gas then becomes,

$$c = \sqrt{\frac{\Gamma_1 k_b T}{\mu m}} \tag{2.1}$$

where Γ_1 is the adiabatic pressure gradient ($\Gamma_1 = (\partial ln P / \partial ln \rho)_{ad}$, where P is the pressure and ρ is the density), k_b is the Stefan-Boltzmann constant, T is the temperature, μ is the average molecular weight and m is the atomic mass. This indicates that a higher temperature, hence faster molecules producing more collisions, produces a higher sound speed. Also, with a constant temperature and thermal equilibrium of the gas, the lighter gases will move faster, colliding more often than for heavier gasses; hence the sound speed will be larger for the lighter gases.

The oscillations can be measured from photometric observations. As the star oscillates, it will expand and contract. This expansion and contraction results in temperature variations. The radius can be regarded as constant for solar like oscillations, thus the $\mathrm{L} \propto \mathrm{T}^4$ relationship produces a brightness variation. Measured through photometry, this periodic brightening and dimming can be analysed to extract the frequencies, amplitudes and phases of the sound waves at the surface of the star. Astronomers can then use basic physics and models to infer the sound speed throughout the interior of the star. Photometric observations are then used to gather information about the pressure and density of the star. The equation of state is able to take this further to constrain the temperature and chemical composition. By making an assumption about the chemical composition, often close to solar, we are able to obtain the surface temperature of the star.

2.1.1 Asteroseismology and Clusters

In this thesis, I wil focus on two open clusters in the *Kepler* field of view, NGC 6791 and NGC 6819. NGC 6791 is centred at $\alpha = 19^h20^m53^s, \delta = +37°46'18''$ (J2000) and has a metallicity [Fe/H] $= +0.29$ (Brogaard et al. 2011) and an age of 8.6 Gyr (Basu et al. 2011). NGC 6819 is centred at $\alpha = 19^h41^m18^s, \delta = +40°11'12''$ (J2000) with a metallicity of [Fe/H] $= +0.09$ (Bragaglia et al. 2001) and an age of 2.4 Gyr (Basu et al. 2011).

An open cluster consists of a few hundred, even a few thousand, stars that are loosely bound to each other. The cluster is disrupted over time as it moves through the galaxy. The cluster members will continue to travel in the same broad direction as the gravitational influence of the cluster diminishes, and they then become stellar associations, or a moving group (Karttunen et al. 2007).

Open clusters can provide a laboratory to observationally constrain stellar evolution models. NGC 6791 is of particular interest due to its combination of old age and high metallicity. Stars in an open cluster are believed to originate from a single cloud of gas and dust, thus sharing a common age and initial chemical composition. The different stellar properties of each star in the cluster are therefore mainly a function of stellar mass (Kippenhahn & Weigert 1994). It is believed that the rotation and magnetic field also play a role, however, there is a lack of observational constraint on stellar evolution with respect to rotation and magnetic field (Suárez et al. 2013).

The stellar properties can be investigated through the use of a colour magnitude diagram (CMD), which is a type of Hertzsprung-Russel diagram in which the colour index replaces the spectral class and the apparent magnitude replaces the absolute magnitude. The CMD for NGC 6819, seen in Figure 2.1 clearly shows the main sequence and the red giant branch (RGB) phases of the cluster. Isochrones (seen in Figure 2.1) can then be used to determine the age based on a fit to the HR diagram of the cluster. This is typically accomplished by comparing the observed turnoff point of the main sequence in the CMD with stellar evolution models.

This technique can also be used to determine distances of clusters by comparing the position of the main sequence, rather than the turnoff point. CMDs of the nearest clusters are used as a benchmark because the distances of these clusters can be determined using parallax measurements. Additionally, the reddening which is a function of the line-of-sight extinction, must be accounted for when determining the cluster distance. The cluster isochrone can also be used to test the models we use to infer stellar properties, such as helium content and mixing processes. Casagrande et al. (2007) used appropriate stellar isochrones to determine the helium content of nearby K dwarf stars to realise that the helium content needs to be anomalously low in order to fit the luminosities and temperatures, despite finding good agreement with empirical mass-luminosity relations. If a significant number of non member stars were included in any of these types of analyses, they

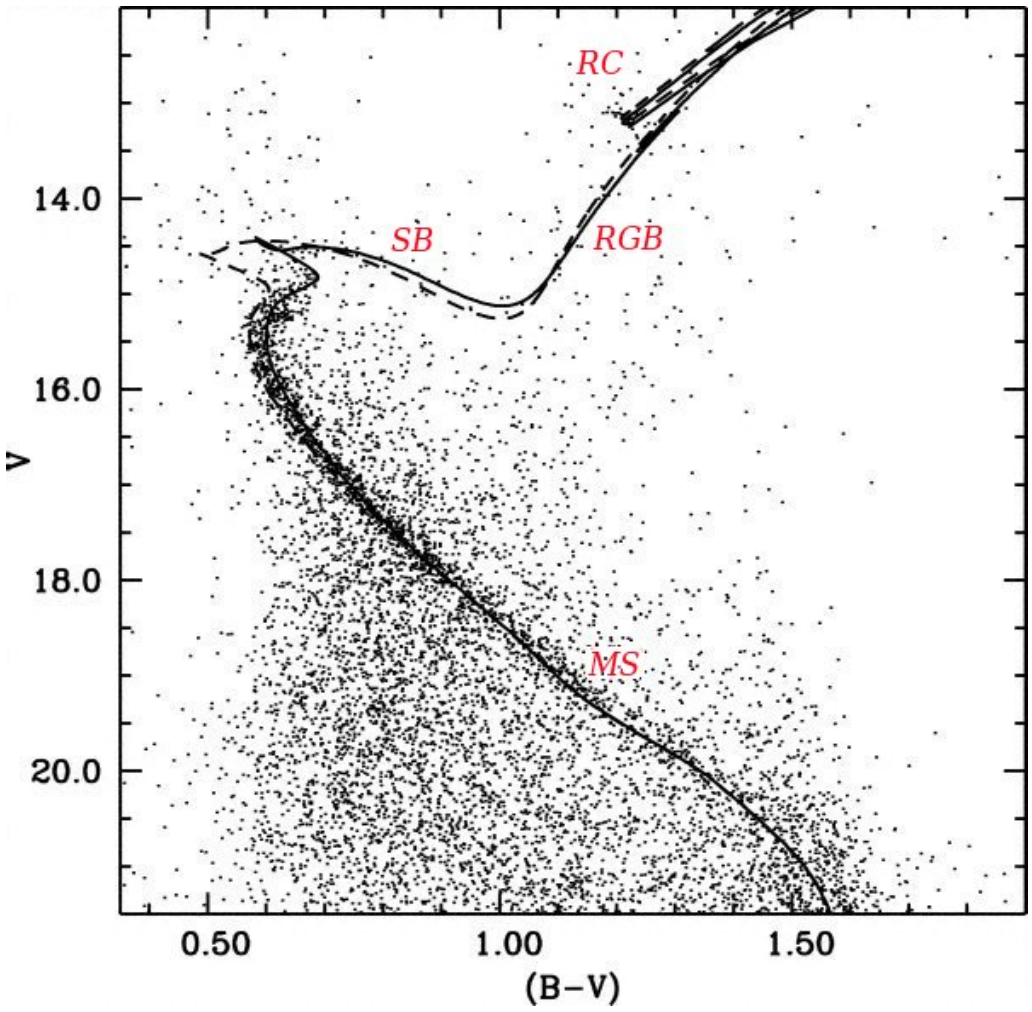

Figure 2.1: The colour magnitude diagram of NGC 6819. The Main sequence phase (MS), sub giant branch (SG) and red giant branch (RGB) can be seen. The red clump stars (RC) are visible at $V \approx 13$, $B - V \approx 1.2$. A 3 Gyr (solid line) and 1.8 Gyr (dashed line) isochrones are shown. The points that do not lie near the isochrone are field stars. Figure credit: (Pietrinferni et al. 2004)

could potentially change the morphology of the isochrone being used to infer cluster or stellar properties. Thus it is of great importance that only a clean sample of cluster members be used in an investigation such as this.

Intense study into both NGC 6791 and NGC 6819 clusters have been conducted in the past, from photometric surveys (Stetson, Bruntt & Grundahl 2003; Platais et al. 2011; Yang et al. 2013), spectroscopic surveys (Carraro et al. 2006; Boesgaard, Jensen & Deliyannis 2009; Hole et al. 2009; Frinchaboy et al. 2013), eclipsing binary studies (Brogaard et al. 2012), variable star surveys (Hartman et al. 2005; de Marchi et al. 2007; Street et al. 2005), and X-ray binary surveys (van den Berg et al. 2013; Gosnell et al. 2012), as well as recent asteroseismic measurements of red giants (Stello et al. 2010b, 2011b; Corsaro et al. 2012). All of these studies aim to provide a definitive determination of membership to the cluster studied. With the diversity of stars provided by these two clusters, ie. from main sequence to the red giant phase, it is imperative that the cluster membership of each target be ascertained prior to extensive future study.

2.2 Theory of Stellar Oscillations

2.2.1 Radial and nonradial modes

A 3-dimensional star requires 3 quantum numbers (n, l, m) to describe the modes of oscillation. l is the *degree* of the mode or the number of nodal lines on the surface of the star; *n* is the number of nodes in the radial direction, ie. number of nodal shells, known as the *radial order*; and *m* is the *azimuthal order*, number of surface nodal lines that cross the equator.

The simplest mode of oscillation is the *radial* fundamental mode, where $l = 0$ and $n = 1$. In this mode, the star will oscillate in a spherically symmetric manner with the star contracting and expanding about the core. Here the core will be the node and the surface the antinode. The first radial overtone mode has a concentric shell within the star which will be a node. The matter above and below this shell will move in antiphase to each other. Higher overtones will have an increasing number of radial shells.

The simplest of the nonradial modes are the dipole modes, where $l = 1$. Here the equator is a node, where the northern hemisphere will expand and the southern hemisphere will contract and vice versa. As the *degree, l*, of the mode increases ($l = 2$ *quadrupole*, $l = 3$ *octupole*), the complexity increases with nodes lying at different latitudes, as shown in Figure 2.2. The figure shows increasing complexity of the oscillation modes from top to bottom, with each column representing a different inclination angle to the observer.

It has been difficult to resolve the stellar surface to detect the nonradial nodes directly from intensity or Doppler maps. Intensity or Doppler maps are spatial representations of the stars surface indicating the relative motion to the core, where parts of the star will be observed to be approaching or receding from the observer, seen in Figure 2.2. As a consequence, for stars other than the Sun, it is necessary to use an integrated surface quantity, such as brightness or radial velocity. As a function of the increasing degree, *l*, of modes, the stellar surface will be divided into an increasing number of zones, with the neighbouring zones having the opposite phase of intensity as seen in Figure 2.2. Hence, the observed amplitude for higher degree modes will be smaller than the modes of lower degree because the integrated brightness will have partially canceled out, *geometric cancellation* (Dziembowski 1977). The partial cancellation of intensity restricts observations to detect the low *l* modes ($l < \sim 4$) of oscillation (Christensen-Dalsgaard, Bedding & Kjeldsen 1995; Kjeldsen et al. 2003; Bedding et al. 2007; Carrier et al. 2007).

2.2.2 p and g modes

There are two main classes of standing waves in stars: pressure modes, or *p modes* where the restoring force is the pressure gradient; and gravity modes, or *g modes*, where the restoring force is buoyancy. The p modes will primarily have vertical motions, while the g modes will have primarily horizontal motion. Both the p and g modes can be modeled in terms of ray paths (Gough 1993). The ray paths for p modes, seen in Figure 2.3a, travel between the surface and an inner turning point. The confinement of the rays indicates that the p modes are sensitive to conditions near the surface. These rays are bent by the increase in wave speed as the penetration depth increases. Figure 2.3b, shows that the ray paths of g modes are confined to the central regions, thus indicating that the g modes do not penetrate to the surface, therefore the g modes are sensitive to conditions within the core (Cunha & Metcalfe 2007).

Figure 2.3b, indicates that for solar-like stars, the g modes are trapped beneath the convective layers. This suggests that they will not be observable. However, after the star leaves the main

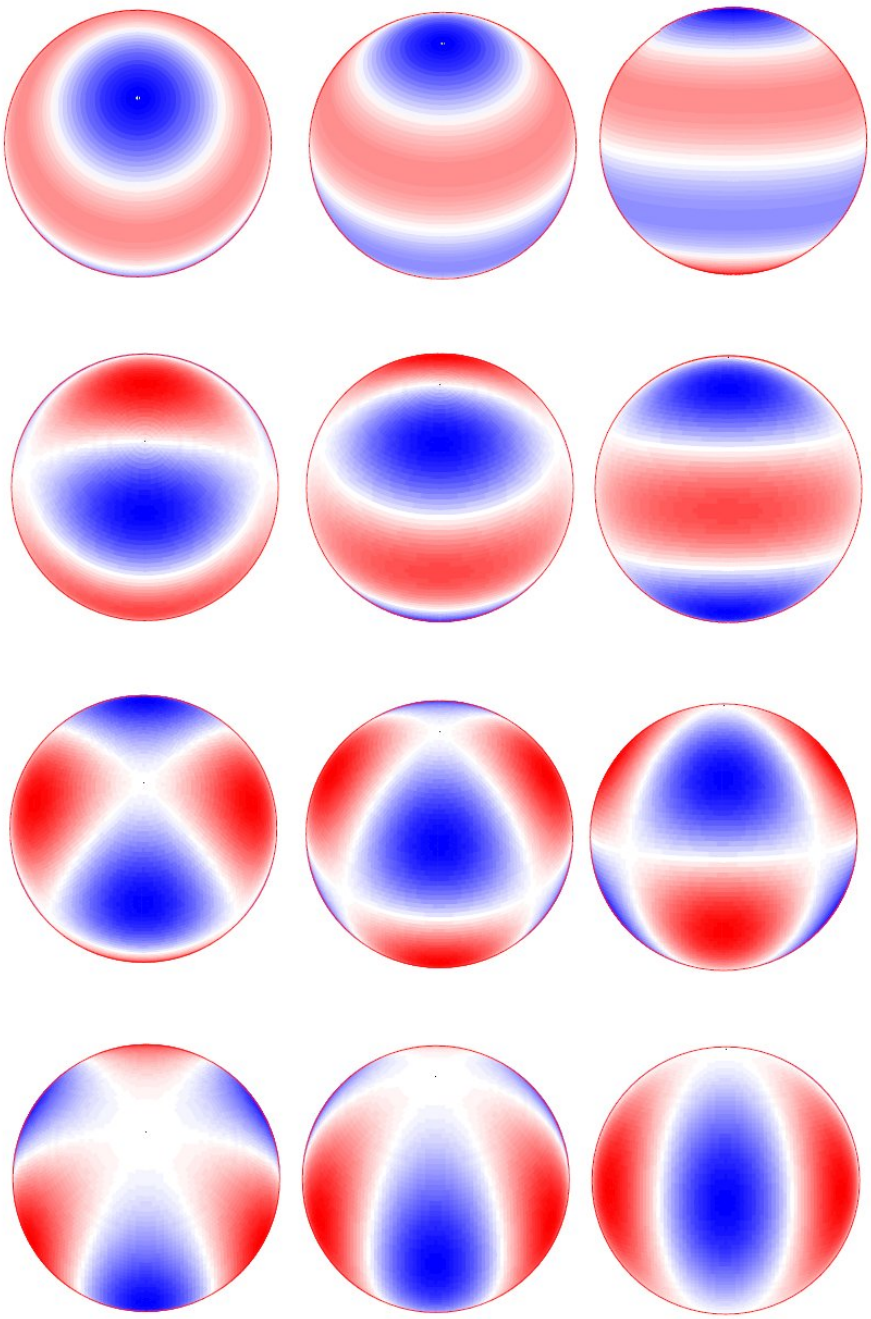

Figure 2.2: Snapshot of non-radial oscillations at different inclination angles: The columns increase in inclination angle from left to right, 30°, 60°, 90°inclination of the pole of oscillation. The white bands indicate the location of the surface nodes, the red and blue represent sections that are moving in antiphase to each other. The top row shows the octupole mode ($l = 3, m = 0$). The second row shows the *tesseral* mode, where ($0 < |m| < l$), here $l = 3, m = \pm 1$, with nodes at two latitudinal lines and one longitudinal line. The third row is an additional tesseral mode, with $l = 3, m = \pm 2$, with nodes at two longitudinal lines and one latitudinal line. The fourth row shows the *sectoral* mode, where $l = |m|$, here $l = m = 3$. The increasing complexity from top to bottom shows the neighbouring zones getting smaller, and hence contributing less and less to the overall integrated light, giving rise to geometric cancellation. Figure credit: (Aerts, Christensen-Dalsgaard & Kurtz 2010)

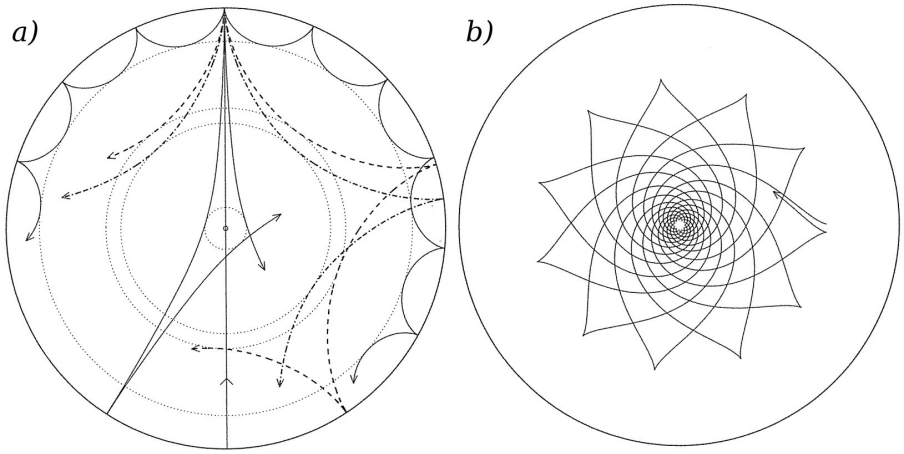

Figure 2.3: Propagation of the ray paths for sound or gravity waves in a solar like star. The acoustic rays (a) are bent by the increase in sound speed with depth until the total internal reflection occurs at the inner turning point. The acoustic waves are reflected at the surface by the rapid decrease in density. The p mode ray's path corresponding to a frequency of 3000 μHz shown corresponds to increasing penetration depth for degrees $l = 75, 25, 20, 2$. The gravity mode ray path (b) corresponds to a mode frequency of 190 μHz and a degree $l = 5$ and is trapped in the interior region. Figure credit: (Aerts, Christensen-Dalsgaard & Kurtz 2010)

sequence phase, the p modes are able to couple with the g modes, forming so called "mixed" modes. These mixed modes allow a component of the g-mode waves to be observable at the surface. I will not discuss the g modes any further as it is only the p modes that pertain to work done in this thesis.

Another important property of p modes is that when $n \gg l$, an asymptotic relation indicates that there is an equal spacing in frequency. Tassoul (1980, 1990) has shown that in the asymptotic relations, the p modes frequencies are approximated by

$$\nu_{nl} \simeq \Delta\nu \left(n + \frac{l}{2} + \alpha \right) + \epsilon_{nl} \tag{2.2}$$

where *n* and *l* are the radial order and the angular degree of the mode, α is a constant, ϵ_{nl} is a small offset and $\Delta\nu$ is the so called *large frequency separation*. In the asymptotic relation, the large separation equals the sound crossing time of the star, given by

$$\Delta\nu = \left(2 \int_0^R \frac{dr}{c(r)} \right)^{-1} \tag{2.3}$$

where c(r) is the sound speed at radius r and R is the stellar radius. Since the large frequency separation is sensitive to the radius of the star, it can be used as a measure of the mass of a star near the main sequence phase.

The increase in the mean molecular weight, μ, during hydrogen burning causes a decrease of the sound speed towards the centre of the star. Kjeldsen, Bedding & Christensen-Dalsgaard (2008), were able to show that with an accuracy of 0.1μHz in the observed frequencies, the age of a solar-like oscillator can be determined to better than 10% of its main sequence lifetime. This was later confirmed with a number of age determinations using CoRoT and Kepler data (Lebreton & Goupil 2014; Lebreton & Montalbán 2009; Sandquist 2013; Soderblom 2010).

2.2.3 Oscillation Mechanisms

All stars are expected to pulsate due to a variety of mechanisms. Initially Eddington (1918) proposed that pulsating stars are thermal heat engines. As layers of the star expand and contract through the pulsating cycle, the gas within the layers do work. If the net work done for the cycle is positive, the layer contributes to the driving of the oscillations. If the net work done by the layer is negative, the oscillations will be damped. However, I am chiefly concerned in this thesis with stars that have oscillations that are excited in the same way as the Sun, *solar-like oscillations*, i.e. convection. The heat engine mechanism will produce oscillations in red giant stars (Aerts et al. 2008), however, it will not produce enough energy to contribute to driving the oscillations at the surface. The oscillations in red giants will be driven predominantly by convection.

Convection

As discussed in Section 1.2, the cooler less massive stars will have a convective envelope, which is the source of the p mode oscillations. The convective envelope contains convective cells that will rise from high density regions, to regions of low density, before they release the energy stored within. The total energy inside the cell then drops and the cell sinks back to a region of high density where it *acquires* more energy, heats up, and repeats the process. Across the stellar surface, there will be many hundreds of thousands to many millions of these convective cells that transport energy to the surface in seemingly random intervals, creating the turbulent motion. The acoustic waves, generated by the turbulent gas motion that have the same frequency as the natural resonant modes of the star, will then be stochastically driven to observable amplitudes. These stochastically driven oscillations are commonly referred to as solar-like oscillations because they occur in stars that have a convective outer layer like the Sun, (Buzasi et al. 2000; Frandsen et al. 2002), including late type G, K and M red giants, (Frandsen et al. 2002; De Ridder et al. 2006, 2009; Stello et al. 2014).

2.3 Observations of Solar-like Oscillations

There are a number of methods by which solar-like oscillations can be observed, all of which rely on the changes in the photosphere. As explained earlier, oscillations in a star cause the surface to move toward and away from us at different latitudes and longitudes, varying in $T_{\rm eff}$ as the star oscillates. The line-of-site component of this motion causes a Doppler shift of the light being emitted, which can be measured by observing the spectral lines in the spectrum. This is known as the radial velocity method. The Balmer lines of the spectrum can also be used to measure these oscillations by measuring the variations in the equivalent widths of these lines, which are sensitive to temperature (Kjeldsen et al. 1995; Bedding et al. 1996). However, Bedding (2011) noted that the equivalent width method for observing oscillations turned out to be more sensitive to instrumental drifts than originally thought. Finally the oscillations cause the luminosity of the star to vary with time allowing photometric detectors, typically CCDs, to observe these fluctuations.

Using radial velocity measurements Brown et al. (1991) showed that the variations seen in the subgiant Procyon are stellar in origin, consistent with solar-like p-modes. They were not able to conclusively determine the oscillation frequency, assuming p-mode oscillations. However, with more data (Mosser et al. 1998; Martić et al. 1999; Barban et al. 1999), it was confirmed that Brown et al. (1991) had indeed made the first clear detection of solar-like oscillations (Bedding & Kjeldsen 2010).

Until recently, observations of solar-like oscillations were restricted to ground based telescopes. This mostly limited the early detections to the radial velocity method, since photometry is heavily affected by atmospheric scintillation. Gilliland et al. (1993) was able to improve the detection sensitivity of solar-like oscillations with a multisite campaign using photometry from seven groups observing stars in M67. They were however, unable to make a clear detection of solar-like oscillations in the stars observed. Following Gilliland et al. (1993), Stello et al. (2007) targeted red giant stars in M67 during a multisite campaign to measure solar-like oscillations. They were able to test the scaling relations (see Section 5.3) for the first time, but were also unable to make any clear detections of oscillations.

Not long after, major breakthroughs in radial velocity technologies were made, driven by a concerted effort to find extra-solar planets. Clear detections of oscillations of the subgiant β Hyi (Bedding et al. 2001) and α Cen A (Bouchy & Carrier 2001; Carrier et al. 2002) are thus seen as the birth of asteroseismology. A series of successful observations were made providing the first application of asteroseismology to a planet hosting star, μ Ara (Bouchy et al. 2005), and clear detections in the solar twin 18 Sco (Bazot et al. 2011). The prediction of solar-like oscillation in red giant stars was also confirmed when oscillations were detected in ξ Hya (Frandsen et al. 2002) and ε Oph (De Ridder et al. 2006).

The ground based observations have been fraught with the difficulties of dealing with gaps in the data from the day-night cycle. These gaps create aliasing in the frequency domain, complicating the interpretation of the oscillation signal. Attempts have been made to deal with these gaps by organising mutli-site campaigns to produce uninterrupted data. Multi-site campaigns however, are notoriously difficult to organise; to date the cluster M67 (Gilliland et al. 1993; Stello et al. 2007), the subgiant β Hydri (Bedding et al. 2007), the subgiant Procyon (Hekker et al. 2008; Arentoft et al. 2008; Bedding et al. 2010b), the red giants γ Psc and θ^1 Tau (Beck et al. 2014) have been observed using multi-site campaigns. Arentoft et al. (2008) conducted a multisite campaign to measure radial velocities for Procyon A and found clear detection of solar-like oscillations. Bedding & Kjeldsen (2010) followed by extracting 55 mode frequencies over 20 radial orders from the same data. To facilitate multi-site campaigns for asteroseismology, a dedicated network of eight 1-m telescopes, the Stellar Observations Network Group (SONG), has been planned, with the first and second nodes in Tenerife and China commencing operations (Grundahl et al. 2009; Wang et al. 2014).

The preferred solution to the aliasing problem is to observe continuously from space, minimising the gaps in the data and avoiding the limitation of atmospheric scintillation. The failure of the primary mission of NASA's *Wide-Field Infrared Explorer* satellite (*WIRE*) allowed the star camera to be re-tasked for asteroseismology (Schou & Buzasi 2001; Fletcher et al. 2006; Retter et al. 2003; Stello et al. 2008). The Solar Mass Ejection Imager (SMEI) was used to observe oscillations in bright red giants (Tarrant et al. 2007, 2008). The *Hubble Space Telescope* was utilized both via direct imaging (Edmonds & Gilliland 1996; Stello & Gilliland 2009) and using its fine guidance sensors (Kallinger et al. 2005; Gilliland et al. 2011) to observe solar-like oscillations in red giant stars.

Great success was achieved from the first dedicated asteroseismology space mission *Microvariability and Oscillations of STars* (*MOST*) using observations of classical pulsators (Walker et al. 2003; Matthews 2007), red giants (Kallinger et al. 2008) and Procyon (Huber et al. 2011a). The French-led Convection Rotation and planetary Transit (*CoRoT*) mission, launched in December 2006, led to a revolution in asteroseismology by detecting oscillations in thousands of red giant stars (De Ridder et al. 2009; Hekker et al. 2009; Carrier et al. 2010; Mosser et al. 2010) as well as in main sequence and subgiants (Michel et al. 2008; Appourchaux et al. 2008). The asteroseismic

revolution continued to make great strides with the launch of *Kepler* in March of 2009. Although its primary goal was to search for extra-solar planets, *Kepler* has also detected solar-like oscillations in thousands of stars, from main sequence to M giants (Miglio et al. 2009; Bedding et al. 2010a; Huber et al. 2010; Kallinger et al. 2010; Mosser 2013) and continues to provide valuable data for stellar evolution (Jeffery & Ramsay 2014; Gizis 2014).

2.4 Properties of Solar-like Oscillations

In order to extract information about the stars we observe, we need to compare observations to the theory. Some theory has already been introduced, such as the large frequency separation, in Section 2.2.2. This theory indicates that we should expect to find peaks with regular spacing in the Fourier spectrum of a time series containing the oscillation signal. In addition, we should also find that odd modes will be approximately half way between even modes, with modes with the value of $n + l/2$ being almost degenerate. Ulrich (1986) showed that the large frequency separation, Equation 2.3, is approximately proportional to the square root of the mean stellar density

$$\Delta\nu \propto \sqrt{\frac{M}{R^3}} \tag{2.4}$$

Looking at the power spectrum of the Sun more closely, Figure 2.4b, we see that there is a difference in the modes with the same $n + l/2$ value. These differences arise from the *small frequency separation*, the frequency spacing between odd/even angular degree of the same radial order.

Additional properties can be observed by plotting the frequencies of each mode modulo the large frequency separation, termed an échelle diagram, (Grec, Fossat & Pomerantz 1983). Modes of the same degree, l, will form nearly vertical ridges as seen in Figure 2.5. Sloping ridges will indicate an incorrect value of $\Delta\nu$ chosen, thus providing a diagnostic of the $\Delta\nu$ value. Any variation in the vertical ridges are clearly observed and representative of physical changes within the star.

The amplitudes of oscillation can also tell us meaningful information about the star. Figure 2.4a shows that the amplitudes of the modes follow a broad gaussian envelope. The shape and position of this envelope is dictated by the oscillation mechanism and are therefore dependent on fundamental stellar properties. The central frequency of this gaussian envelope is denoted by ν_{max}, the frequency at maximum power. This frequency is believed to scale with the frequency above which the acoustic modes are not reflected at the surface. By approximating the surface temperature to be the effective temperature, $T_{\rm eff}$, of the star, we find

$$\begin{aligned} \nu_{\rm max} &\propto \frac{g}{\sqrt{T_{\rm eff}}} \\ &\propto \frac{M}{R^2\sqrt{T_{\rm eff}}} \end{aligned} \tag{2.5}$$

where g is the surface gravity (Brown et al. 1991). It has been seen that Equations 2.4 and 2.5, will follow a power law relation for $\nu_{\rm max}$ and $\Delta\nu$ (Hekker et al. 2009; Stello et al. 2009; Mosser et al. 2010; Hekker et al. 2011c).

$$\Delta\nu \simeq \alpha \left(\nu_{\rm max}\right)^{\beta} \tag{2.6}$$

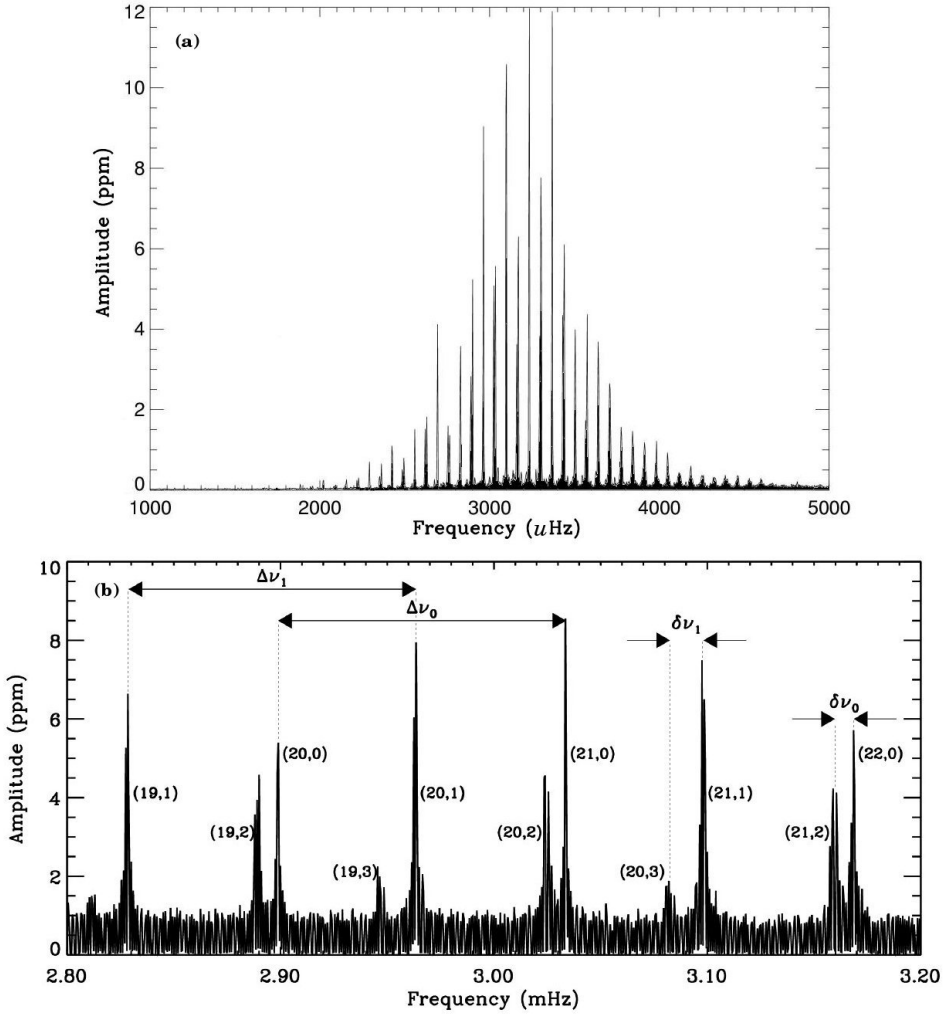

Figure 2.4: (a) The solar power spectrum from 36 days of radial velocity measurements obtained with the GONG network. (b) A close up view of panel (a) centred on the frequency of maximum power, indicating the radial order, n, and the spherical degree, l of each mode. The dotted lines indicate the large and small separations, $\Delta\nu$ and $\delta\nu$ respectively. The odd modes can be seen to be half way between the even modes. (ie. $\delta\nu_{n,1}$ halfway between $\delta\nu_{n,0}$ and $\delta\nu_{n,3}$)

where α and β are scaling relation coefficients and $\nu_{\rm max}$ is in μHz. Huber et al. (2011b), Silva Aguirre et al. (2012), Miglio, Montalbán & Noels (2012) and Silva Aguirre et al. (2013) have all applied different methods to verify and constrain this relationship. Huber et al. (2010) showed that main sequence stars and red giants have different power law coefficients, such that a $\nu_{\rm max}$ value close to solar would be underestimated by 10% when the scaling relation was calibrated to red giant stars. In agreement with the expectations of scaling relations, Huber et al. (2011b) showed that these differences in $\Delta\nu$ –$\nu_{\rm max}$ relation between unevolved and evolved stars can be attributed to different distributions in effective temperature and stellar mass. Silva Aguirre et al. (2013) were able to verify the radii, $T_{\rm eff}$ and bolometric fluxes to an excellent level of accuracy for main sequence to red giant stars. Therefore, when the effective temperature is known, this scaling

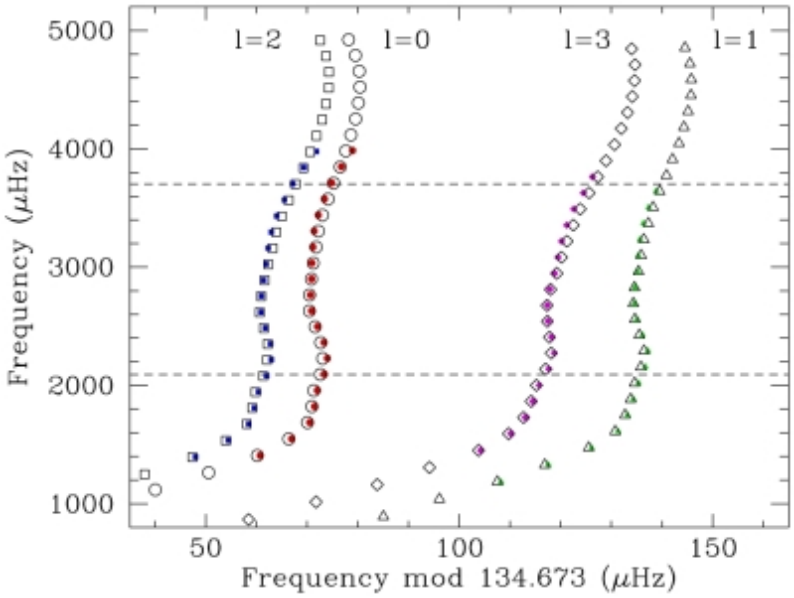

Figure 2.5: Échelle diagram of the observed frequencies in the Sun. The coloured symbols show the observations while the open symbols show the best stellar model from Metcalfe (2009). The oscillation modes $l = 0$ to 2 in a range of frequencies between the dashed lines were used for the model fit. However, there is good agreement outside of this range and for the modes for degree $l = 3$.
Figure credit: (Metcalfe 2009)

relation allows us to estimate the mass and radius of a star when $\Delta\nu$ and $\nu_{\rm max}$ are measured (Stello et al. 2008). This method is known as the'direct method' and can be seen more clearly by manipulating Equations 2.4, 2.5 and Equation 2.6 to obtain

$$\frac{M}{M_\odot} \approx \left(\frac{\nu_{\rm max}}{\nu_{\rm max,\odot}}\right)^3 \left(\frac{\Delta\nu}{\Delta\nu_\odot}\right)^{-4} \left(\frac{T_{\rm eff}}{T_{\rm eff\,\odot}}\right)^{3/2} \tag{2.7}$$

$$\frac{R}{R_\odot} \approx \left(\frac{\nu_{\rm max}}{\nu_{\rm max,\odot}}\right) \left(\frac{\Delta\nu}{\Delta\nu_{,\odot}}\right)^{-2} \left(\frac{T_{\rm eff}}{T_{\rm eff\,,\odot}}\right)^{1/2} \tag{2.8}$$

Previously, mass and radius were determined through comparison of observed frequencies and frequencies calculated from models. The 'direct method' of observing is becoming more common (see Chaplin et al. (2011); Huber (2014); Epstein et al. (2014) because it is only required to measure $\Delta\nu$ and ν_{max}.

Chapter 3

The *Kepler* Mission

The universe is a pretty big place. If it's just us, seems like an awful waste of space. - Carl Sagan

3.1 Background

As Carl Sagan indicates, the sheer size of the universe seems to suggest that it is difficult to believe that mankind is the only advanced life-form in the universe. People have speculated the existence of extra terrestrial life for thousands of years, from apparent UFO sightings since 214 BCE (Foster 1854) to authors producing tales of travel to other inhabited worlds in the 17th and 18th centuries and beyond. Serious theories have been proposed explaining the existence of extrasolar planets dating back to Aristotle and Epicurus, 2400 years ago (Dick 1996). The search for extrasolar planets and extraterrestrial life is one of the 'holy grails' of astronomy, particularly the search for Earth's twin.

Since the light from a planet is minuscule compared to the light emitted from a star, it is a difficult enterprise to directly detect a planet in another solar system. This did not stop scientists from coming up with techniques that would allow us to infer the presence of a planet. By observing the star over time, the absorption lines in the spectrum would shift back and forth periodically, suggesting that the star is 'wobbling' back and forth. This Doppler effect is explained by the gravitational pull of an unseen planet in a close orbit. This effect was exploited by Mayor & Queloz (1995) to find the first clear detection of a Jupiter mass planet in close orbit around a Sun-like star, 51 Pegasi. Since then, many more planets have been detected (at the time of writing, 532 planets have been detected via radial velocity). The inherent bias in the radial velocity method causes the majority of the detected planets to be more massive than Jupiter and in close proximity to the host star because they will create the largest radial velocity variation. It is much more difficult to find a planet that could conceivably harbour life as we know it, a twin of Earth, i.e. an Earth-sized planet in an Earth-like orbit around a Sun-like star. Until recently, the radial velocity method has been the most successful method for detecting extrasolar planets.

Advances in detector technology have allowed the transit method to be used to detect smaller planets at greater distances from the host star, complementing the radial velocity method. The transit method utilises the fact that the planet will block a portion of the light from the star as it travels between us and the stellar disk. In order to obtain a clear detection of exoplanets using the transit method, three criteria are required: 1. The observations must be continuous to avoid missing transit events; 2. The detector system is required to be sensitive to minuscule variations

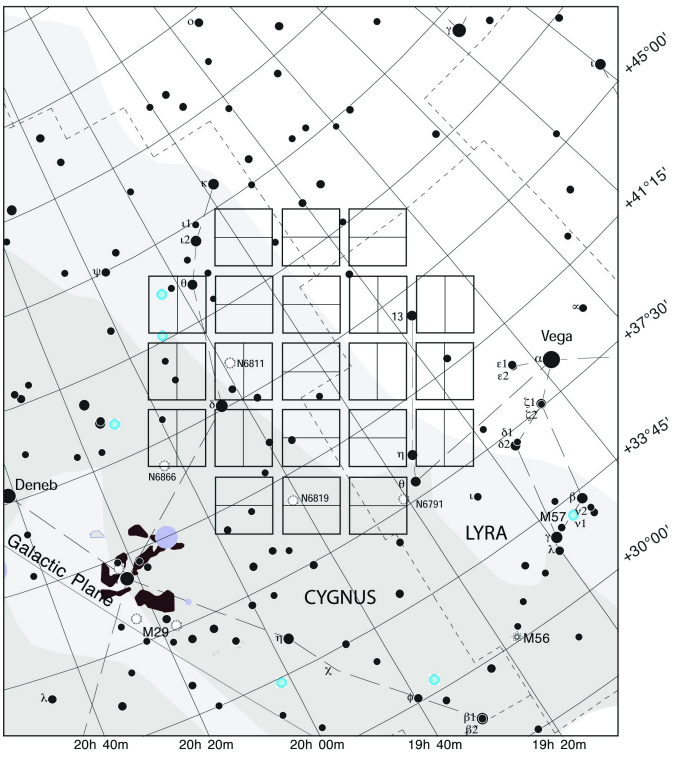

Figure 3.1: Kepler field of view projected on a star map showing the higher magnitude stars in the FOV. The individual rectangles mark the array of 42 CCD detectors (see Figure 3.2). The CCD's were aligned so that the brighter stars ($m_v > 6$) in the FOV fall in the gaps to avoid saturation.
Figure credit: NASA

in measured light; and 3. A large sample size is required to increase the chances of observing a planet orbiting in the plane of the line of sight to the observer.

The most recent exoplanet detectors have been launched into space to avoid the limitations of ground based networks, gaps in the data from poor weather and daylight, and atmospheric scintillation limiting sensitivity. The first space telescope to be dedicated to the search for exoplanets was the French led CoRoT mission (Barge et al. 2008). NASA soon joined the exoplanet 'party' by launching *Kepler* in March 2009. *Kepler* had a nominal mission of three and a half years to stare continuously at a single patch of sky, Figure 3.1, to search for Earth-sized planets in or near the habitable zone of Sun-like stars (Borucki et al. 2010). The habitable zone is the region around the star in which the temperature of the planet allows for liquid water to exist on its surface, a necessary condition of life.

3.2 Mission Details

The mission focus dictated the nominal length of the mission to three and a half years. To confirm the orbit of a transiting exoplanet, there must be a minimum of three transits observed, thus for a planet in an Earth-like orbit, this requires three years of observations.

Kepler is a single purpose photometer based off a schmidt telescope, with a 0.95m aperture, a 105 deg^2 field of view and a $1.4m$ primary mirror. A cross section is shown in Figure 3.2. The

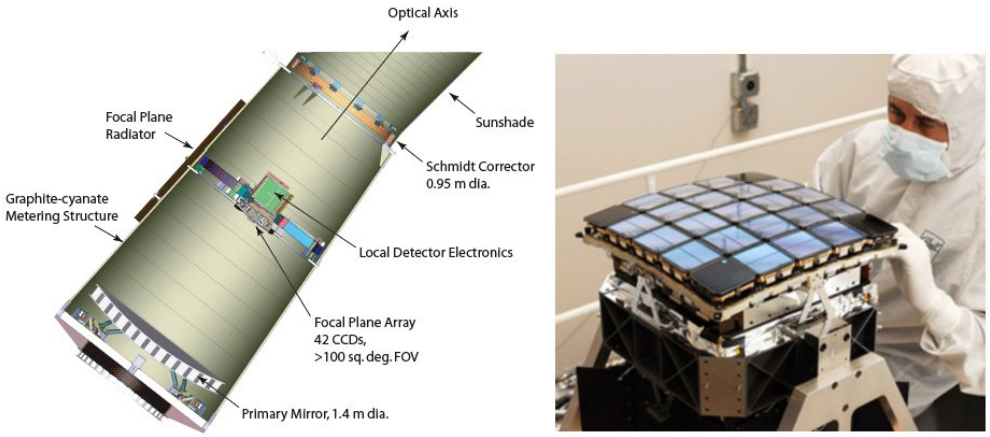

Figure 3.2: Left: A cross-section of the *Kepler* telescope showing the primary and correcting mirror, as well as the CCD array on the focal plane. *Right*: The 42 CCD array under construction at Ball Aerospace laboratories. Figure credit: NASA

detector, consisting of an array of 42 CCDs, is set at the primary focus. To minimise detector noise, the CCD is cooled using liquid nitrogen and an external radiator, which can be seen in Figure 3.3.

There are two modes of integration, short cadence (SC) and long cadence(LC). Short cadence data is integrated over 58.85 sec allowing a more accurate measurement of the transit times, possibly revealing additional planets through transit timing variations. Observations with short cadence data will reveal stellar variations of periods in the order of a few minutes, such as solar-like oscillations in main sequence stars (1-5 minutes).

The short cadence mode only allows for a small number of targets to be simultaneously observed, ~ 500. The majority of the stars are observed in long cadence mode, with one data point every 29.4 minutes, sufficient for detecting transits typically lasting several hours. The long cadence observations also permit the detection of oscillations with periods larger than a few hours which is typical for red giants (Huber et al. 2010; Kallinger et al. 2010; Jendreieck et al. 2012; Miglio, Montalbán & Noels 2012). Considering these cadences, the bandwidth prohibits *Kepler* from returning complete images of the field of view, or observing all stars in the field. The target stars are observed using 'pixel masks' that contain all the flux from each target star.

The *Kepler* spacecraft was launched into an Earth trailing heliocentric orbit, Figure 3.4, on March 7 2009, allowing the spacecraft to avoid stray light from Earth or the Moon. The spacecraft slowly drifted away from the Earth and reached a maximum distance of 0.5 AU after 4 years. Additionally, this orbit is highly stable, having a very low disturbing torque on the spacecraft. Power to the *Kepler* spacecraft is provided by the solar panels seen in Figure 3.3 surrounding half the spacecraft. The spacecraft maintains constant power by reorienting itself every three months to keep the solar panels directed toward the Sun. Thus *Kepler* data is naturally split up into ~ 90 day blocks called quarters. *Kepler* observations began on 2 May, 2009 for a 10 day commissioning period, called Quarter 0 (Q0), which was then followed by a short one month long quarter, Q1, before the first spacecraft roll. Each quarter since, lasted three months until Q17 when the nominal mission ended. Rotational torques from solar pressure acting on the spacecraft were corrected using three of four reaction wheels (one for each degree of freedom and one spare in case of failure). These three reaction wheels maintained fine pointing of the telescope while

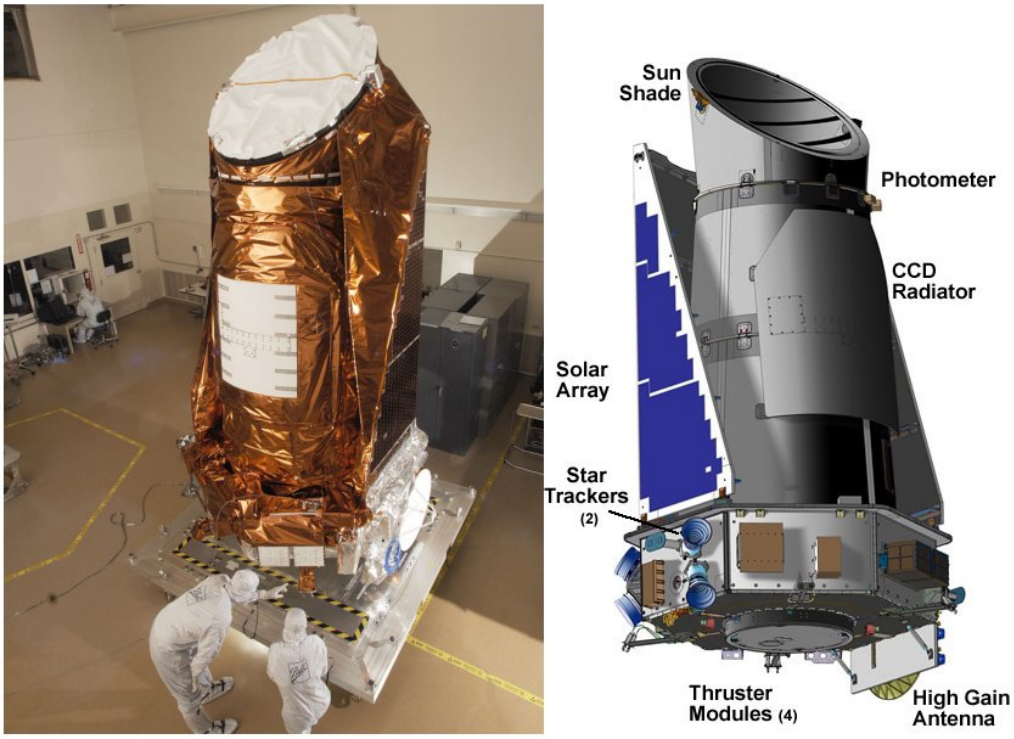

Figure 3.3: Left: Engineers from Ball Aerospace, where the *Kepler* telescope was built and assembled, checking the spacecraft before being transported to NASA. *Right*: A schematic diagram of the spacecraft identifying the solar panels, radiator that cools the CCD's and the high gain antenna for communication with the ground.
Figure credit: NASA

observing. The spacecraft is prevented from spinning by the angular momentum being transferred to the reaction wheels via the wheels spinning up over time. This angular momentum will continue to build until it reaches its operational limit, unless the spacecraft uses its thrusters to 'dump' the angular momentum every three days (García et al. 2011).

On 9 January 2010, one of the CCD modules (Module 3) failed during operations, affecting two of the 42 CCD devices (discussed in detail in Section 4.2.1). Since this time, these detectors have not been able to make observations. The stars that fall on module 3, including stars in NGC 6819, in one quarter per year were still observed during the remaining three quarters.

To achieve the scientific objective of *Kepler*, the spacecraft was pointed towards the constellation of Cygnus and Lyra, Figure 3.1, which was chosen for the richness of stars. Cygnus and Lyra provide a large selection of stars from early to late evolutionary stages.

3.2.1 *Kepler* Now and into the Future

Kepler has been able to produce outstanding successes in stellar evolution. Detailed properties of oscillation modes allow the distinction between the stars on the red giant branch and those in the red clump region (Bedding et al. 2011). *Kepler* data has also been used to perform in-depth modeling of individual stars (di Mauro et al. 2011), allowing for mode identification (Huber et al. 2010; White et al. 2012). Stellar evolution models have been contrained using mixed modes (Benomar et al. 2014), post helium flash stars (Kawaler 2012) and a number of studies into clusters

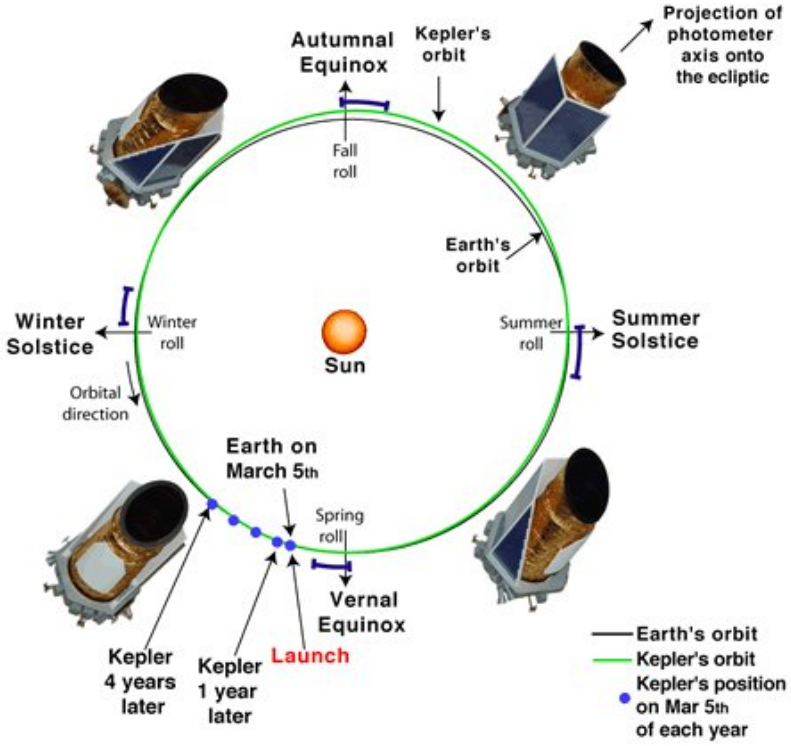

Figure 3.4: A schematic view of the heliocentric orbit of *Kepler* as viewed from the ecliptic North Pole. Each quarter the spacecraft rolls to realign the solar panels toward the Sun. The blue dots at the southern end of the image indicate the successive positions of the *Kepler* spacecraft after each year of operation.
Figure credit: NASA

(Stello et al. 2010b; Basu et al. 2011; Stello et al. 2011b,a; Corsaro et al. 2012; Miglio et al. 2012). People within the galactic archeology community have also begun to realise the potential use of these oscillations as standard clocks and rulers for galactic studies (Miglio et al. 2014). Standard clocks and rulers are used to infer details of the evolution of the universe and the conditions in the early universe. Christensen-Dalsgaard (2014) also suggests that *Kepler* will be able to provide a determination of the helium abundances in red giants (Broomhall et al. 2014), constraining the chemical evolution of the galaxy.

Despite the loss of the two modules *Kepler* experienced, there is still a large amount of data to be analysed. As such there is still a wealth of information to be gained, from exoplanets to galactic archeology (Lissauer et al. 2011; Steffen et al. 2011; Borucki et al. 2012; Barclay et al. 2013a,b).

Chapter 4

Time series Detrending

4.1 Target Selection

Cluster membership studies using asteroseismology are currently limited to stars that show stochastic oscillations driven by near-surface convection (solar-like oscillations). The seismic observables $\nu_{\rm max}$ and $\Delta\nu$ are a representation of the oscillations produced. The seismic observables of a star are strongly linked to its fundamental stellar properties, which can be described by well established scaling relations (see Section 2.4). To observe these stochastic oscillations, we require the oscillations to be sufficiently sampled. Therefore when using the spacecrafts long cadence mode, we are limited to observing red giants.

I aimed to maximise the number of cluster members in my sample (See Appendix A and B) by selecting all available red giant stars within a 20$^{\backprime}$ radius from the centre of each cluster, selected through various Guest Observer (GO) proposals and Kepler Asteroseismic Science Consortium (KASC) working group initiatives (See Appendix C). This left me with a total of 232 red giants around NGC 6791 and 206 red giants around NGC 6819. In addition to the targeted stars in the *Kepler* field, there are also large 200 x 200 pixel CCD superstamps of NGC 6791 and NGC 6819 taken at long cadence. These superstamps provide the opportunity to obtain photometric time series data of all unresolved stars in the field. Kuehn et al. (2015) have used profile fitting and image subtraction to successfully extract light curves from the partially blended stars in this region. However, these methods require further refinement and are still ongoing.

4.2 Data Characteristics

In this study I used *Kepler* LC data obtained between 1^{st} May 2009 and 11^{th} May 2013, known as observing quarters Q0 - Q17. This observing period provided approximately 59,000 data points per star. The data are available in two formats; the simple aperture photometry (SAP) flux measurements, which contains perturbations due to instrumental effects; and the corrected flux measurements where these instrumental perturbations are minimised. The corrected light curves are created by processing the SAP data through the Pre-search Data Conditioning (PDC) procedure (Jenkins et al. 2010) as part of the *Kepler* Science Pipeline at NASA Ames Research Centre.

The PDC procedure attempts to remove perturbations such as pointing drifts, focus changes and thermal effects while maintaining planet transits and other astrophysical signals of interest. These requirements mean that the PDC procedure will not be completely effective for all stars in removing the non-astrophysical signals, thus the data may require further processing. I use

the PDC corrected data due to the complex nature of the corrections required for the SAP data, minimising the work required to facilitate asteroseismic analysis.

4.2.1 PDC Data Characteristics

The data characteristics of the PDC data products are of particular interest as they influenced how the data was analysed. The different aspects of the CCD (CCD gain, aperture, crowding metric, etc (García et al. 2011)) will potentially cause different characteristics to show up in the data. I describe some of the charactersitics that I encountered in the PDC corrected data, and how I was able to mitigate against the influence of these characteristics. I do not discuss all features of the data, as many of the features had no effect on my analysis.

Jumps

The PDC light curves show jumps in the average flux level from one quarter to the next caused by the 90°quarterly rolls, resulting in a change in the aperture for the star being observed. To correct for the jumps, I developed an interactive algorithm that provided a visualisation of three alternative stitching methods, as seen in Figure 4.1, along with additional processing options to enable seamless stitching together of the quarters for each individual star. In each case, the first quarter of available data for any given star is used as a reference.

- The first stitching method, LinearAlignment, is based on linear interpolation between successive quarters. A first order polynomial is fitted to the last two days of the reference quarter and an additional first order polynomial is fitted to the first two days of the successive quarter. The two midpoints of the polynomials are then aligned by shifting the second quarter up or down as required. I note that if the gap between each quarter is large, there is no expectation that a linear alignment would produce a continuous light curve, therefore the alignment is only performed when the gap between each quarter is less than a predefined tolerance. I found a gap of less than 17 days to be acceptable. When the gap is larger than this, I did not align the data with this method and used one of the alternative procedures described below. The predefined gap and the number of days fitted for the alignment are modifiable by the user for each star. This allows the user to analyse a broad range of stars, from main sequence to red giants.

- The second method, AverageAlignment, was applied to the majority of the stars to shift the average flux level of each quarter to match that of the previous quarter.

- Finally, the third method is a combination of the previous two, CombinedAlignment. This method will use the LinearAlignment method when the gap between each quarter is less than a predefined tolerance, and the AverageAlignment method when the gap is larger.

Evaluation of the light curve, and resulting power spectrum of each stitching method, enabled the decision to perform any further processing. This would include the use of high pass filtering to smooth the light curve, the ability to remove any long term trends in the data using polynomial fitting of up to the fourth order for each individual quarter, and outlier removal. The resulting light curve and power spectrum were displayed for visual inspection before the final alignment and processing options were chosen (see Figure 4.1).

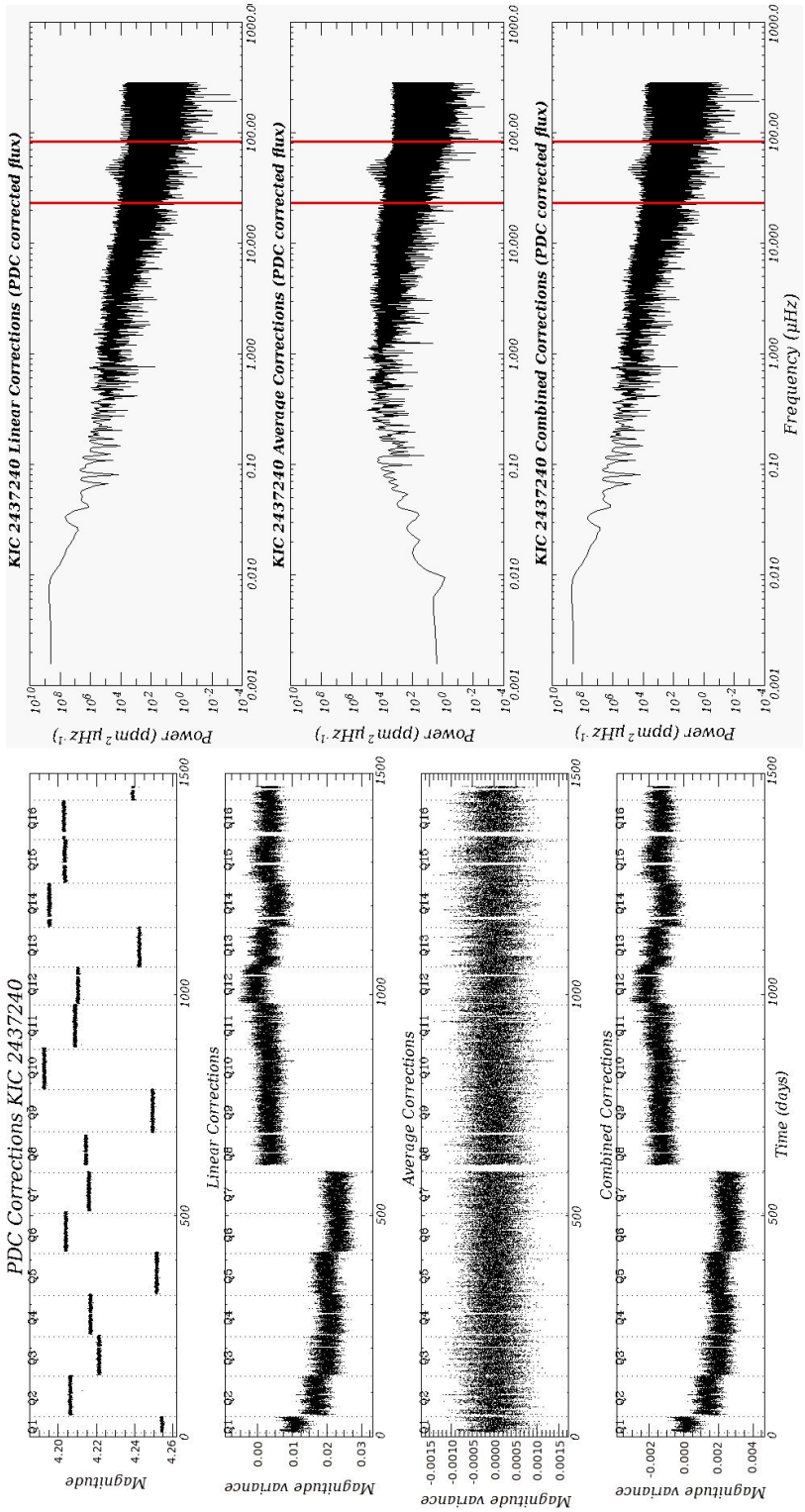

Figure 4.1: Left: The SAP PDC corrected data followed by the jump corrected data using the various alignment methods. From top to bottom; SAP PDC data, linear corrections, average correction, and combined corrections. *Right*: The corresponding power spectrum of the corrected light curves used to determine if any further processing is required. From top to bottom; Linear corrected power spectrum, average corrected power spectrum and combined corrected power spectrum. The oscillation signal can be seen between the two vertical red lines in the power spectrum. The non-white noise is significantly lower in the average corrected spectrum allowing for the signal to noise ratio to increase, suggesting this is the preferred alignment method.

Failure of Modules

After only 9 months of operation, one of the CCD modules failed leading to a consistent temperature drop within a number of onboard systems. The failure of Module 3 was caused by the circuitry powering the module. It was concluded when evaluating Module 3 that the chance of a subsequent failure was remote, supported by the fact that the remaining Modules continued operating until the completion of the mission, except of course for Module 7, which failed in Q17. The remaining 19 Modules continued to work effectively until the end of the mission. As a result of Module 3 failing, 20% of the FOV experienced missing data in one quarter per year, resulting in less data for all 206 stars in the region of NGC 6819, limiting the resolution of detected oscillations.

Safe Modes

The *Kepler* spacecraft experienced unanticipated interruptions to observations, due to sensitivity to cosmic radiation or an unanticipated response to a command sequence. While these events are unexpected, it is not out of the ordinary for a newly-commissioned spacecraft to experience these teething issues (Christiansen & Van Cleve 2011). These interruption events will cause the spacecraft to enter what is called a 'Safe Mode', where non-essential systems such as the CCD electronics will be shut down to preserve the spacecraft while normal operations are recovered. Figure 4.3 shows the affect of a safe mode event on a light curve at ~ 15 days, where the electronics were turned off and the previously collected data was only available for retrieval when the spacecraft was recovered. The photometric trend in the data seen after safe mode recovery, highlighted in red circles, was identified as a thermally induced focus change due to heating from the base of the spacecraft, where the majority of the electronics were housed. (Christiansen & Van Cleve 2011). As a result of these safe modes occurring early on in the mission, the *Kepler* science team had mitigated this effect through improvements in the PDC pipeline.

Not all safe mode events will be triggered the same way and cause the same features to appear, thus they may not be able to be caught by any previous improvements made to the PDC module of the *Kepler* pipeline. The early corrections to the PDC pipeline were not able to correct for some of these events, as can be seen in Figure 4.2, which shows the SAP data and the PDC corrected data in the top panel (red and black, respectively). The bottom panel shows my interactively corrected light curve. The safe mode can be identified by the slowly decreasing/increasing trend after a significant change in the measured magnitude. A safe mode that was not effectively corrected for by the PDC procedure can be seen in Q2 of the top panel. In an attempt to correct for this event, I tried several variations of high pass filters and polynomial corrections. As can be seen in the lower panel of Figure 4.2, significant scatter still exists in the Q2 data, thus I was not able to correct for this safe mode event completely, and decided to exclude it from the analysis. Another safe mode event is visible in Q15 (top panel), that still required some correction after the PDC corrections were applied. I was able to make effective corrections for this safe mode event by applying a high pass filter to the affected quarter.

Loss of Fine Pointing

The *Kepler* spacecraft had occasionally lost the capability to maintain precision pointing. This was caused by momentum dumping from the reaction wheels, or any time the spacecraft makes a minor manoeuvre for realignment or communication to mission control. The Loss Of Fine Pointing (LOFP) control will render the collected data during this period with no better precision than 1%, meaning that the precision of the stars position and flux measurements could not be

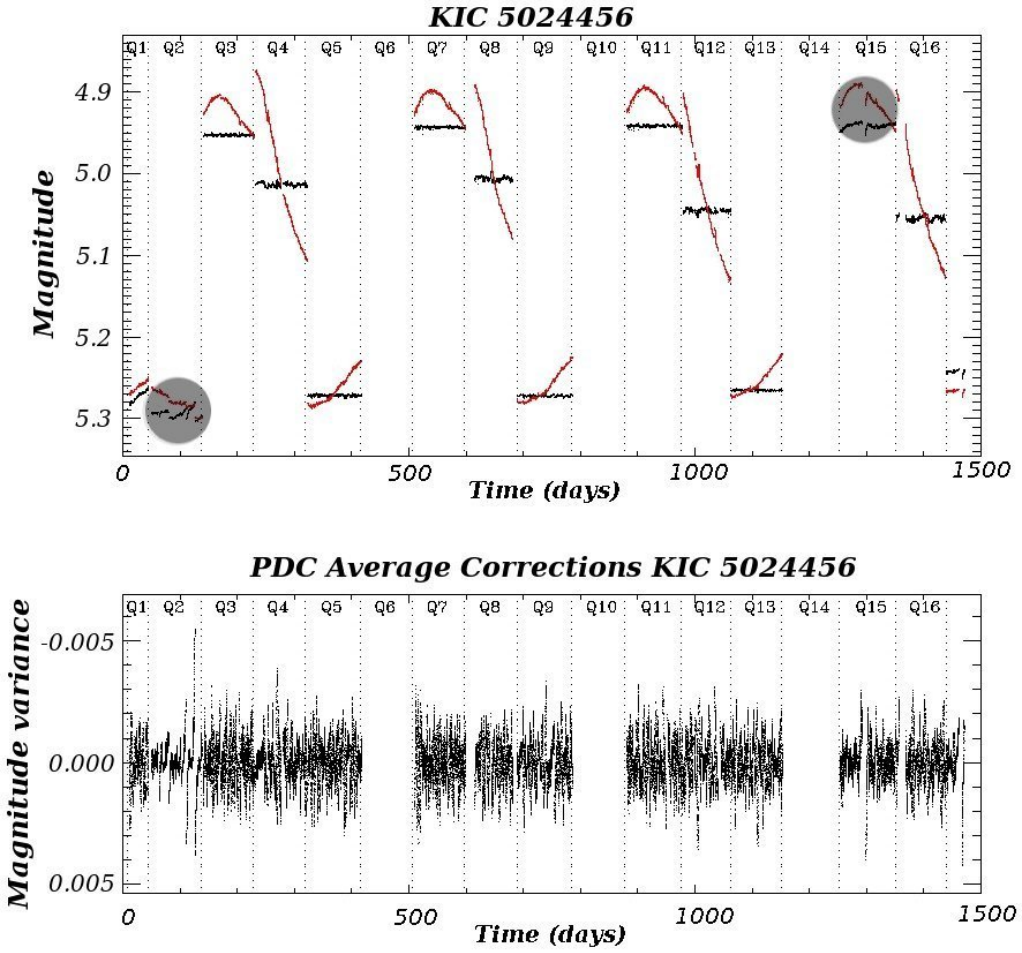

Figure 4.2: Top: SAP data (red), PDC corrected data (Black); *Bottom*: My interactive algorithm corrections and alignment. Q2 shows a safe mode, highlighted in grey, that isn't corrected for effectively. This quarter was removed from analysis after attempts to correct it failed. Q15 has a safe mode event that was corrected for using the PDC procedure however the quarter still required further correction. This was corrected using the additional processing options in my alignment algorithm.

guaranteed. This is classified as lost data by the pipeline and can be analysed if photometry of 1% precision are of scientific interest. This is not the case for asteroseismology, so I leave the LOFP data as missing from the light curve. There is no procedure available within the *Kepler* science pipeline or my interactive algorithm to correct for the missing data from loss of fine pointing.

Attitude Tweaks

Occasional attitude tweaks were necessary early on in the mission to avoid the target aperture moving off the desired pixels due to continued drift (Figure 4.3). Small attitude adjustments were made to ensure that the largest distance between the expected and actual location of a star in its aperture remained below 0.1 of a pixel. These "tweaks" were necessary in Q2 data, as seen in Figure 4.3, which introduced flux discontinuities in the data. As seen in the PDC corrected light curve of Figure 4.3 (red curve), the *Kepler* pipeline has not been able to completely compensate for these discontinuities. Later improvements to the Flight Guidance System greatly reduced the

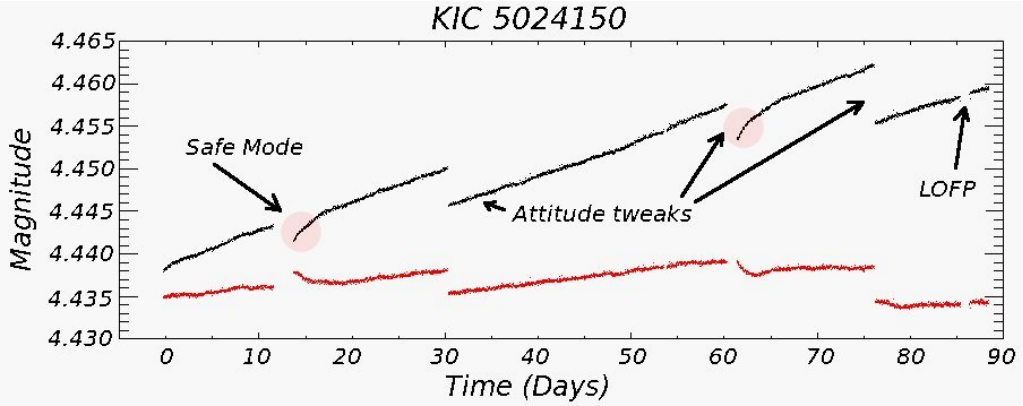

Figure 4.3: SAP (black), PDC corrected (red) light curves of Q2 data for KIC 5024150. The PDC corrected light curve has been shifted down for clarity. A safe mode is observed at ~ 15 days into Q2 observations, with additional attitude tweaks to adjust for drift at ~ 30, ~ 60 and ~ 75 days. A loss of fine pointing (LOFP) is seen at ~ 85 days

need for these attitude tweaks by diminishing the boresight drift.

Several safe modes have been encountered throughout the *Kepler* mission, and are typically corrected with the improved procedures to the PDC pipeline. Attitude adjustments create discontinuities in the data that require specialised algorithms to compensate for the jumps (García et al. 2011). As a result of multiple discontinuities in the data, I had to decide on a case by case basis on how to compensate for these signatures. The interactive algorithm that I developed allowed for additional processing on each quarter individually or on the entire corrected light curve. I have not implemented the algorithms specified in García et al. (2011), as this would require a large amount of effort to analyse a small amount of data ($\sim 2\%$ of stars in my sample). I found that in some cases I was unable to correct for these signatures effectively. Such is the case for KIC 5024150, thus I decided to remove the affected quarter from the analysis.

4.2.2 PDC Corrected Aligned Data Characteristics

While significant effort has been invested to preserve any natural variability in the corrected light curves, it is not possible to preserve all general stellar variability. The PDC process is known to distort astrophysical features in a subset of the corrected light curves, therefore I still see some features in the data that were not corrected for, and that I need to account for when analysing each star. Some of the more prominent characteristics encountered are discussed below.

Varying Scatter

On close inspection of the light curves, some appeared to indicate inconsistencies in the scatter about the average flux level from quarter to quarter. This can be caused by added noise from nearby sources leaking into the pixels of interest (pixel mask). Alternatively it could be a result of the varying gain between each CCD as the star is observed in different quarters. I was able to determine that the difference in scatter is caused during the PDC correction process. The PDC pipeline applies the corrections to the data after the data is shifted to a zero point. A scaling is then applied when the data is normalised, corrected and rescaled back to its original mean flux level. This results in each quarter being normalised by different amounts, causing the various scatter we see. I was able to correct for these inconsistencies by scaling the affected quarters.

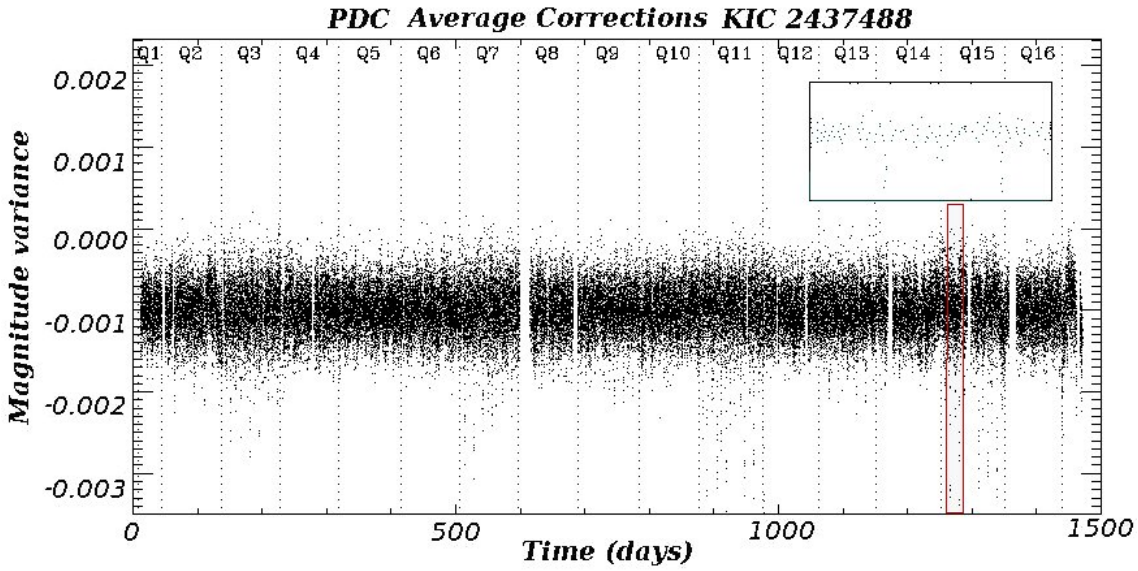

Figure 4.4: The corrected light curve of KIC 2437488 using the average alignment method for stitching. This light curve indicates the relative depths of the eclipses, shown inset, in the different quarters. Quarters 3,7,11, and 15 indicate a strong signal from the eclipse, while quarters 9 and 13 still shows the eclipse signal, but with a significantly less amplitude. Inset is a zoom of the red box showing two primary eclipses and a secondary eclipse from Quarter 15.

Eclipses

Eclipses were found in a number of light curves, many of which only appeared in one quarter of a year's observations, thereby appearing in every fourth quarter as seen in Figure 4.4. This suggests that the eclipsing signal is from a nearby star near the edge of the pixel mask. The relative depth of the eclipsing signal in each quarter can be attributed to a change in the pixel mask because the star falls in a different position relative to the CCD in each quarter. To reduce the effect of the eclipse on the analysis of the data, I removed the eclipse signal from the data. The eclipse signal was removed by first determining the period and duration of the eclipse. An initial estimate for the period was obtained using Period04 (Lenz & Breger 2005) on the individual affected quarters, thereby getting a value for each quarter. This was accomplished by determining the frequency of the strongest narrow peak in the power spectrum. The full stitched light curve was then folded into a phased light curve to determine an accurate fit to the period, and the eclipse duration was then determined. Each eclipse was then located in the uncorrected data and the section of data containing the eclipse was removed. I estimate the eclipse signal in the KIC 2437488 light curve has a period of ~ 7.235, days and a duration of ~ 6 hours. Stello et al. (2011b) found this same eclipsing signal in the first four months of *Kepler* data, and removed Q3 from their analysis to avoid strong bias in the measurement of the asteroseismic parameters. I retain all affected quarters with the eclipse signal removed as described above. Each case of an eclipse signal was individually examined to estimate the period and duration of the eclipse. I found that for some cases, e.g. KIC 2569488, the eclipse duration was a significant fraction of the period (period ~ 1.25 days; eclipse duration ~ 7.2 hours). For these cases, the affected quarters were removed as the eclipse removal process described above would remove a significant amount of the data and the remaining data would not improve the analysis.

Under/Overcorrection

As with the safe mode events, not all PDC corrections are effective. It can be seen in the top panel of Figure 4.5 that Q5, Q9 and Q13 seem unaffected by the PDC correction process. The reader will note that these quarters correspond to the same CCD. An under/over-correction can be identified by comparison with the rest of the light curve and the SAP data. When most quarters have a similar signal in the SAP data and are processed through the PDC corrections, it is expected that they will continue to have a similar signal to each other. Thus when there is a difference between the quarters after a correction is applied, the effect is implied to be an under or over-correction of the SAP data.

Corrections were applied to these quarters (Q5, Q9 and Q13) using the PDC module corrections, however it is apparent that they require further corrections. The magnitude of a red giant star is not expected to vary by more than a mmag, suggesting that any deviation of more than this, indicates further processing is required. Since the trend in the affected quarters (Q5, Q9 and Q13) seems to have a similar frequency of below 0.5μHz it is possible to apply a high pass filter to attenuate the power of all frequencies below this frequency. As can be seen by the bottom panel in Figure 4.5, the high pass filtering applied provides smoother discontinuities in the light curve for analysis.

The safe mode event in Q17 is associated with the failure of the second reaction wheel, discussed in section 4.2.1, which resulted in the *Kepler* mission to cease observations. Since this is limited to only 32 days of data, I exclude this quarter from the analysis.

4.2.3 The Affect of the Data Characteristics on the Time Series Analysis

While attempts were made to mitigate all non-astrophysical signals from the data, such as the safe mode events, attitude tweaks and under/over-corrections of the PDC corrected data. I was not able to correct for all of these features using my interactive alignment algorithms which included additional processing such as high pass filtering, polynomial detrending and outlier removal. Where significant discontinuities remained, I decided to exclude the affected quarter from the analysis, resulting in the exclusion of a total of 12 individual quarters from a total of 7 stars.

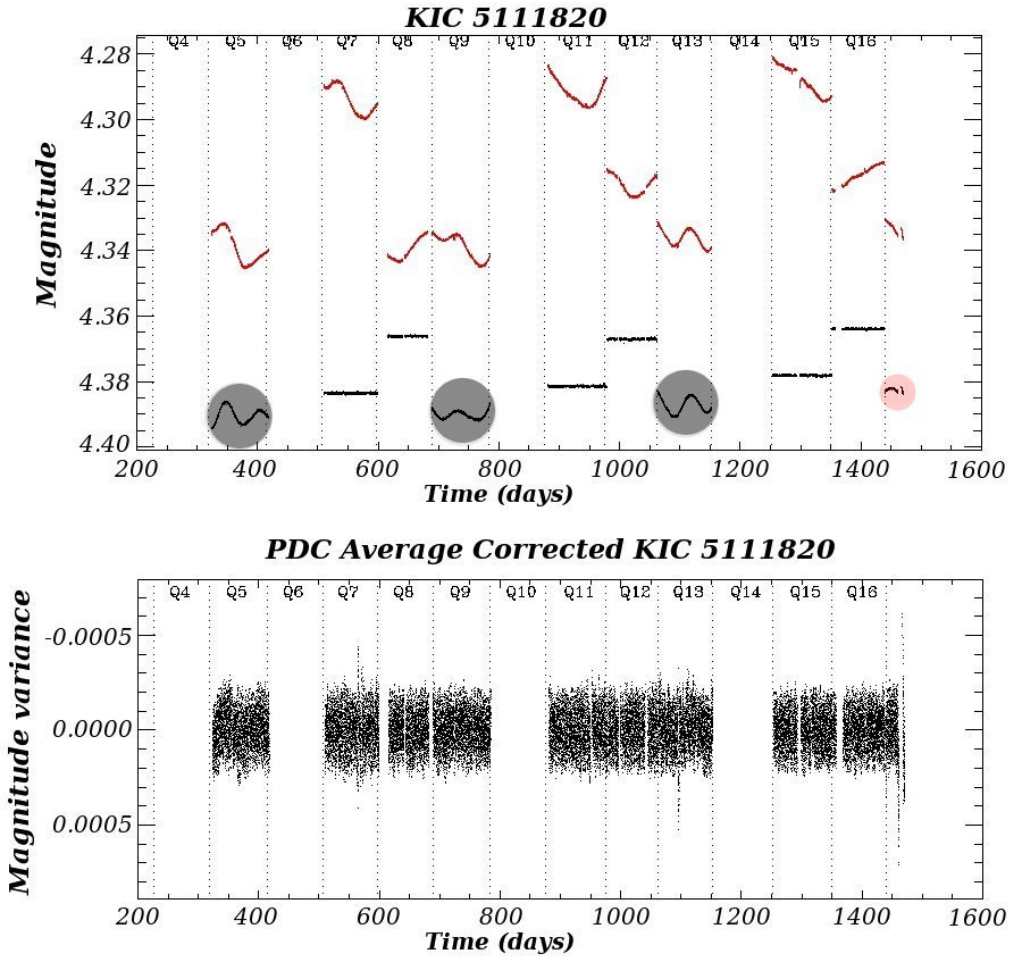

Figure 4.5: Top: SAP data (red), PDC corrected data (Black); *Bottom*: My interactive algorithm corrections and alignment. Quarters 5, 9, and 13 show signatures of under corrections of the SAP data made by the PDC pipeline highlighted in grey. Alternatively, the remaining quarters (7, 8, 11, 12, 15 and 16) were over corrected by the PDC pipeline. I took quarters 5, 9, and 13 to be under corrected and they were corrected using the additional processing options such as high pass filtering, polynomial detrending and outlier removal available in the alignment algorithm I developed. The safe mode event in Q17, highlighted in red, is a result of the failure of the second reaction wheel. This quarter was excluded from the final analysis.

Chapter 5

Membership Analysis

5.1 Introduction

We have seen that asteroseismology can be used to infer the sound speed inside the star (Section 2.4), thus inferring some physical properties of the star, M, R, and T_{eff}. The common age and chemical composition of clusters allows us to compare the asteroseismic parameters of individual stars in the field with the cluster mean. Any deviation from the cluster mean suggests that the implied absolute magnitude, and thus distance, of the star is under or over estimated. Therefore, this indicates that the star in question is a fore- or background star. Hence, I can use asteroseismology to determine whether a star is a likely member of the cluster independently of distance, interstellar absorption or reddening of the cluster.

5.2 Extraction of Asteroseismic Parameters

Kepler has returned large amounts of data for the four years of observations, meaning that scientists have a long road ahead to analyse the data. In order to extract as much information in as little time as possible, scientist use automated pipeline code to analyse multiple stars simultaneously, or in quick succession. This allows them to extract the information from a large sample of stars in a short period of time. Several automated pipelines were developed during the early phases of *Kepler's* observations to extract various asteroseismic properties. Mathur et al. (2010) describe an automated pipeline, A2Z, that calculates the global parameters (rotation period, mean large frequency spacing $\Delta\nu$, and the maximum amplitude A_{max}), which have been tested on simulated stars and applied to real data from CoRoT. Verner & Roxburgh (2011) attempted to automatically detect a number of asteroseismic parameters using autocorrelation on the power spectrum. Additionally, pipelines have been developed in the framework of the asteroFLAG project (Chaplin et al. 2008; Mathur et al. 2009; Huber et al. 2009) through Hare & Hounds exercises. Hare & Hounds exercises comprise of one group (the *Hounds*) analysing the simulated data that was produced by the other group (the *Hares*) without knowing any of the parameters that the simulations were based on. The results of these pipelines, and others, have been compared in order to develop an understanding of the different methods employed. Hekker et al. (2011b) found that the results of seven different pipelines agreed to within a few percent and therefore appear to be fairly robust against the different methods used. Therefore the choice of pipeline used will not make a significant difference in the results obtained for most stars. I used the pipeline code, SYD, developed by Huber et al. (2009) that attempts to extract the asteroseismic properties $\Delta\nu$ and ν_{max} by using an

autocorrelation function to estimate where the power excess occurs, which I modified to suit the current project.

The SYD pipeline is discussed in detail in Huber et al. (2009), however, I provide a brief description of how the pipeline works. The basic analysis steps covered by the SYD pipeline are: 1. Estimating the location of the power excess, ν_{max}, in the power spectrum; 2. Calculating an improved background model; and 3. Estimating the mean large frequency separation, $\Delta\nu$.

1. To estimate the location of the power excess, the pipeline first models the background by smoothing a binned power spectrum. This background is subtracted to form a residual power spectrum (Figure 5.1, top panel) which is divided into subsets of roughly equal length. The autocorrelation function (ACF) is calculated for each subset after the mean of each subset is subtracted (Figure 5.1, middle panel). The ACF of each subset is collapsed over all frequency spacings and a gaussian function is fitted to the peak to estimate the position of the power excess (Figure 5.1, bottom panel). The centre of the gaussian is taken as the measurement of the frequency of maximum power, ν_{max}. The advantage of the collapsed ACF over smoothing is that it will be more sensitive to the regularity in the peaks, as opposed to just their strengths, thereby using the fact that the peaks are expected to be regularly spaced.

2. The background is modeled with an extended Harvey model suggested by Karoff (2008), which is a more physically realistic interpretation of the stellar background. The extended Harvey model allows for a steeper slope at high frequencies, corresponding to granulation, and a shallower slope at low frequencies, corresponding to turbulence (Nordlund et al. 1997). The granulation timescales are estimated by scaling from the solar values, using the $\nu_{\rm max}$ estimated in the previous step (Kjeldsen & Bedding 1995). Despite the granulation signature of hotter stars being quite different to the Sun, Huber et al. (2009) found the scaling produces a satisfactory approximation to the initial background values.

3. To estimate $\Delta\nu$, the background-corrected time series is divided into overlapping subsets and the power spectra of each subsets are co-added, forming a smoothed power spectrum. The power excess calculations are repeated to obtain a more accurate measurement of $\nu_{\rm max}$ by fitting a gaussian to the background-corrected power spectrum and taking the peak as the new $\nu_{\rm max}$ estimate. A new estimate for the expected $\Delta\nu$, $\Delta\nu_{scaled}$, is calculated based on the correlation between $\nu_{\rm max}$ and $\Delta\nu$, as seen in Equation 2.6. An average large frequency separation is then determined using an autocorrelation of the power spectrum for the region $\nu_{\rm max} \pm 10\Delta\nu_{scaled}$ and fitting a gaussian function to the dominant peak in the vicinity of $\Delta\nu_{scaled}$.

The SYD pipeline was developed to analyse the maximum number of stars possible in a sample, meaning it is capable of analysing most types of stars, from main sequence to red giants. Testing was performed on 1,936 simulated stars representative of *Kepler* stars that span the HR diagram, from low-mass main-sequence stars to evolved sub giants. Huber et al. (2009) found that the SYD pipeline was able to recover the true $\nu_{\rm max}$ and $\Delta\nu$ values for 70% and 60% of stars respectively. Where the pipeline was not able to recover the $\nu_{\rm max}$ or $\Delta\nu$, it would return a 0. The value of the amplitude of each frequency bin in the power spectrum will have an inherent uncertainty related to the uncertainty in the time series. To simulate this, the SYD pipeline generates 500 realisations of the power spectrum, by randomly varying the amplitude of each frequency bin by following a χ^2 distribution with 2 degrees of freedom. The measurments for $\nu_{\rm max}$ and $\Delta\nu$ are

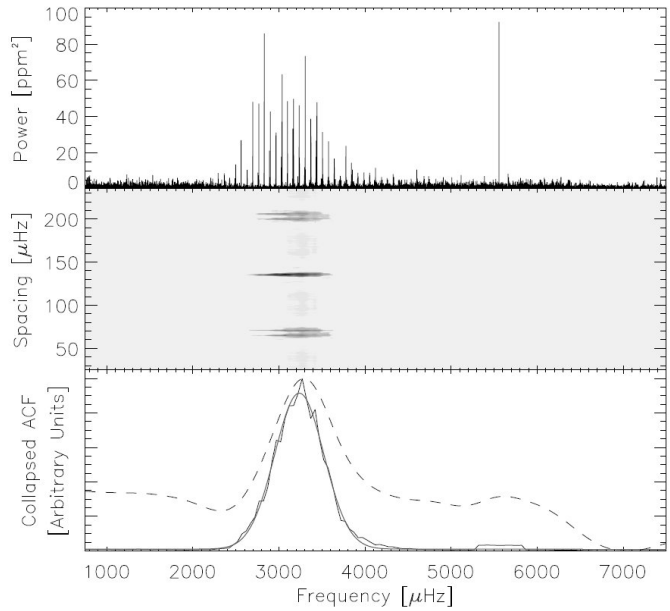

Figure 5.1: Procedure for locating the power excess using a 30 day subset of VIRGO photometry. *Top panel:* background-corrected power spectrum. *Middle panel:* Autocorrelation as a function of frequency spacing and central frequency of the subset at which the correlation is evaluated. Dark colours are regions of high correlation. *Bottom panel:* Collapsed ACF (black solid line) and smoothed power spectrum (dashed line). The grey solid line shows a gaussian fit to the collapsed ACF.
Figure credit: (Huber et al. 2009)

obtained for each iteration which enables me to describe the uncertainty in the measured asteroseismic properties. The uncertainties are taken as the standard deviation of these 500 values using the Tukey's Biweight (Hoaglin, Mosteller & Tukey 1983) method to weight the points for a robust estimate.

Huber et al. (2009) noted that modifications would be required for processing low frequency oscillations in red giant stars. I performed the required modifications by providing boundaries for the region of interest for each star. The region of interest is defined by the frequency bounds that incorporate any oscillation signal in full. I rounded the upper and lower frequency bounds, up and down respectively, to the nearest interval in log space. Modification to these boundaries allowed for improving the background fitting parameters specific to each star. This meant that the light curves and power spectrum of each star were visually inspected to ascertain the frequency range of interest. This region specifies to the pipeline the frequency region that contains the oscillation signal, as well as describing the locations of upper and lower bounds for fitting of the background, where the noise is dominated by the end of granualtion at low frequency, and where white noise begins to dominate at high frequency. The region of interest was maximised when there was no obvious signal present. Where there was a signal, the region of interest was minimised to reduce the influence from the background while still containing the complete signal. The improved background fitting parameters were included in a file for each individual star, which the pipeline would use to set up some initial conditions for processing that star, enabling the pipeline to use specific parameters for each star. These modifications meant that the region of interest could be fine tuned to avoid any contamination from more than one pulsator blending into the observations, such as KIC 5024582 as seen in Figure 5.2. This fine tuning greatly reduced the influence of the

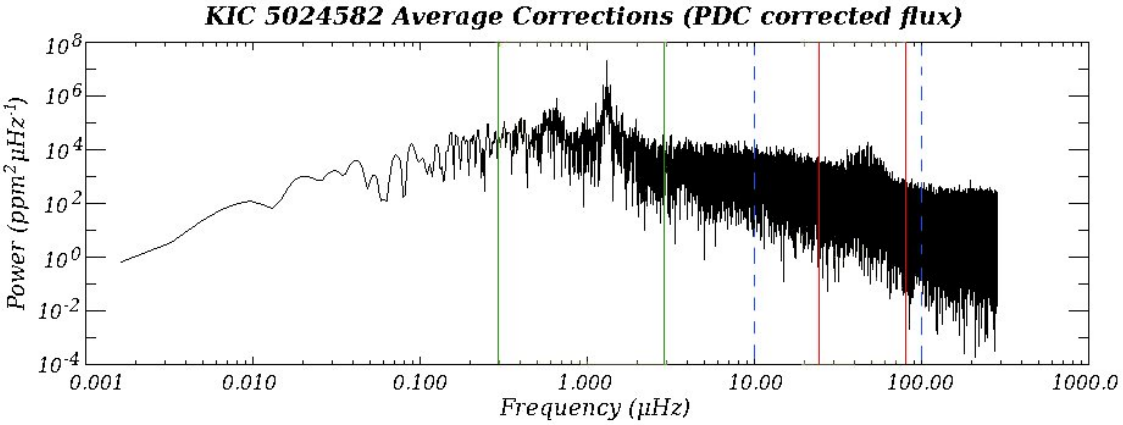

Figure 5.2: Power spectrum in log-log scale of the corrected light curve from KIC 5024582. The two regions inside the green and red vertical lines indicate signals of excess power where the pipeline could be used to extract a value for $\nu_{\rm max}$ and $\Delta\nu$. The modification of the boundaries for the region of interest (blue dashed lines) allowed both regions to be analysed independently. The excess power at $\sim 1\mu$Hz is a result of a blended signal from a W UMa variable star, KIC 5112741.

blended signal on the power excess calculations or the background fitting. The two regions in Figure 5.2 could be analysed independently to find $\Delta\nu$ and $\nu_{\rm max}$ estimates without the influence of the other. It appears obvious that at least one of the signals is a blend of another star within the target pixels. I found that the signal around 1μHz , within the green lines, is consistent with the blended signal from a large amplitude contact binary, W UMa variable (KIC 5112741), in agreement with Stello et al. (2011b).

Each star was analysed individually through the SYD pipeline, and accepted or rejected on the basis on the following three criteria:

1. An acceptable background fit to the data (left panel of Figure 5.3);
2. An acceptable gaussian fit to the background-corrected power spectrum, to estimate ν_{max} (right panel of Figure 5.3); and
3. An acceptable estimate of $\Delta\nu$ (Figure 5.4). The acceptability of the fit at each stage was determined by eye given these figures.

The background fitting was performed on the power spectrum with the region of excess power removed, so the background model was not affected by the oscillation signal. The left panel of Figure 5.3 shows the region of interest removed from the power spectrum (black line) with the background model overlaid (thick blue line). The smoothed power spectrum (yellow line) is also shown to represent the extent to which the signal is removed from interfering with the background. The $\nu_{\rm max}$ estimate is shown as a blue diamond in the right panel of Figure 5.3, where the background-corrected power spectrum in the region of interest is shown. The $\nu_{\rm max}$ estimate is taken as the peak of the gaussian fit to the smoothed background-corrected power spectrum (red line). If the blue diamond did not correspond to a similar location to the middle of the power excess, the fit was deemed unacceptable. Additionally, if the gaussian fit to the smoothed background-corrected power spectrum did not seem to cover the full range of the signal, the fit was rejected. The background fit and the $\nu_{\rm max}$ estimate could be improved by fine tuning

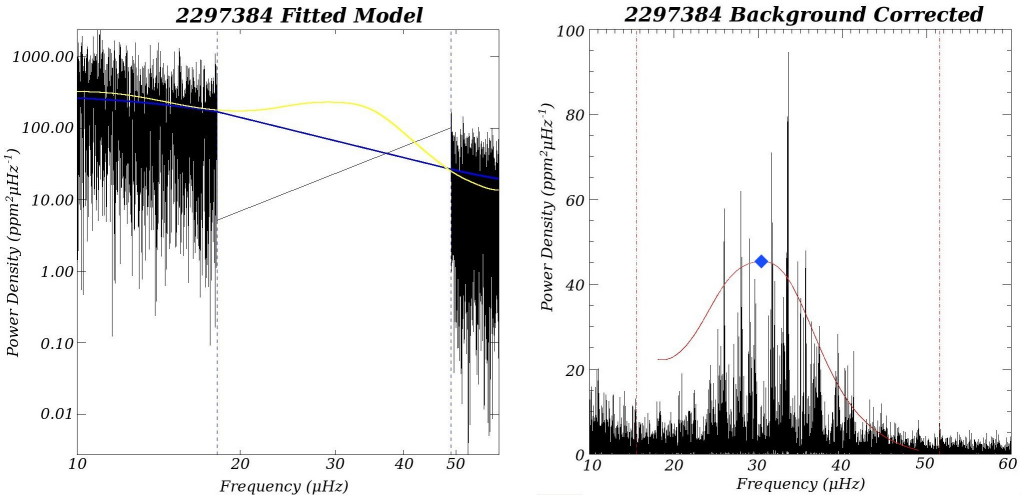

Figure 5.3: Left: A section of the power spectrum of KIC 2297384 containing excess power. The region enclosed in the dashed lines contains the excess power, which is removed for the background fitting (blue line). The yellow line shows the smoothed power spectrum to indicate the extent of the excess power. *Right:* A section of the power spectrum of KIC 2297384 is shown after the background corrections have been performed. The excess power is clearly centred around 30 μHz as shown by the gaussian fit to the region inside the red dahsed lines. The estimated $\nu_{\rm max}$ is taken as the peak of the gaussian (blue diamond). The red dahsed lines indicate the region for which $\Delta\nu$ will be evaluated.

the additional background fitting-parameters that I implemented in the pipeline to improve the processing of highly evolved red giant stars. When making a decision for the acceptability of the fit for $\Delta\nu$, I examined the corresponding fitted model, Figure 5.4, for each individual star. Panel a) shows the ACF of the smoothed background-corrected power spectrum. The vertical red dashed line indicates the solar scaled $\Delta\nu$ value, i.e. the expected $\Delta\nu$ value based on the measured ν_{max}. The red line highlighting a single peak in the ACF indicates the closest peak to the expected value. The $\Delta\nu$ value is taken as the peak of the gaussian function that is fitted to this peak, as seen in panel b), (green line). This value is then checked using the échelle diagram, panel c) where the power spectrum is divided up into equal segments of $\Delta\nu$ and stacked on top of each other as described in Section 2.4. Here the bright colours indicate the location of the p-mode oscillations $l = 1, l = 2, l = 0$ as labeled, with the panel extended to double $\Delta\nu$ for clarity. If the échelle diagram (Figure 5.4 panel c)) indicated straight vertical lines for the oscillation modes, the $\Delta\nu$ value was deemed to be acceptable.

5.3 Estimating Solar Scaled Parameters

I use the independent method of asteroseismic membership introduced by Stello et al. (2010b), to categorize my selected stars as cluster members or likely non-members. Stello et al. (2011b) used this same approach with 10 months of *Kepler* data (Q1-Q4) to determine membership of *Kepler* red giants in NGC 6791 and NGC 6819. They were able to confirm four previously identified non-members of NGC 6819, despite having better than 80% probability of membership from radial velocity measurements (Hole et al. 2009; Platais et al. 2011), and assuming a single star classification. They found additional stars that disagreed with previous membership studies of NGC 6819 and NGC 6791, two additional stars for NGC 6819 and one in NGC 6791. I was able to use almost five times as much data to determine stellar membership of the two clusters selected,

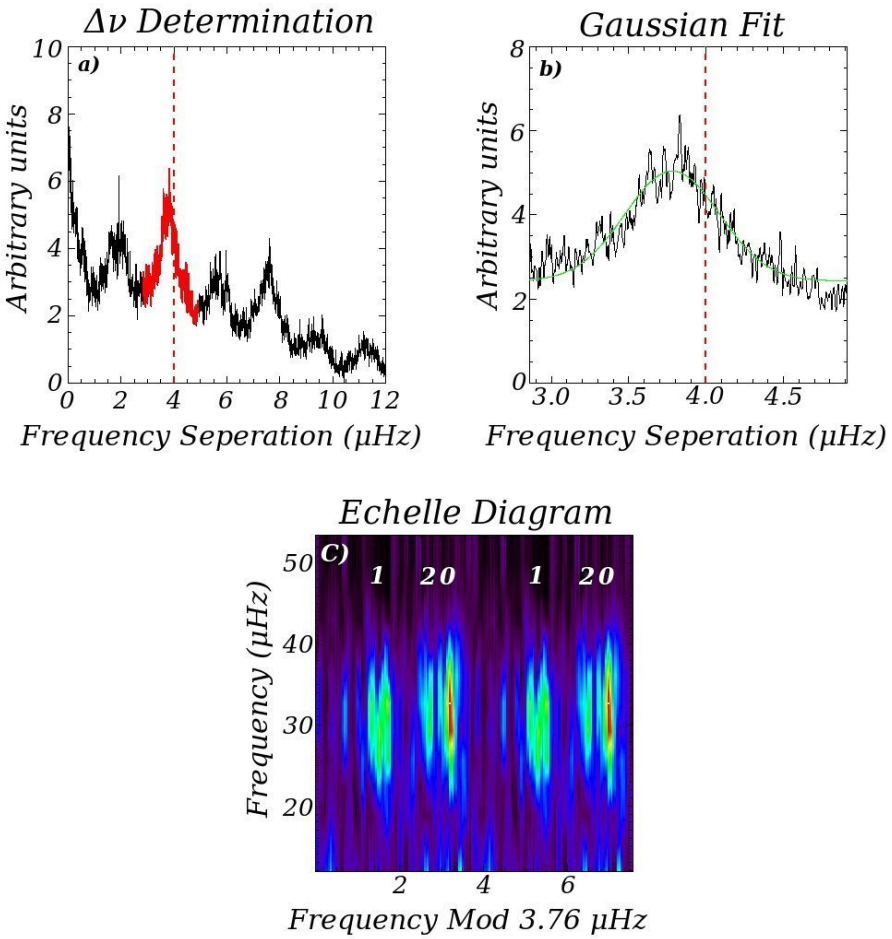

Figure 5.4: Panel a) shows the autocorrelation function of the region of excess power in Figure 5.3. The red dashed line indicates the expected $\Delta\nu$ value based on solar scaling from the $\nu_{\rm max}$ estimate. The highlighted red line indicates the closest peak to this expected $\Delta\nu$ value. Panel b) A gaussian curve is fitted to the peak from panel a) to obtain an accurate estimate of the regular frequency spacing. The $\Delta\nu$ estimate is confirmed using panel c), the échelle diagram, where vertical ridges are expected for each mode degree identified.

NGC 6791 and NGC 6819. As discussed, I use the SYD pipeline to extract both $\nu_{\rm max}$ and $\Delta\nu$ for all of the stars targeted individually in the region of the two clusters. Using the well known scaling relations (Ulrich 1986; Mosser et al. 2010; Brown et al. 1991; Kjeldsen & Bedding 1995)

$$\nu_{\rm max} \approx \frac{M/M_{\odot}(T_{\rm eff}/T_{\rm eff,\odot})^{3.5}}{L/L_{\odot}}\nu_{\rm max,\odot} \tag{5.1}$$

$$\Delta\nu \approx \frac{(M/M_{\odot})^{0.5}(T_{\rm eff}/T_{\rm eff,\odot})^{3}}{(L/L_{\odot})^{0.75}}\Delta\nu_{\odot} \tag{5.2}$$

where $\Delta\nu_{\odot} = 135.1 \pm 0.1$ μHz , $\nu_{\rm max,\odot} = 3090 \pm 30$ μHz and $T_{\rm eff,\odot} = 5777$ K, I was able to make estimates of the expected values and infer cluster membership through any deviation of the measured value from the expected value. Here, the uncertainties in the solar values produce a variation in the expected values by less than 0.1% and 1% for $\Delta\nu$ and $\nu_{\rm max}$ respectively, thus do not influence the membership classification. I note that due to the high correlation of $\Delta\nu$ and $\nu_{\rm max}$

(Stello et al. 2009; Hekker et al. 2009), it is only for redundancy that both parameters are used for membership determination. However, I place a higher significance on the measured value of $\Delta\nu$ as it is known to be more precise and physically more well understood (Stello et al. 2009, 2011b; Verner et al. 2011).

I have already described the process of extracting the measured values of $\nu_{\rm max}$ and $\Delta\nu$ in section 5.2. In order to infer cluster membership, I need to compare the measured values of $\nu_{\rm max}$ and $\Delta\nu$ with the expected values, $\nu_{\rm max,scaled}$ and $\Delta\nu_{scaled}$. This requires the M, L and $T_{\rm eff}$ parameters for each star to be known in order to calculate the expected values from Equations 5.1 and 5.2. The masses of the red giant branch stars are not expected to be different from each other at the 1% level (Marigo et al. 2008), and can be assumed to be equal for my purposes. I therefore adopt the average red giant mass from Basu et al. (2011), of $M_{RGB} = 1.20 \pm 0.01 M_{\odot}$ for NGC 6719 and $M_{RGB} = 1.68 \pm 0.03 M_{\odot}$ for NGC 6819. However, since the red clump stars are not included in this study, it is likely that I will see a systematic overestimation of $\Delta\nu$ for the red clump stars if significant mass loss has taken place near the tip of the red giant branch. I obtained accurate photometry of each star from Stetson, Bruntt & Grundahl (2003) and Hole et al. (2009) for NGC 6791 and NGC 6819, respectively. I converted the apparent magnitude into luminosity using the cluster distances of Basu et al. (2011), $(m-M)_0 = 13.11 \pm 0.06$ and $(m-M)_0 = 11.85 \pm 0.05$ for NGC 6791 and NGC 6819 respectively. I corrected for bolometric magnitude and interstellar absorption. The interstellar absorption was corrected by using $A_v = 3.1 E_{(B-V)}$, from Roth (2009). I adopted cluster reddenings of $E_{(B-V)} = 0.1$ mag for NGC 6791, which is less than that adopted by Basu et al. (2011), however, it is still within the acceptable range listed in the literature, $0.1 < E_{(B-V)} < 0.16$ (Janes 1984; Worthey 2010; Brogaard et al. 2011). The adopted $E_{(B-V)} = 0.15$ mag for NGC 6819 is consistent with that of Basu et al. (2011). I applied the bolometric correction using the polynomial equations of Flower (1996) and Torres (2010). I found that the bolometric corrections for the cooler stars (i.e. $< 4000K$) were more likely to cause a larger scatter in the observed ratios. This is somewhat expected as the corrections determined for low temperature stars were determined from uncertain angular diameters (Flower 1996). This only had a minor effect on the membership determination of two stars, KIC 2437496 and KIC 2569935, which I have categorised as likely members. All other low temperature stars are considered as non-members.

The asteroseismic membership technique seeks to identify stars that are likely non-members, by distinguishing them from the mean of the cluster. I take into account the relative $T_{\rm eff}$ and bolometric corrections of each star in my sample. I use the calibrations of Ramírez & Meléndez (2005) with the the $V-K$ color index to transform into the T_{eff}, since it is less sensitive to metallicity and shows less scatter in temperature than the $B-V$ color index (Stello et al. 2011b). Propagating the uncertainties gives ~ 28 K and ~ 40 K for NGC 6791 and NGC 6819 respectively, which includes contributions from photometry and metallicity. I expect this to increase by an additional 40 K when accounting for reddening, as suggested by Hekker et al. (2011a).

5.4 Membership determination

The determination of membership of each star was established using the ratio of the extracted values for $\nu_{\rm max}$ and $\Delta\nu$ and the solar scaled values determined using Equations 5.1 and 5.2, tabulated in Tables 5.1 and 5.2. These tables show the measured values of a few selected stars in NGC 6791 and NGC 6819 with the comparative membership classifications from radial velocity membership studies (Platais et al. 2011; Hole et al. 2009), an early seismic study (Stello et al.

2011b) and the classifications from this work. The full tables are available in Appendix A and B.

When the measured properties $\nu_{\rm max}$ and $\Delta\nu$ (Table 5.1 and 5.2) are compared to the solar scaled values, $\nu_{\rm max,scaled}$ and $\Delta\nu_{scaled}$ for an expected member, I was able to specify the membership status of each star. Figure 5.5 shows the observed-to-scaled ratio for those stars that are considered likely members. Each star shows an expected $\Delta\nu$ ratio of 1.0, with a few showing small deviations from the expected ratio. These deviations are predominantly a result of the uncertainty in the $T_{\rm eff}$ (see Equations 5.1 and 5.2) which dominate the uncertainty in the ratio, which is less than 10% (dashed red line). Apart from the few outliers seen in Figure 5.5, I found no systematic difference in the ratios for red giant branch stars compared to the red clump stars. This, in conjunction with the domination of the temperature in the calculations of the expected values $\Delta\nu_{scaled}$ and $\nu_{\rm max,scaled}$, suggests that my original assumption of equal mass of red giant stars, including that of red clump stars, is acceptable.

In addition to performing the asteroseismic membership analysis of the two clusters, I compare the results with that of Stello et al. (2011b), as seen in Tables 5.1 and 5.2. I obtained the measured values of the stars listed in Stello et al. (2011b) along with their scaled values. In addition, I confirmed the scaled values of Stello et al. (2011b) based on my cluster parameters and corrected temperatures. In most cases, there was little difference in the expected values. I found that I was able to confirm all results of Stello et al. (2011b) for both clusters, as seen in Figure 5.5, except for KIC 2568916 which I will discuss in more detail.

Table 5.1: NGC 6791 measured asteroseismic properties

Target ID [a] KIC	Target ID (Stetson)[b]	$\nu_{\max}$ (μHz)	Solar Scaled $\nu_{\max}$ ratio[c]	$\Delta\nu$ (μHz)	Solar Scaled $\Delta\nu$ ratio[c]	Membership (Platais)[d] %	Seismic Membership (Stello) [e]	Seismic Membership This work
2297384	5583	30.41 ± 1.30	0.97 ± 0.08	- [f] $\pm$ -	1.01 ± 0.09	93	Yes	Yes
2297574	8144	199.7 ± 0.01	0.93 ± 0.001	15.18 ± 0.02	0.92 ± 0.04	98	-	Yes
2297793	11539	4.10 ± 0.17	0.38 ± 0.01	0.79 ± 0.01	0.48 ± 0.02	0	No	No
2297825	11957	31.23 ± 1.21	0.98 ± 0.07	3.81 ± 0.03	1.01 ± 0.05	94	Yes	Yes
2436291	2109	367.1 ± 0.94	1.03 ± 0.01	18.67 ± 0.01	0.78 ± 0.03	99	-	No
2436458	2915	37.56 ± 0.60	0.99 ± 0.03	4.15 ± 0.01	0.97 ± 0.05	99	Yes	Yes
2436540	3354	57.49 ± 1.09	1.07 ± 0.04	5.79 ± 0.01	1.04 ± 0.05	85	Yes	Yes
2436543	3369	26.24 ± 0.84	0.85 ± 0.04	3.49 ± 0.02	0.93 ± 0.05	99	Unknown	Yes
2437496	8904	4.42 ± 0.07	0.98 ± 0.03	0.81 ± 0.05	0.99 ± 0.03	99	Yes	Yes
2569935	8266	5.17 ± 0.38	0.92 ± 0.12	0.98 ± 0.05	0.99 ± 0.04	96	Yes	Yes

Table 5.2: NGC 6819 measured asteroseismic properties

Target ID [a] KIC	Target ID (Hole)[g]	$\nu_{\max}$ (μHz)	Solar Scaled $\nu_{\max}$ ratio[c]	$\Delta\nu$ (μHz)	Solar Scaled $\Delta\nu$ ratio[c]	RV Membership (Hole) [h] %	RV Membership (Platais)[d] %	Seismic Membership (Stello)[e]	Seismic Membership This work
4937011	7017	27.73 ± 0.78	0.44 ± 0.03	4.09 ± 0.04	0.69 ± 0.03	-	0	No	No
4937056	2012	45.60 ± 1.34	0.95 ± 0.05	4.77 ± 0.03	0.97 ± 0.04	-	-	Yes	Yes
4937140	12023	9.18 ± 0.13	$0.004 \pm$ -	- ± 1.27	0.08 ± 0.01	93	0	-	No
4937770	9024	63.85 ± 0.21	0.79 ± 0.04	7.85 ± 0.01	1.07 ± 0.04	94	61	Yes	Unknown
5023849	13010	3.11 ± 0.76	0 ± 0	1.21 ± 0.06	0.004 ± 0.001	-	0	-	No
5023863	-	35.67 ± 18.5	$0.004 \pm$ -	6.10 ± 0.04	0.02 ± 0.002	94	99	-	No
5023889	4014	53.56 ± 0.53	2.58 ± 0.14	5.37 ± 0.01	2.07 ± 0.09	-	0	No	No
5023890	9009	1.10 ± 0.03	0 ± 0	0.25 ± 0.07	0.002 ± 0	-	0	-	No
5023931	7009	50.6 ± 1.56	0.98 ± 0.06	4.91 ± 0.01	0.96 ± 0.04	92	99	Yes	Yes
5024582	9002	45.6 ± 1.024	0.95 ± 0.05	4.78 ± 0.04	0.97 ± 0.04	BLM	99	Yes	Yes
5112741	3002	56.26 ± 31.63	1.75 ± 0.09	7.75 ± 0.03	2.14 ± 0.09	93	99	-	No

[a] Only targets for which oscillations were detected are listed.
[b] ID's from Stetson, Bruntt & Grundahl (2003)
[c] A value of 0 is less than 0.0001, effectively 0
[d] Membership probability from radial velocity (Platais et al. 2011)
[e] Seismic membership from Stello et al. (2011b)
[f] SYD pipeline was unable to extract a value.
[g] ID's from Hole et al. (2009)
[h] Membership probability from radial velocity (Hole et al. 2009); BLM: binary likely member.

Stello et al. (2011b) found that despite a large spatial separation, KIC 2568916 seemed to be highly correlated with KIC 2569488. They determined this was a result of a localized strong trend within a narrow time span. They analysed a single quarter, Q4, to avoid the blended signal interfering with the results and found a signal that was consistent with membership, however, I was unable to confirm this classification. A total of 15 quarters were available for analysis, however I found that the correction and alignment of the time series was not adequate for two of the quarters, Q3, and Q4. These two quarters, highlighted in red in the top panel of Figure 5.6 were removed before attempting to extract the asteroseismic parameters, $\nu_{\rm max}$ and $\Delta\nu$. The SYD pipeline code was unable to extract a measurement for these parameters due to difficulties fitting the background and the signal, therefore I examined the uncorrected power spectrum. Figure 5.6 shows the uncorrected power spectrum (middle panel) with the bottom panel showing a zoomed in linear plot of the highlighted region in red. The highlighted region is defined by $\nu_{\rm max,scaled}$ and $\Delta\nu_{scaled}$ assuming membership using Equations 5.1 and 5.2, where the region extends to $\pm 4\Delta\nu_{scaled}$. I decided to calculate the autocorrelation function of the uncorrected power spectrum in this region to try to extract a value for the large separation $\Delta\nu$. The autocorrelation function for this region seen in Figure 5.7 shows the location of $\Delta\nu_{scaled}$ (the red dashed line). I find no significant peak near the expected location. I also note that the amplitude of the noise of KIC 2568916 is consistent with similar stars which have been confirmed as members, and hence not just a member whose photometry is too noisy to detect the oscillation signal. This suggests that KIC 2568916 is not a member of NGC 6791. I make no definitive claim as to the membership of this star, however I err on the side of caution and suggest it may not be a member as suggested by Stello et al. (2011b).

I have analysed 232 and 206 red giant stars around NGC 6791 and NGC 6819 respectively to ascertain the membership to the associated cluster. This is achieved through measuring $\nu_{\rm max}$ and $\Delta\nu$ for each star and calculating the expected values based on membership; if the ratio between the measured and expected value is 1.0 then the star can be considered a likely member of the cluster. I detected solar-like oscillations in over 80% of the stars analysed as seen in Table 5.3, 41% of which have been classified as likely members of one of the two clusters, NGC 6791 and NGC 6819. The comparison of my results with previous work (Hole et al. 2009; Stello et al. 2010b, 2011b; Platais et al. 2011) has allowed me to identify 41 new members of NGC 6791 and four additional new members of NGC 6819, thus increasing the red giant membership population of NGC 6791 by almost 40%.

Table 5.3: Breakdown of star numbers for each cluster.

Cluster	# of stars analysed	# of stars with solar-like oscillations	# of members found	# of new members
NGC 6791	232	208	103	41
NGC 6819	206	145	43	4
Total	438	353	146	45

5.5 Additional Results

By determining the membership of each individual cluster, I was able to show the spatial extent of red giants within each cluster. This will provide a minimum value for the cluster radii. Figures

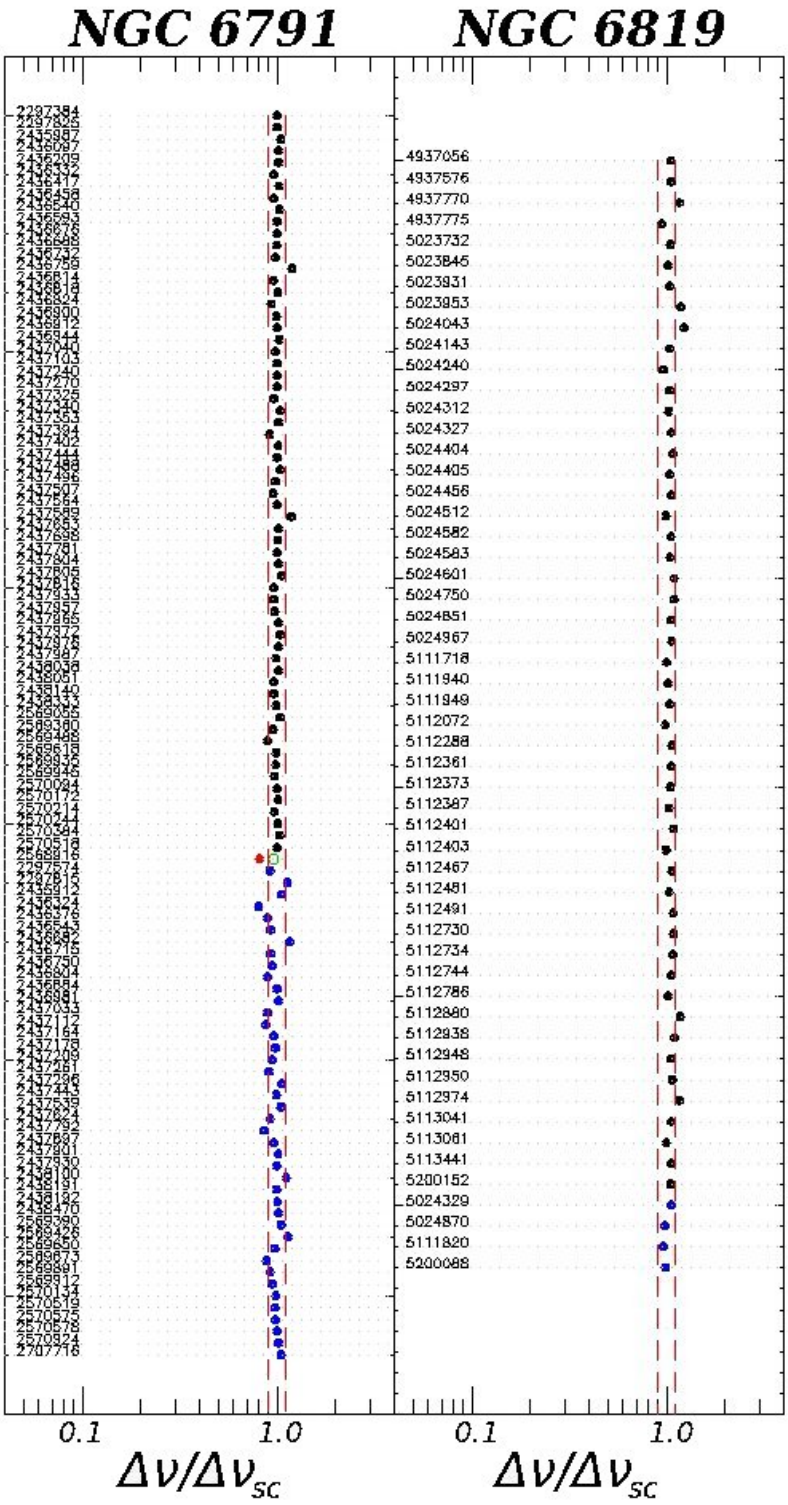

Figure 5.5: Cluster members of NGC 6791 (*left*) and NGC 6819 (*right*) identified by the ratio of the measured $\nu_{\rm max}$ and $\Delta\nu$ parameters to the solar scaled value. The vertical dashed lines are indicative of $\pm 2\sigma$ from the expected ratio of 1. The black dots indicate members from Stello et al. (2011b) that are confirmed in this work. The red dot indicates a member from Stello et al. (2011b) that I could not confirm with certainty, discussed in the text (I note that Stello et al. (2011b) use one quarter, Q4, for KIC 2568916). The blue dots indicate likely new members found by this work.

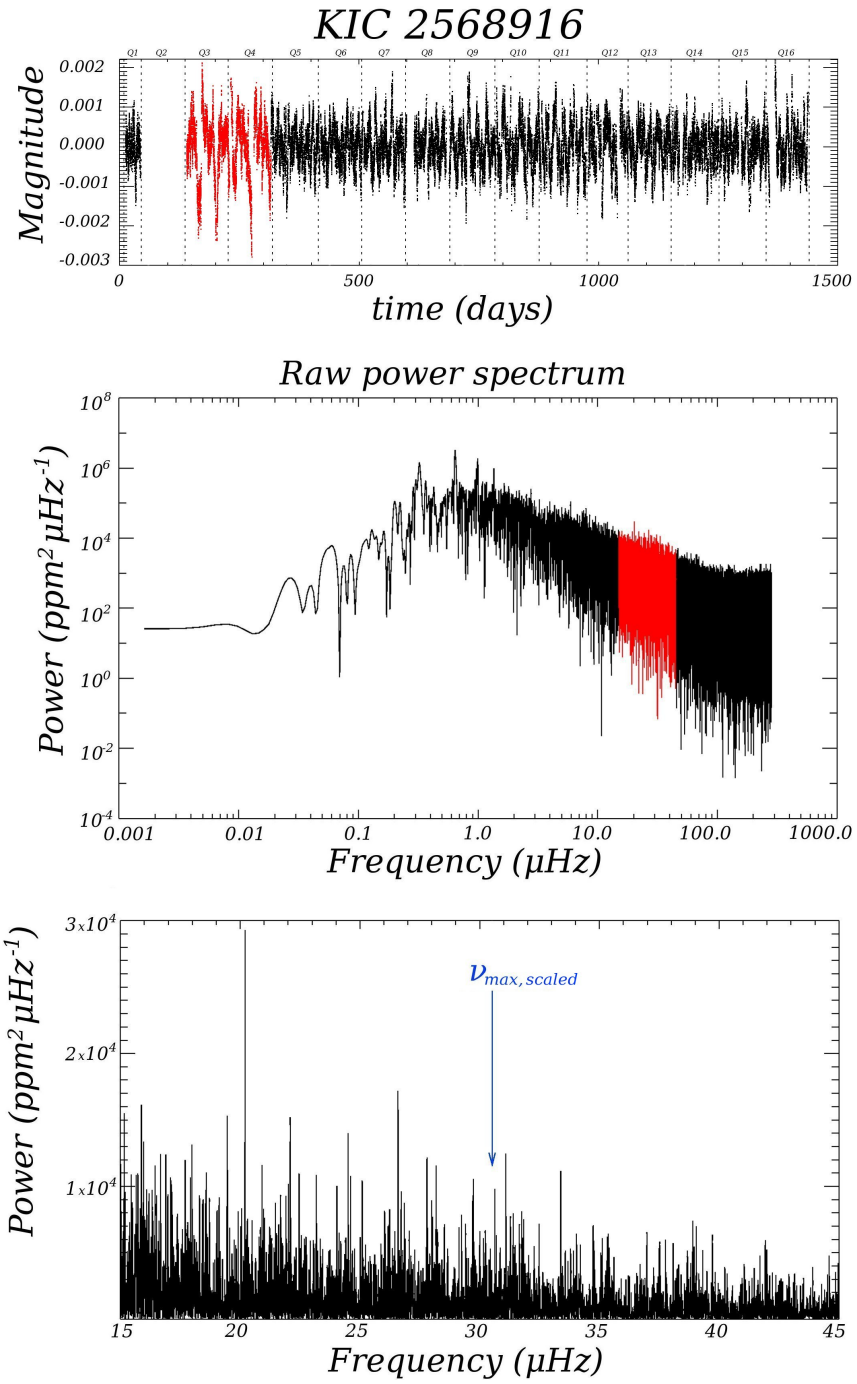

Figure 5.6: Top panel Shows the time series after alignment has been performed. The two quarters highlighted, Q3 and Q4 have been removed before further analysis. *Middle panel* indicates the power spectrum of the 13 quarters of the time series, with the highlighted region indicating where $\nu_{\rm max,scaled}$ is expected to be located. The extent of the highlighted region is defined by $\nu_{\rm max,scaled}$ $\pm 4\Delta\nu$. *Bottom panel* shows a zoomed in linear plot of the highlighted region in the middle panel with the $\nu_{\rm max,scaled}$ labeled.

5.8 and 5.9 show the distribution of all analysed red giant stars around each cluster, where the red dots indicate the likely members of Stello et al. (2011b) confirmed by this work. The blue squares

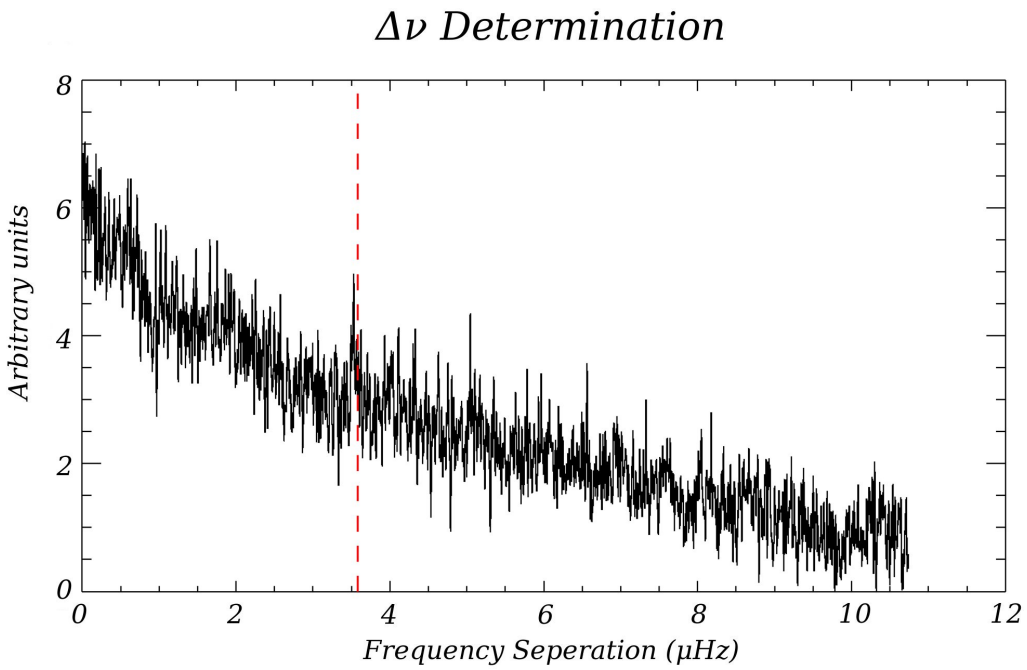

Figure 5.7: The autocorrelation function of the region highlighted in the middle panel of Figure 5.6. The red dashed line indicates the location of $\Delta\nu_{\ scaled}$. A peak similar to that found in Figure 5.4 is expected when there is a detected frequency separation.

indicate the position of the likely new members found by this work. The black circles are those stars that were deemed to be field stars. I can see that the red giants in these clusters are within 10' of the centre. This is in agreement with the cluster radii in the literature (Jensen, Boesgaard & Deliyannis 2006; Milliman et al. 2014; Anthony-Twarog, Deliyannis & Twarog 2014).

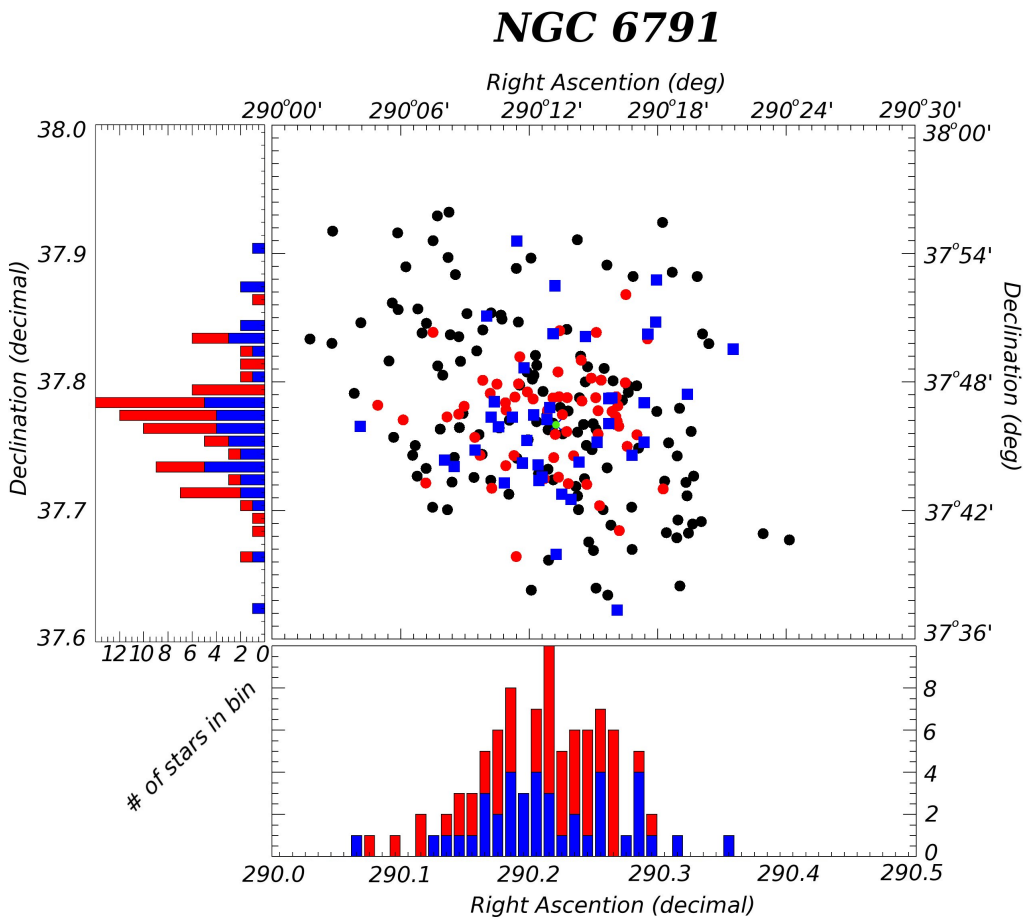

Figure 5.8: The main panel shows all stars analysed in this thesis for NGC 6791 as they would appear in the sky. The black dots indicate those stars that are considered field stars. The red dots are the stars considered members by Stello et al. (2011b) and confirmed by this work. The blue squares indicate all new asteroseismic members found by this work, the single green dot indicates the centre of the cluster. Histograms below and to the left are shown to represent the cluster distribution along each axis, and where the new members were found. It can be seen that the center of the cluster contains a higher density of red giants than the edges.

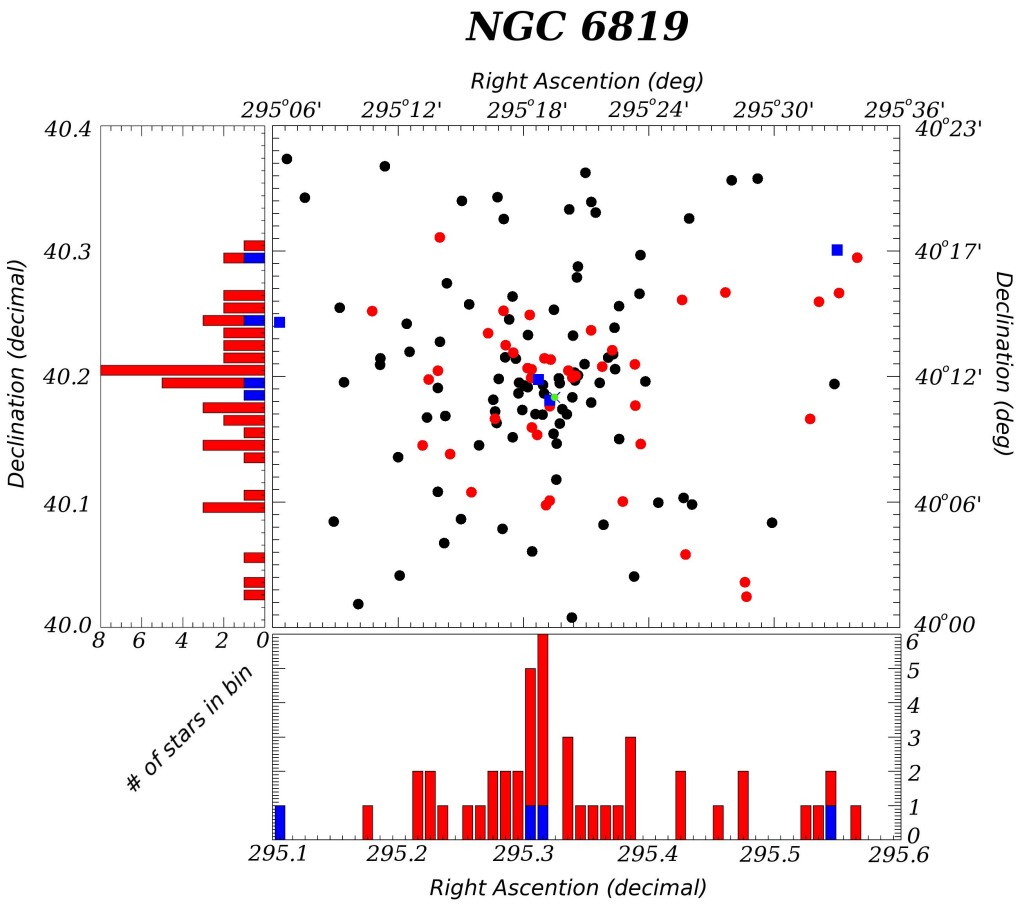

Figure 5.9: The main panel shows all stars analysed in this thesis for NGC 6819 as they would appear in the sky. The black dots indicate those stars that are considered field stars. The red dots are the stars considered members by Stello et al. (2011b) and confirmed by this work. The blue squares indicate all new asteroseismic members found by this work, the single green dot indicates the centre of the cluster. Histograms below and to the left are shown to represent the cluster distribution along each axis, and where the new members were found. It can be seen that the center of the cluster contains a higher density of red giants than the edges.

Chapter 6

Conclusion and Future Work

6.1 Conclusion

In this thesis, I performed an analysis of 438 stars in the *Kepler* field of view. The analysis was aimed at characterising their membership association with one of two clusters, NGC 6791 or NGC 6819. The photometric data required some smoothing and correction from jumps (see Chapter 4) in order to perform effective analysis. With more than four times the data available, with respect to Stello et al. (2011b), I was able to detect solar-like oscillations in more red giant stars than previous studies. The main achievements and conclusions of this thesis are:

- I was able to develop an interactive program described in Chapter 4 to process the *Kepler* photometric time series. As explained in Section 4.2, the photometric data show jumps in the average flux level which required correction. The interactive program can align each quarter to produce a relatively continuous time series. Three methods of alignment were implemented and the results of each displayed for user selection of the best alignment. In addition, the program also allowed for several processing options to be performed before or after the alignment process. The interactive nature of the program allowed me to maximise the number of stars I would be able to analyse by providing individually aligned time series tailored to each star.

- The modifications I made to the SYD pipeline code improve the effectiveness of the analysis for red giant stars. This is achieved by providing a frequency bounds toi estimate where the noise is dominated by granulation (end of granulation), and a frequency where the noise is dominated by white noise. These modifications allowed me to analyse multiple signals of excess power individually, avoiding any interference from blended signals. Modification of the frequency bounds for each individual star also allowed for optimisation of the background correction, to increase the likelihood of detecting solar-like oscillations.

- With the improvements made to the SYD pipeline code, I was able to extract a $\nu_{\rm max}$ value for 80% and a $\Delta\nu$ value for 73% of stars. This allowed membership determination of 87% of stars in the sample, with the remaining stars having no detection of $\nu_{\rm max}$ or $\Delta\nu$. A comparison with a previous study (Stello et al. 2011b) was performed to validate my sample, and I was able to confirm membership association for all targets listed in Stello et al. (2011b), except for KIC 2568916 which is discussed in detail in Section 5.4. The detection of solar-like oscillations in 87% of stars led to the discovery of 41 new red giant members in NGC 6791 and four new red giant members in NGC 6819 (see Chapter 5).

- Stello et al. (2011b) classified KIC 2568916 as a likely member of NGC 6791 based on manual measurements of a single quarter. With 13 times more data, p mode oscillations would be easier to detect due to reduced noise and better frequency resolution. However, an ACF of the uncorrected power spectrum showed no significant peak that would indicate membership. The background noise level was comparable to similar stars that were identified as cluster members and suggests that KIC 2568916 is not a member of NGC 6791.

6.2 Future Work

In order to make improvements on the research presented in this thesis, enhancements can be made to the tools that were used. While the interactive program developed as part of this research performed admirably by processing over 400 photometric light curves, it was not able to correct all discontinuities. Further effort could be spent on developing dedicated algorithms to remove each feature effectively. The safe modes could be removed by using polynomial corrections to the section of data affected tied to the general trend of the remaining data. The attitude tweaks could be corrected by using a similar procedure to stitch the quarters together, applied to the small jumps, similar to that described in García et al. (2011). Making these improvements would provide smoother discontinuities, resulting in less noise in the light curve. This would translate into a lower threshold for detecting solar-like oscillations.

The interactive program could also be modified to perform the independent processing on each individual quarter, such as detrending and high pass filtering. By applying this modification, each quarter could be adjusted independently improving the effectiveness of the data in the final analysis. This, however would require some knowledge of the whole light curve to decide on the correct processing choices for each quarter, as the initial choices will likely influence the choices made for successive quarters. However, it is likely that the differences between processing choices for consecutive quarters would be minor, such as a cutoff frequency for high pass filtering changing from 1μHz to 1.5 μHz .

I have shown that the detection of solar-like oscillations in red giant stars allows us to evaluate membership within a specific cluster, which can be used to constrain stellar evolution theories. The oscillation frequencies detected can also be used to investigate stellar structure in detail, such as the core composition (Montalbán et al. 2013; Stello et al. 2013) and the effect of mass loss (Barbaro & Pigatto 1984; Castellani & Castellani 1993). In addition to stellar evolution, red giants can be used as tracers for galactic populations Miglio et al. (2013) and as distance indicators (Wu, Li & Hekker 2014) when combined with photometric constraints. This has the potential to map the galaxy out to further distances than has previously been achieved, by up to a factor of ten (Miglio et al. 2013). Since stellar mass is a reliable proxy for age (Miglio et al. 2013), the oscillation frequencies can be used to constrain the mass and thus infer a stellar age.

Appendix A

Asteroseismic properties of NGC 6791

Table A.1: Asteroseismic properties of NGC 6791.

Target ID [1] KIC	Target ID (Stetson)[2]	$\nu_{\rm max}$ (μHz)	Solar Scaled $\nu_{\rm max}$ ratio[3]	$\Delta\nu$ (μHz)	Solar Scaled $\Delta\nu$ ratio[3]	Membership (Platais)[4] %	Seismic Membership (Stello) [5]	This work
2296995	1709	103.8 ± 1.15	1.02 ± 0.02	9.28 ± 0.04	1.01 ± 0.05		-	Yes
2297384	5583	30.41 ± 1.3	0.97 ± 0.08	3.78 ± 0.04	1.01 ± 0.1	93	Yes	Yes
2297454	6518	0.85 ± 0.12	0 ± 0	0.45 ± 0.05	0.03 ± 0		-	No
2297529	7624	4.08 ± 0.09	2.21 ± 0.22	0.74 ± 0.01	1.71 ± 0.07		-	No
2297574	8144	199.7 ± 0.02	0.93 ± 0	15.09 ± 0.03	0.93 ± 0.05	98	-	Yes
2297706	10259	14.68 ± -	0.06 ± -	6.69 ± 0.05	0.36 ± 0.02		-	No
2297721	10550	1.01 ± 0.01	0 ± 0	0.53 ± 0.04	0.01 ± 0		-	No
2297729	10689	1.52 ± -	0.01 ± -	0.09 ± -	0.01 ± 0		-	No
2297779	11371	4.23 ± 1.02	0.01 ± 0	0.52 ± 0.02	0.02 ± 0		-	No
2297793	11539	4.11 ± 0.18	0.38 ± 0.01	0.79 ± 0.01	0.49 ± 0.02	0	No	No
2297815	11863	49.96 ± 1.11	1.26 ± 0.07	5.16 ± 0.01	1.14 ± 0.07		-	Yes
2297825	11957	31.23 ± 1.22	0.99 ± 0.08	3.81 ± 0.04	1.01 ± 0.06	94	Yes	Yes
2297868	12601	1.01 ± 1.39	0 ± 0	0.42 ± 0.03	0.01 ± 0		-	No
2298006	13957	1 ± 0.37	0 ± 0	0.94 ± 0.48	0.02 ± 0		-	No
2298034	14198	26.31 ± 0.5	0.38 ± 0.01	3.18 ± 0.01	0.52 ± 0		-	No
2298039	14334	100.8 ± 0.72	1.87 ± 0.05	8.86 ± 0.02	1.59 ± 0.08		-	No
2298049	14395	- ± 7.81	- ± -	7.73 ± 0.07	0.18 ± 0.01		-	No
2298081	14672	0.76 ± 0.12	0 ± 0	0.25 ± 0.01	0 ± 0		-	No
2298097	14798	350.7 ± -	1.01 ± -	19.62 ± 0.04	0.83 ± 0.04	96	-	No
2298129	15058	- ± 1.7	- ± -	0.62 ± 0.04	0.02 ± 0		-	No
2298343	15881	64.38 ± 0.56	1.46 ± 0.04	6.16 ± 0.02	1.27 ± -		-	No
2298439	16094	9.3 ± 0.34	0.29 ± 0.01	1.36 ± 0.03	0.36 ± -		-	No
2435893	209	3.08 ± 0.14	0.07 ± 0	0.37 ± 0.07	0.08 ± 0		-	No
2435912[6]	366	- ± 52.87	- ± -	11.87 ± 0.08	1.06 ± 0.06		-	Yes
2435987	611	37.81 ± 0.76	1.1 ± 0.05	4.2 ± 0.01	1.06 ± 0.05	94	Yes	Yes
2436062	887	2.86 ± 0.06	0 ± 0	0.62 ± 0.05	0.01 ± 0		-	No
2436097	1110	42.39 ± 0.77	1.08 ± 0.04	4.52 ± 0.01	1.03 ± 0.05	96	Yes	Yes
2436136	1352	- ± 30.64	- ± -	5.46 ± 0.04	0.1 ± 0		-	No
2436148	1405	13.26 ± 9.91	0.03 ± 0	2.45 ± 0.03	0.08 ± 0		-	No
2436160	1459	1.32 ± 1.17	0 ± 0	0.52 ± 0.06	0.02 ± 0		-	No
2436209	1705	57.1 ± 0.66	1.07 ± 0.03	5.74 ± 0.02	1.02 ± 0.05	94	Yes	Yes
2436211	1714	1.76 ± 5.62	0 ± 0	1.09 ± 0.05	0.03 ± 0		-	No
2436291	2109	367.1 ± 0.95	1.04 ± 0.01	18.68 ± 0.01	0.78 ± 0.04	99	-	No
2436324	2170	124.8 ± 16.73	0.44 ± 0.05	15.62 ± 0.02	0.81 ± 0.09		-	Yes

[1]Only targets for which oscillations were detected are listed

[2]ID's from Stetson, Bruntt & Grundahl (2003)

[3]A value of 0 is less than 0.0001, effectively 0

[4]Membership probability from radial velocity (Platais et al. 2011)

[5]Seismic membership from Stello et al. (2011b)

[6]Cluster membership is based solely on the $\Delta\nu$ measurement.

2436332	2309	28.5 ± 0.79	0.99 ± 0.05	3.39 ± 0.01	0.98 ± 0.05	99	Yes	Yes
2436334	2320	62.18 ± 0.84	0.08 ± 0	6.04 ± 0.02	0.15 ± 0.01		-	No
2436365	2481	23.29 ± 7.27	0.14 ± 0.01	4.37 ± 0.01	0.32 ± 0.01		-	No
2436376	2544	175.8 ± 36.08	0.92 ± 0.36	13.53 ± 0.26	0.9 ± 0.05	98	-	Yes
2436417	2723	26.85 ± 0.61	1 ± 0.05	3.45 ± 0.03	1.03 ± 0.06	99	Yes	Yes
2436421	2746	8.05 ± 0.01	0 ± 0	1.24 ± 0	0 ± 0		-	No
2436448	2883	21.89 ± 0.67	0.1 ± 0	2.8 ± 0.33	0.17 ± 0.01		-	No
2436458	2915	37.57 ± 0.6	1 ± 0.03	4.16 ± 0.01	0.97 ± 0.06	99	Yes	Yes
2436533	3321	0.73 ± 0.02	0 ± 0	0.23 ± 0.04	0.01 ± 0		-	No
2436540	3354	57.5 ± 1.09	1.07 ± 0.04	5.8 ± 0.01	1.04 ± 0.06	85	Yes	Yes
2436543	3369	26.25 ± 0.84	0.85 ± 0.05	3.5 ± 0.03	0.94 ± 0.06	99	-	Yes
2436583	3567	5.08 ± 7.72	0 ± 0	2.05 ± 0.06	0.02 ± 0		-	No
2436593	3609	111.3 ± 1.26	1.04 ± 0.02	9.66 ± 0.04	1.01 ± 0.06	99	Yes	Yes
2436608	3712	24.36 ± 0.63	0.59 ± 0.02	3.67 ± 0.07	0.79 ± 0.05		-	No
2436676	4122	132.2 ± 1.87	1 ± 0.03	11.29 ± 0.05	1.01 ± 0.06	99	Yes	Yes
2436680	4143	18.8 ± 0.58	0.21 ± 0	2.54 ± 0.01	0.31 ± 0.02		-	No
2436682	4162	28.95 ± 1.39	1.15 ± 0.13	3.69 ± 0.04	1.17 ± 0.07		-	Yes
2436688	4202	77 ± 1.02	1.04 ± 0.03	7.21 ± 0.01	1 ± 0.06	99	Yes	Yes
2436715	4327	193.1 ± 142.9	1.1 ± 5.37	12.96 ± 0	0.94 ± 0.05	0	-	Yes
2436732	4482	30.94 ± 0.85	1 ± 0.06	3.68 ± 0.02	0.99 ± 0.06	99	Yes	Yes
2436750	4571	30.51 ± 1.81	0.91 ± 0.1	3.77 ± 0.03	0.95 ± 0.06	0	-	Yes
2436759[7]	4616	197.1 ± 1.33	1.31 ± 0.02	14.8 ± 0.04	1.2 ± 0.07	0	Yes	Yes
2436804	4894	213.1 ± 0.01	0.89 ± 0	15.96 ± 0.05	0.9 ± 0.05	99	-	Yes
2436814	4952	24.31 ± 0.42	0.93 ± 0.03	3.12 ± 0.01	0.96 ± 0.06	0	Yes	Yes
2436818	4968	97.63 ± 1.78	1.03 ± 0.04	8.79 ± 0.03	1.02 ± 0.06	99	Yes	Yes
2436824	4994	34.01 ± 0.37	0.95 ± 0.02	3.85 ± 0.01	0.94 ± 0.06	99	Yes	Yes
2436842	5150	250 ± 0.08	0.71 ± 0	16.87 ± 0.15	0.71 ± 0.04	99	-	No
2436849	5178	9.02 ± 0.44	0.09 ± 0	1.39 ± 0.05	0.15 ± 0.01		-	No
2436884	5342	9.25 ± 0.2	1.05 ± 0.05	1.4 ± 0.02	1.01 ± 0.05	99	-	Yes
2436900	5454	35.91 ± 0.62	1.03 ± 0.04	4.05 ± 0.02	1 ± 0.06	99	Yes	Yes
2436912	5503	29.59 ± 0.72	0.95 ± 0.04	3.74 ± 0.03	1 ± 0.06	0	Yes	Yes
2436935	5639	0.92 ± 0.09	0.01 ± 0	0.67 ± 0.13	0.05 ± 0		-	No
2436944	5712	30.02 ± 0.83	1.01 ± 0.06	3.73 ± 0.03	1.04 ± 0.06	95	Yes	Yes
2436954	5787	205.1 ± 2.82	0.67 ± 0.01	15.95 ± 0.03	0.75 ± 0.04	81	No	No
2436981	5972	119.5 ± 1.45	1.06 ± 0.03	10.12 ± 0.04	1.02 ± 0.06	99	-	Yes
2437033	6258	284.9 ± 0.25	0.92 ± 0	19.32 ± 0	0.9 ± 0.05	99	-	Yes
2437040	6288	25.78 ± 0.47	1.04 ± 0.04	3.08 ± 0.01	0.99 ± 0.06	99	Yes	Yes
2437103	6626	28.76 ± 1.19	0.91 ± 0.07	3.78 ± 0.03	1.01 ± 0.06	0	Yes	Yes
2437112	6667	261.3 ± 0.1	0.92 ± 0	17.58 ± 0.01	0.88 ± 0.05	90	-	Yes
2437164	6940	29.47 ± 1.18	0.9 ± 0.07	3.79 ± 0.04	0.97 ± 0.06	0	-	Yes
2437171	6963	0.92 ± 0.15	0.93 ± 0.3	0.21 ± 0.01	0.81 ± 0.01	99	Unknown	Unknown
2437178[8]	7006	- ± 0.01	- ± -	16.69 ± 0.08	0.99 ± 0.06	99	-	Yes
2437209	7186	283.9 ± 0	1.15 ± 0	17.13 ± 0.06	0.96 ± 0.06	99	-	Yes
2437222	7262	1.14 ± 0.05	0.01 ± 0	0.29 ± 0.01	0.02 ± 0		-	No
2437240	7347	45.78 ± 0.81	1.04 ± 0.04	4.84 ± 0.01	1.01 ± 0.06	99	Yes	Yes
2437261	7503	283.1 ± 20.07	0.91 ± 0.12	19.84 ± 0.1	0.92 ± 0.05	99	-	Yes
2437267	7540	36.34 ± 0.83	1.48 ± 0.1	3.92 ± 0.04	1.24 ± 0.07		-	No
2437270	7564	69.62 ± 0.91	1.08 ± 0.03	6.51 ± 0.01	1 ± 0.06	99	Yes	Yes
2437280	7593	69.41 ± 7.23	0.2 ± 0.01	6.87 ± 0.09	0.29 ± 0.02		-	No
2437281	7592	1.2 ± 0.24	0.01 ± 0	0.3 ± 0	0.02 ± 0		-	No
2437296	7687	206.8 ± 95.28	0.99 ± 1.13	16.94 ± 0.02	1.07 ± 0.06	0	-	Yes
2437317	7878	0.31 ± 0.01	0.01 ± 0	0.21 ± 0.01	0.04 ± 0		-	No
2437325	7912	93.04 ± 0.9	1 ± 0.02	8.28 ± 0.01	0.97 ± 0.06	99	Yes	Yes
2437327	7852	52.97 ± 0.66	1.19 ± 0.04	5.88 ± 0.04	1.21 ± 0.07		-	No
2437340	7972	8.45 ± 0.18	1.03 ± 0.04	1.38 ± 0.01	1.05 ± 0.05	99	Yes	Yes
2437353	8082	31.14 ± 0.93	1.01 ± 0.06	3.82 ± 0.03	1.03 ± 0.06	99	Yes	Yes
2437394	8317	158.5 ± 3.15	0.93 ± 0.03	12.66 ± 0.07	0.93 ± 0.05	99	Yes	Yes
2437402	8351	46.41 ± 0.83	1.08 ± 0.04	4.81 ± 0.01	1.02 ± 0.06	99	Yes	Yes
2437413	8429	- ± 0.01	- ± -	18.22 ± 0.02	0.74 ± 0.04	99	-	No
2437443	8544	176.3 ± 16.65	1.02 ± 0.2	13.68 ± 0.05	1 ± 0.06	99	-	Yes
2437444	8563	19.07 ± 0.43	1.04 ± 0.05	2.47 ± 0.02	1.01 ± 0.05	0	Yes	Yes
2437488	8865	63.3 ± 0.87	1.08 ± 0.03	6.28 ± 0.02	1.05 ± 0.06	96	Yes	Yes
2437496	8904	4.42 ± 0.08	0.99 ± 0.03	0.82 ± 0.06	0.99 ± 0.04	99	Yes	Yes

[7] Asteroseismic properties were manually measured

[8] Cluster membership is based solely on the $\Delta\nu$ measurement.

2437505	9413	0.54 ± 0.01	0 ± 0	0.13 ± 0.02	0 ± 0		-	No
2437507	8988	20.47 ± 0.41	0.99 ± 0.04	2.6 ± 0.01	0.96 ± 0.05	99	Yes	Yes
2437539	9157	47.22 ± 0.57	1.14 ± 0.03	4.9 ± 0.01	1.06 ± 0.06		-	Yes
2437564	9316	32.32 ± 0.87	1.03 ± 0.06	3.79 ± 0.04	1.01 ± 0.06	99	Yes	Yes
2437589	9462	46.5 ± 0.86	1.43 ± 0.08	4.61 ± 0.02	1.19 ± 0.07	99	Yes	Yes
2437610	9558	32.16 ± 25.62	0.08 ± 0.01	5.12 ± 0.06	0.19 ± 0.01		-	No
2437612	9562	44.74 ± 5.63	0.06 ± 0	4.93 ± 0.15	0.11 ± 0		-	No
2437622	9621	11.14 ± 0.12	0.12 ± 0	1.66 ± 0.01	0.19 ± 0.01		-	No
2437624[9]	9648	$- \pm 0.01$	$- \pm -$	18.44 ± 0.02	0.93 ± 0.05	99	-	Yes
2437630	9683	$- \pm 0.01$	$- \pm -$	12.93 ± 0.02	0.75 ± 0.04	99	-	No
2437653	9827	73.63 ± 0.68	1.05 ± 0.02	7.01 ± 0.02	1.02 ± 0.06	99	Yes	Yes
2437676	9926	$- \pm 23.46$	$- \pm -$	17.19 ± 0.2	0.7 ± 0.04	99	-	No
2437684	9991	0.93 ± 0.21	0.01 ± 0	0.12 ± 0.15	0.01 ± 0		-	No
2437694	10114	$- \pm 25.69$	$- \pm -$	18.02 ± 0.54	0.81 ± 0.05	99	-	No
2437698	10135	29.58 ± 1.71	0.97 ± 0.11	3.76 ± 0.02	1.02 ± 0.06	99	Yes	Yes
2437749	10461	26.5 ± 0.03	0.09 ± 0	4.14 ± 0.02	0.2 ± 0.01		-	No
2437762	10523	2.73 ± 0.01	0 ± 0	0.54 ± 0	0 ± 0		-	No
2437781	10674	85.07 ± 0.85	1.04 ± 0.02	7.82 ± 0.02	1.01 ± 0.06	0	Yes	Yes
2437783	11130	1.49 ± 0.01	0 ± 0	0.37 ± 0.02	0 ± 0		-	No
2437792	10755	324.1 ± 225.6	0.95 ± 2.25	19.94 ± 0.03	0.87 ± 0.05	82	-	Yes
2437804	10809	26.95 ± 1.09	1.02 ± 0.08	3.37 ± 0.05	1.03 ± 0.06	99	Yes	Yes
2437805	10806	32.37 ± 0.97	1.12 ± 0.07	3.75 ± 0.04	1.06 ± 0.06	99	Yes	Yes
2437816	10898	17.65 ± 0.33	0.99 ± 0.04	2.34 ± 0.02	0.97 ± 0.05	97	Yes	Yes
2437851	11116	$- \pm 0.07$	$- \pm -$	13.36 ± 0.01	0.8 ± 0.04	87	Unknown	No
2437888	11335	1.11 ± 0.02	0 ± 0	0.39 ± 0.02	0.01 ± 0		-	No
2437897	11404	149.8 ± 2.35	0.98 ± 0.03	12.21 ± 0.1	0.97 ± 0.06	99	-	Yes
2437901	11437	31.79 ± 0.68	1 ± 0.04	3.87 ± 0.04	1.02 ± 0.06		-	Yes
2437930	11585	148.1 ± 3.15	1 ± 0.04	12.19 ± 0.06	1 ± 0.06	99	-	Yes
2437933	11598	107.4 ± 0.96	0.99 ± 0.02	9.37 ± 0.02	0.97 ± 0.06	99	Yes	Yes
2437948	11722	5.95 ± 0.01	0.02 ± 0	0.84 ± 0.01	0.04 ± 0		-	No
2437957	11797	93.38 ± 1	0.98 ± 0.02	8.53 ± 0.01	0.98 ± 0.06	90	Yes	Yes
2437965	11814	6.99 ± 0.17	0.88 ± 0.04	1.33 ± 0.08	1.03 ± 0.05	99	Yes	Yes
2437972	11862	84.58 ± 0.75	1.07 ± 0.02	7.88 ± 0.03	1.05 ± 0.06	99	Yes	Yes
2437976	11895	88.78 ± 0.79	1.05 ± 0.02	8.13 ± 0.02	1.03 ± 0.06	99	Yes	Yes
2437987	11938	29.65 ± 1.16	0.95 ± 0.07	3.73 ± 0.03	1 ± 0.06	99	Yes	Yes
2438010	12111	0.93 ± 0.04	0.01 ± 0	0.21 ± 0.02	0.01 ± 0		-	No
2438038	12249	62.27 ± 0.57	1.06 ± 0.02	6.15 ± 0.02	1.03 ± 0.06	99	Yes	Yes
2438051	12333	30.23 ± 0.86	0.98 ± 0.05	3.62 ± 0.11	0.97 ± 0.06	99	Yes	Yes
2438094	12569	10.18 ± 0.46	0.15 ± 0	1.58 ± 0.02	0.24 ± 0.01		-	No
2438100	12596	69.62 ± 1.59	1.41 ± 0.09	6.08 ± 0.02	1.12 ± 0.06		-	Yes
2438139	12825	31.79 ± 1.05	1.79 ± 0.21	3.97 ± 0.04	1.62 ± 0.09		-	No
2438140	12836	70.24 ± 0.84	0.99 ± 0.02	6.74 ± 0.01	0.97 ± 0.06	0	Yes	Yes
2438191	13129	93.08 ± 0.99	1.03 ± 0.02	8.42 ± 0.03	1 ± 0.06		-	Yes
2438192	13133	286.8 ± 35.5	1.09 ± 0.3	19.27 ± 0.01	1.01 ± 0.06	99	-	Yes
2438289	13648	14.9 ± 0.42	0.43 ± 0.01	2.21 ± 0.01	0.55 ± 0.03		-	No
2438333	13847	60.81 ± 0.62	1.02 ± 0.02	6.09 ± 0.02	1 ± 0.05	98	Yes	Yes
2438340	13898	39.44 ± 12.47	0.16 ± 0.02	4.43 ± 0.02	0.25 ± 0.01		-	No
2438362	14021	45.29 ± 14.22	0.23 ± 0.03	6.99 ± 0.05	0.46 ± 0.03		-	No
2438421	14379	0.67 ± 0.01	0.75 ± 0.02	0.19 ± 0.01	0.79 ± 0.01	99	Unknown	No
2438462	14591	22.55 ± 1.02	0.6 ± 0.03	3.43 ± 0.04	0.81 ± 0.04		-	No
2438469	14627	0.94 ± 0.2	0 ± 0	0.22 ± 0.04	0.01 ± 0		-	No
2438470	14634	65.37 ± 0.81	1.05 ± 0.03	6.46 ± 0.03	1.02 ± 0.05		-	Yes
2568575	7	32.94 ± 0.59	2.13 ± 0.16	3.95 ± 0.02	1.78 ± 0.1		-	No
2568654	95	14.73 ± 0.56	1.65 ± 0.21	2.12 ± 0.01	1.47 ± 0.01		-	No
2568756	377	51.27 ± 0.83	0.34 ± 0	5.57 ± 0.01	0.45 ± 0.02		-	No
2568876	779	0.76 ± 0.2	0 ± 0	0.53 ± 0.04	0.01 ± 0		-	No
2568888	867	16.27 ± 0.28	1.54 ± 0.08	2.17 ± 0.02	1.37 ± 0.03		-	No
2568916[10]	996	24.59 ± 1	0.81 ± 0.05	3.05 ± 0.5	0.82 ± 0.03	83	Yes	No[11]
2569000	1605	0.87 ± 0.03	0 ± 0	0.25 ± 0.03	0.02 ± 0		-	No
2569055	1904	29.72 ± 1.25	1.01 ± 0.09	3.74 ± 0.04	1.05 ± 0.05	95	Yes	Yes
2569078	2044	23.41 ± 0.35	1.62 ± 0.08	2.91 ± 0.01	1.41 ± 0.06		-	No
2569105	2192	0.68 ± 0.02	0.01 ± 0	0.21 ± 0.01	0.02 ± 0		-	No

[9] Cluster membership is based solely on the $\Delta\nu$ measurement.

[10] Asteroseismic properties were manually measured

[11] membership is subject to change given more detailed data

2569126	2349	0.63 ± 0.01	1.38 ± 0.08	0.16 ± 0.01	1.14 ± 0.01		-	No
2569137	2423	4.44 ± 0.54	0.31 ± 0.02	0.82 ± 0.02	0.4 ± 0.02		-	No
2569171	2616	0.68 ± 0.02	0 ± 0	0.17 ± 0.04	0.01 ± 0		-	No
2569187	2729	14.84 ± -	0.06 ± -	1.56 ± 0.05	0.08 ± 0		-	No
2569204	2793	5.4 ± 0.3	1.23 ± 0.17	0.97 ± 0.03	1.21 ± 0.03		-	Unknown
2569310	3456	0.98 ± 0.06	0 ± 0	0.53 ± 0.01	0.03 ± 0		-	No
2569358	3755	73.54 ± 22.13	0.17 ± 0.02	6.55 ± 0.17	0.23 ± 0.01		-	No
2569360	3754	21.66 ± 0.35	0.97 ± 0.03	2.75 ± 0.01	0.96 ± 0.05	99	Yes	Yes
2569390	3951	62.41 ± 0.64	1.07 ± 0.02	6.28 ± 0.02	1.06 ± 0.05		-	Yes
2569426	4176	61.8 ± 0.65	1.25 ± 0.03	6.15 ± 0.02	1.15 ± 0.06		-	No
2569488	4715	29.41 ± 1.37	0.98 ± 0.09	3.28 ± 0.02	0.9 ± 0.04	98	Yes	Unknown
2569595	5597	10.91 ± -	0.05 ± -	2.22 ± 0.05	0.14 ± 0.01		-	No
2569605	5706	10.07 ± -	0.07 ± -	2.69 ± 0.04	0.23 ± 0.01		-	No
2569618	5796	56.29 ± 0.77	1.04 ± 0.03	5.66 ± 0.01	1 ± 0.06	99	Yes	Yes
2569650	6072	190.9 ± 2.1	1.03 ± 0.02	14.26 ± 0.06	0.98 ± 0.06	99	-	Yes
2569673	6275	- ± -	- ± -	19.83 ± 0.01	0.89 ± 0.05	99	-	No
2569702	6502	0.64 ± -	0 ± -	0.6 ± 0.11	0.01 ± 0		-	No
2569712	6583	210.45 ± 14.14	0.93 ± 0.12	9.17 ± 0.02	0.54 ± 0.03	99	-	Unknown
2569727	6679	0.52 ± 0.07	0 ± 0	0.41 ± 0.06	0.02 ± 0		-	No
2569737	6777	0.84 ± 0.01	0 ± 0	0.24 ± 0.02	0.01 ± 0		-	No
2569891	7922	29.73 ± 1.98	0.94 ± 0.12	3.53 ± 0.06	0.93 ± 0.05	99	-	Yes
2569912	8055	226.9 ± 9.5	0.94 ± 0.07	16.84 ± 0.02	0.95 ± 0.05	99	-	Yes
2569935	8266	5.18 ± 0.39	0.93 ± 0.13	0.98 ± 0.05	1 ± 0.05	96	Yes	Yes
2569945	8395	28.35 ± 0.81	0.89 ± 0.05	3.74 ± 0.05	0.98 ± 0.05	99	Yes	Yes
2569995	8867	0.61 ± 0.03	0 ± 0	0.18 ± 0.05	0 ± 0		-	No
2570092	9752	92.21 ± -	0.41 ± -	4.43 ± 0.03	0.26 ± 0.02		-	No
2570094	9786	67.99 ± 0.82	1.05 ± 0.03	6.5 ± 0.02	1.01 ± 0.06	98	Yes	Yes
2570131	10035	0.84 ± 0.14	0.01 ± 0	0.75 ± 0.02	0.06 ± 0		-	No
2570134[12]	10050	- ± 104.1	- ± -	18.7 ± 0.01	1 ± 0.05	99	-	Yes
2570172	10407	73.6 ± 0.39	1.05 ± 0.01	7.03 ± 0.01	1.02 ± 0.06	0	Yes	Yes
2570214	10695	25.89 ± 0.58	0.85 ± 0.03	3.6 ± 0.03	0.98 ± 0.05	99	Yes	Yes
2570244	11006	106.2 ± 0.9	1.07 ± 0.02	9.11 ± 0.03	1.02 ± 0.06	99	Yes	Yes
2570263	11164	399.9 ± 0.01	1.33 ± 0	17.58 ± 0.02	0.84 ± 0.05	99	-	No
2570384	12265	64.64 ± 1.18	1.07 ± 0.04	6.35 ± 0.02	1.04 ± 0.06	94	Yes	Yes
2570432	12650	12.34 ± 0.36	0.01 ± 0	2.03 ± 0.02	0.03 ± 0		-	No
2570518	13260	46.31 ± 0.65	1.02 ± 0.03	4.94 ± 0.01	1 ± 0.05	98	Yes	Yes
2570519	13277	172.7 ± 1.12	1.01 ± 0.01	13.37 ± 0.07	0.98 ± 0.03	99	-	Yes
2570575	13610	79.24 ± 1.02	1.01 ± 0.03	7.47 ± 0.02	0.99 ± 0.05		-	Yes
2570578	13632	31.43 ± 0.48	1.09 ± 0.04	3.59 ± 0.05	1.01 ± 0.06		-	Yes
2570652	14140	88.52 ± 0.96	1.49 ± 0.05	8.4 ± 0.02	1.35 ± 0.08		-	No
2570794	15080	10.86 ± 0.52	0.19 ± 0	1.66 ± 0.01	0.29 ± 0.01		-	No
2570825	15265	0.77 ± 0.04	0 ± 0	0.68 ± 0.02	0.02 ± 0		-	No
2570924	15615	50.55 ± 0.91	1.04 ± 0.04	5.36 ± 0.02	1.03 ± 0.06		-	Yes
2707109	102	0.78 ± 0.05	0.07 ± 0	0.27 ± 0.06	0.16 ± 0.01		-	No
2707312	988	0.4 ± 0.02	1.34 ± 0.16	0.12 ± 0.01	1.19 ± 0.01		-	No
2707427	1913	0.18 ± 0.01	0 ± 0	0.09 ± 0.02	0 ± 0		-	No
2707448	2039	91.01 ± 41.61	0.16 ± 0.02	5.41 ± 0.04	0.16 ± 0.01		-	No
2707478	2382	16.43 ± 0.39	1.53 ± 0.11	2.45 ± 0.02	1.47 ± 0.08		-	No
2707716	5630	29.95 ± 0.93	1.01 ± 0.06	3.75 ± 0.03	1.06 ± 0.06		-	Yes
2707916	9545	6.04 ± 2.27	0.03 ± 0	0.97 ± 0.03	0.06 ± 0		-	No
2708221	13818	12.23 ± 0.46	0.04 ± 0	2.67 ± 0.08	0.13 ± 0.01		-	No

[12]Cluster membership is based solely on the $\Delta\nu$ measurement.

Appendix B

Asteroseismic properties of NGC 6819

Table B.1: Asteroseismic properties of NGC 6819.

Target ID [1] KIC	Target ID (Hole)[2]	$\nu_{\rm max}$ (μHz)	Solar Scaled $\nu_{\rm max}$ ratio[3]	$\Delta\nu$ (μHz)	Solar Scaled $\Delta\nu$ ratio[3]	RV Membership (Hole)[4] %	(Platais)[5]	Seismic Membership (Stello) [6]	This work
4936244	30024	25.01 ± 19	0.01 ± 0	3.1 ± 0.01	0.02 ± 0	95	52	-	No
4936335	7021	7.43 ± 0.39	0.12 ± 0.01	1.41 ± 0.06	0.25 ± 0.01	95	31	No	No
4936404	31026	5.53 ± 0.05	0 ± 0	-3.14 ± 0.07	-0.01 ± 0	91	55	-	No
4936524	3022	255.1 ± 3.61	0 ± 0	18.24 ± -	0 ± 0	0	-	-	No
4936672	22018	2.74 ± 0.05	0 ± 0	0.5 ± 0.02	0 ± 0	SM	0	-	No
4936727	16015	2.04 ± 0.78	0 ± 0	0.51 ± 7.87	0 ± 0			-	No
4936741	-	2.96 ± -	0 ± 0	1.22 ± 0.2	0 ± 0	87	93	-	No
4936897	15015	0.81 ± 0.02	0 ± 0	0.31 ± 0.07	0 ± 0	92	99	-	No
4937011	7017	27.73 ± 0.79	0.44 ± 0.03	4.1 ± 0.04	0.69 ± 0.03			No	No
4937056	2012	45.6 ± 1.35	0.95 ± 0.05	4.77 ± 0.03	0.97 ± 0.04	0	-	Yes	Yes
4937149	-	1.08 ± 0.01	0 ± 0	0.26 ± 0.05	0 ± 0	95	0	-	No
4937257	9015	34.65 ± 0.61	0.35 ± 0.02	4.12 ± 0.05	0.49 ± 0.02	95	98	No	No
4937546	19020	96.1 ± 1.32	0.03 ± 0.01	7.9 ± 0.16	0.07 ± 0.01	88	81	-	No
4937576	5016	33.46 ± 0.77	1.01 ± 0.06	3.57 ± 0.01	0.98 ± 0.05	0	-	Yes	Yes
4937770	9024	63.85 ± 0.21	0.79 ± 0.04	7.85 ± -	1.07 ± 0.04	94	61	Yes	Unknown
4937775	9026	84.17 ± 10.49	0. 89 ± 0.03	7.3 ± 0.05	0.88 ± 0.03	0	0	Yes	No
4937861	12022	1.91 ± -	0 ± 0	0.83 ± 0.03	0.01 ± 0	95	73	-	No
5023548	20016	0.7 ± 0.02	0 ± 0	0.3 ± 0.04	0.01 ± 0	91	97	-	No
5023649	-	1.08 ± 0.02	0 ± 0	0.25 ± 0.02	0 ± 0	94	5	-	No
5023711	-	- ± 1.64	- ± -	2.08 ± 0.07	0.01 ± 0	91	16	-	No
5023712	-	0.92 ± 0.05	0 ± 0	0.44 ± 0.13	0 ± 0	0	-	-	No
5023732	5014	27.26 ± 0.51	0.97 ± 0.06	3.12 ± 0.01	0.96 ± 0.04	94	44	Yes	Yes
5023754	-	67.56 ± 21.9	0.01 ± 0	6.19 ± 0.14	0.02 ± 0	0	-	-	No
5023822	8012	1.14 ± 0.3	0 ± 0	0.29 ± -	0 ± 0			-	No
5023845	8010	109.5 ± 0.86	0.96 ± 0.05	8.9 ± 0.01	0.94 ± 0.04			Yes	Yes
5023849	13010	3.11 ± 0.76	0 ± 0	1.21 ± 0.07	0 ± 0			-	No
5023863	-	35.68 ± 18.53	0 ± 0	6.11 ± 0.04	0.02 ± 0	94	99	-	No
5023889	4014	53.57 ± 0.53	2.58 ± 0.15	5.37 ± 0.01	2.07 ± 0.09			No	No
5023890	9009	1.1 ± 0.03	0 ± 0	0.25 ± 0.08	0 ± 0			-	No
5023931	7009	50.63 ± 1.57	0.99 ± 0.06	4.92 ± 0.02	0.96 ± 0.04	92	99	Yes	Yes
5023953	3011	48.69 ± 1.23	1.19 ± 0.06	4.77 ± 0.01	1.1 ± 0.05	95	99	Yes	Yes
5024043	8013	55.89 ± 0.46	1.15 ± 0.06	5.59 ± 0.01	1.13 ± 0.05			Yes	Yes
5024084	16009	5.64 ± 0.02	0 ± 0	0.94 ± -	0 ± 0	95	0	-	No

[1]Only targets for which oscillations were detected are listed

[2]ID's from Hole et al. (2009)

[3]a value of 0 is less than 0.0001, effectively 0

[4]Membership probability from radial velocity (Hole et al. 2009); SM: single member; BM: binary member; BLM: binary likely member; BLN: binary likely non-member

[5]Membership probability from radial velocity Platais et al. (2011)

[6]Seismic membership from Stello et al. (2011b)

5024118	-	29.42 ± 0.06	0 ± 0	1.21 ± 0.02	0 ± 0	94	0	-	No
5024122	-	- ± 24.66	- ± -	4.7 ± 0.02	0.01 ± 0	84	99	-	No
5024143	7005	119.6 ± 2.46	0.97 ± 0.05	9.63 ± 0.02	0.96 ± 0.04			Yes	Yes
5024149	23006	2.25 ± 0.03	0.01 ± 0	0.52 ± 0.05	0.02 ± 0	BLM	99	-	No
5024150	11006	2.41 ± 0.04	0 ± 0	0.21 ± 0.88	0 ± 0	95	0	-	No
5024157	17006	2.59 ± 0.04	0 ± 0	0.82 ± 0.06	0 ± 0	BLM	99	-	No
5024173	9004	3.5 ± 0.04	0 ± 0	0.39 ± 0.07	0 ± 0			-	No
5024239	-	1.73 ± 0.02	0 ± 0	0.48 ± 0.41	0 ± 0			-	No
5024240	8007	153.7 ± 110.92	0.86 ± 0.04	11.95 ± 0.02	0.89 ± 0.03	94	0	Yes	No
5024268	2003	25.32 ± 0.04	1.71 ± 0.08	0.22 ± 3.65	0.11 ± 0	93	99	No	No
5024272	3003	17.86 ± 0.95	1.88 ± 0.11	1.99 ± 0.02	1.39 ± 0.06	94	99	No	No
5024287	10004	1.62 ± 0.03	0 ± 0	0.49 ± 0.09	0 ± 0	80	0	-	No
5024297	8003	46.34 ± 0.41	0.99 ± 0.06	4.57 ± 0.01	0.96 ± 0.04			Yes	Yes
5024312	13002	94.97 ± 1.26	0.95 ± 0.05	8.09 ± 0.02	0.95 ± 0.04	88	6	Yes	Yes
5024327	11002	43.9 ± 0.84	0.93 ± 0.05	4.72 ± 0.03	0.98 ± 0.04	BU	-	Yes	Yes
5024329	15005	223.5 ± 63.9	0.97 ± 0.05	15.62 ± 0.08	0.98 ± 0.04	0	-	-	Yes
5024354	7004	31.39 ± 6.93	0.01 ± 0	1.73 ± 0.03	0.01 ± 0	93	0	-	No
5024372	19002	20.63 ± 0.2	0.01 ± 0	2.64 ± 0.02	0.03 ± 0	95	1	-	No
5024404	3004	47.48 ± 0.79	1 ± 0.06	4.78 ± 0.04	0.99 ± 0.04			Yes	Yes
5024405	4001	96.87 ± 1.18	0.95 ± 0.05	8.26 ± 0.01	0.96 ± 0.04	89	41	Yes	Yes
5024414	6002	76.89 ± 0.95	1.29 ± 0.05	6.45 ± 0.04	1.1 ± 0.03	89	0	Unknown	Unknown
5024454	9003	207.4 ± 0.6	0.82 ± 0.01	1.71 ± 31.24	0.09 ± 0	0	-	-	No
5024455	14012	27.17 ± 0.42	0 ± 0	3.24 ± -	0 ± 0	94	99	-	No
5024456	1002	3.79 ± 0.09	1.25 ± 0.04	0.7 ± 0.02	1.22 ± 0.03	95	0	Yes	No
5024476	1006	66.08 ± 1.82	1.46 ± 0.07	5.76 ± 0.03	1.21 ± 0.04	95	0	Unknown	No
5024497	13006	34.43 ± 3.16	0.01 ± 0	4.09 ± 0.64	0.02 ± 0	94	8	-	No
5024503	-	- ± 1.71	- ± -	0.38 ± 0.03	0 ± 0	93	99	-	No
5024512	3001	72.51 ± 1.74	0.89 ± 0.05	6.69 ± 0.01	0.92 ± 0.04	93	98	Yes	Yes
5024517	2001	50.94 ± 1.13	3.03 ± 0.11	4.92 ± 0.02	2.37 ± 0.07	95	99	Unknown	No
5024519	11005	4.41 ± -	0 ± 0	0.58 ± 0.76	0.01 ± 0	95	99	-	No
5024531	12003	1.97 ± 0.02	0 ± 0	0.27 ± 0.02	0 ± 0	Rapid	99	-	No
5024557	11004	2.68 ± 1.07	0.01 ± 0	0.99 ± 0.27	0.03 ± 0	88	99	-	No
5024582	9002	45.57 ± 1.02	0.96 ± 0.05	4.78 ± 0.04	0.98 ± 0.04	BLM	99	Yes	Yes
5024583	7003	38.08 ± 0.49	1.01 ± 0.06	3.9 ± 0.01	0.96 ± 0.04	92	99	Yes	Yes
5024601	4002	32.31 ± 1.25	0.98 ± 0.05	3.71 ± 0.01	1.01 ± 0.05	94	99	Yes	Yes
5024717	-	1.91 ± 0.03	0 ± 0	0.48 ± 0.02	0 ± 0	93	99	-	No
5024747	-	1.03 ± 0.14	0 ± 0	0.59 ± 0.04	0 ± 0	88	0	-	No
5024750	1004	13.54 ± 1.22	1.04 ± 0.06	1.78 ± 0.03	1 ± 0.05	91	99	Yes	Yes
5024851	2008	4.02 ± 0.12	1.19 ± 0.04	0.75 ± 0.02	1.21 ± 0.03	95	0	Yes	No
5024870	20013	- ± 169.84	- ± -	16.78 ± 0.19	0.91 ± 0.03	BM	73	-	Unknown
5024943	21007	1.06 ± 0.03	0 ± 0	0.26 ± 0.02	0 ± 0	BLM	99	-	No
5024961	-	0.71 ± 0.21	0 ± 0	0.23 ± 0.03	0 ± 0	95	95	-	No
5024967	6009	44.97 ± 1.15	0.96 ± 0.05	4.73 ± 0.03	0.99 ± 0.04	92	76	Yes	Yes
5024975	-	3.31 ± 1.04	0 ± 0	18.22 ± -	0.05 ± 0.01	88	99	-	No
5024984	13007	- ± 9.7	- ± -	13.03 ± 0.02	0.67 ± 0.02			-	No
5025113	-	51.72 ± 41.51	0.01 ± 0	6.24 ± 0.04	0.03 ± 0			-	No
5025152	67015	0.74 ± 0.04	0 ± 0	0.21 ± 0.01	0 ± 0	93	99	-	No
5025675	22020	- ± 1.69	- ± -	0.29 ± 0.03	0 ± 0	95	99	-	No
5025769	11021	3.16 ± 0.05	0 ± 0	0.65 ± 0.02	0 ± 0	95	91	-	No
5111525	19021	4.83 ± 0.96	0 ± 0	0.32 ± 0.31	0 ± 0			-	No
5111718	8018	134.2 ± 1.1	0.92 ± 0.04	10.53 ± 0.02	0.93 ± 0.03	92	98	Yes	Yes
5111849	17013	1.95 ± 0.04	0 ± 0	-0.31 ± 0.03	0 ± 0	0	-	-	No
5111889	-	44.24 ± 23.77	0 ± 0	3.48 ± 0.02	0 ± 0			-	No
5111938	-	1.36 ± 0.02	0 ± 0	0.25 ± 0.08	0 ± 0	BLN		-	No
5111940	5012	52.17 ± 0.86	0.93 ± 0.05	5.19 ± 0.01	0.95 ± 0.04	0	-	Yes	Yes
5111949	4011	47.86 ± 1.12	0.97 ± 0.05	4.81 ± 0.09	0.96 ± 0.04			Yes	Yes
5112012	-	0.63 ± 0.02	0 ± 0	0.64 ± 0.02	0 ± 0	0	-	-	No
5112064	19009	- ± 0.07	- ± -	0.38 ± 0.12	0 ± 0	0	-	-	No
5112072	9010	125.3 ± 0.84	0.91 ± 0.04	10.02 ± 0.02	0.92 ± 0.03	0	-	Yes	Yes
5112104	18013	2.12 ± 0.04	0 ± 0	0.36 ± 0.02	0 ± 0	82	99	-	No
5112123	-	- ± 38.37	- ± -	7.83 ± 0.04	0 ± 0	81	2	-	No
5112182	-	2.42 ± 0.02	0 ± 0	0.18 ± 0.03	0 ± 0	95	55	-	No
5112198	10010	7.21 ± 0.02	0 ± 0	1.82 ± 0.01	0.01 ± 0	0	-	-	No
5112232	-	1.06 ± 0.06	0 ± 0	0.23 ± 0.02	0 ± 0	95	99	-	No
5112288	2007	47.33 ± 1	0.99 ± 0.05	4.82 ± 0.02	0.99 ± 0.04	0	-	Yes	Yes
5112361	4008	68.39 ± 0.73	1.03 ± 0.05	6.18 ± 0.01	0.98 ± 0.04			Yes	Yes

5112368	16005	2.58 ± 0.12	0 ± 0	1.31 ± 0.41	0.01 ± 0	95	99	-	No
5112373	5005	43.96 ± 0.91	0.94 ± 0.05	4.65 ± 0.03	0.97 ± 0.04	88	0	Yes	Yes
5112387	3007	45.63 ± 0.98	0.95 ± 0.05	4.67 ± 0.04	0.95 ± 0.04	95	99	Yes	Yes
5112401	3009	37.03 ± 0.84	1 ± 0.05	4.05 ± 0.03	1.01 ± 0.04			Yes	Yes
5112403	5004	141.8 ± 1.97	0.9 ± 0.04	11.13 ± 0.02	0.92 ± 0.03			Yes	Yes
5112409	22004	1.82 ± 0.03	0 ± 0	0.41 ± 0.18	0.01 ± 0	94	98	-	No
5112413	-	45.33 ± 6.52	0 ± 0	4.67 ± 0.03	0 ± 0	93	99	-	No
5112467	6003	45.44 ± 0.68	0.98 ± 0.05	4.71 ± 0.06	0.99 ± 0.04	0	-	Yes	Yes
5112468	17005	11.88 ± 0.02	0 ± 0	1.11 ± 0.03	0.01 ± 0			-	No
5112481	1007	4.86 ± 0.11	1.11 ± 0.04	0.88 ± 0.01	1.16 ± 0.04	95	99	Yes	Unknown
5112491	10002	44.67 ± 0.79	0.99 ± 0.05	4.68 ± 0.03	1 ± 0.04	95	99	Yes	Yes
5112499	-	- ± 0.19	- ± -	5.71 ± 0.03	0.01 ± 0	95	99	-	No
5112558	11003	35.93 ± 0.44	0.23 ± 0.01	3.98 ± 0.02	0.33 ± 0.01	0	-	-	No
5112604	22007	82.2 ± 4.12	0.02 ± 0	6.57 ± 0.31	0.04 ± 0.01			-	No
5112705	17002	109.1 ± 0.4	0.01 ± 0	11.12 ± -	0.04 ± 0.01	94	96	-	No
5112730	4005	43.62 ± 0.95	1 ± 0.05	4.57 ± 0.02	1.01 ± 0.04			Yes	Yes
5112734	12002	40.42 ± 0.52	1.02 ± 0.06	4.14 ± 0.01	0.99 ± 0.05	5	-	Yes	Yes
5112741	3002	56.26 ± 31.63	1.75 ± 0.1	7.76 ± 0.03	2.14 ± 0.09	93	99	-	No
5112744	5011	44.29 ± 0.81	1 ± 0.06	4.42 ± 0.02	0.97 ± 0.04	91	0	Yes	Yes
5112749	15012	3.95 ± 0.59	0 ± 0	0.76 ± 0.04	0 ± 0	94	99	-	No
5112751	8002	84.73 ± 2.12	1.67 ± 0.08	6.16 ± 0.04	1.2 ± 0.05	95	98	Unknown	No
5112786	5003	7.37 ± 0.56	1.15 ± 0.05	1.15 ± 0.02	1.13 ± 0.04	95	99	Yes	No
5112816	12006	- ± 1.56	- ± -	0.33 ± 0.16	0 ± 0	95	0	-	No
5112817	-	3.81 ± 0.33	0 ± 0	1.47 ± 0.08	0 ± 0	91	0	-	No
5112861	-	4.03 ± 2.01	0 ± 0	0.71 ± 0.02	0 ± 0	90	0	-	No
5112880	2004	25.62 ± 0.53	1.21 ± 0.07	2.8 ± 0.01	1.08 ± 0.05			Yes	Yes
5112907	-	0.96 ± 0.15	0 ± 0	0.6 ± 0.04	0 ± 0	95	25	-	No
5112910	9005	2.35 ± 0.03	0 ± 0	0.59 ± 0.03	0 ± 0	91	0	-	No
5112932	5006	5.73 ± 1	0 ± 0	1.98 ± 0.08	0 ± 0	92	0	-	No
5112938	2006	45.27 ± 0.79	0.98 ± 0.05	4.82 ± 0.06	1.01 ± 0.04	95	97	Yes	Yes
5112948	5007	42.61 ± 0.65	1 ± 0.06	4.29 ± 0.01	0.97 ± 0.04			Yes	Yes
5112950	3005	41.9 ± 1.03	1.01 ± 0.06	4.32 ± 0.05	0.99 ± 0.04	95	0	Yes	Yes
5112958	-	41.47 ± 0.8	0.01 ± 0	4.36 ± 0.14	0.02 ± 0		99	-	No
5112974	4009	40.63 ± 0.68	1.09 ± 0.06	4.35 ± 0.02	1.08 ± 0.05	94	99	Yes	Yes
5113041	4007	37.31 ± 0.64	0.96 ± 0.06	3.98 ± 0.01	0.97 ± 0.04		-	Yes	Yes
5113047	-	24.88 ± 5.17	0 ± 0	4.42 ± 0.06	0 ± 0	86	99	-	No
5113061	1014	4.44 ± 0.2	1.15 ± 0.04	0.77 ± 0.07	1.12 ± 0.04	Rapid	99	Yes	No
5113261	22013	1.08 ± 0.02	0 ± 0	0.93 ± 0.07	0.02 ± 0	95	96	-	No
5113344	-	- ± 0.06	- ± -	0.04 ± 0.08	0 ± 0		99	-	No
5113441	12016	153.9 ± 1.18	0.94 ± 0.05	12.17 ± 0.04	0.98 ± 0.04	93	14	Yes	Yes
5113457	-	- ± 55.95	- ± -	9.06 ± 0.09	0.01 ± 0	94	99	-	No
5113733	21021	3 ± 0.29	0.01 ± 0	1.22 ± 0.07	0.05 ± 0	BM	98	-	No
5113793	27023	1.55 ± 1	0 ± 0	0.6 ± 0.3	0.02 ± 0			-	No
5113848	26026	- ± 2	- ± -	1.39 ± 0.07	0.01 ± 0	BU	-	-	No
5199121	24029	- ± 1.08	- ± -	0.4 ± 0.07	0 ± 0			-	No
5199464	32024	2.73 ± 0.04	0 ± 0	0.05 ± 0.11	0 ± 0			-	No
5199710	16019	3.86 ± 1.16	0 ± 0	0.48 ± 0.04	0 ± 0	95	99	-	No
5199843	18019	1.35 ± 0.02	0 ± 0	0.32 ± 0.11	0 ± 0	89	98	-	No
5199859	1016	0.85 ± 0.02	1.57 ± 0.01	0.2 ± 0.03	1.34 ± 0	93	98	Yes	No
5200088	14017	- ± 137.57	- ± -	15.48 ± 0.19	0.92 ± 0.03	95	99	-	Unknown
5200152	3021	46.43 ± 0.7	0.97 ± 0.05	4.79 ± 0.1	0.97 ± 0.04			Yes	Yes
5200172	11018	3.08 ± 0.02	0 ± 0	0.88 ± 1.16	0.01 ± 0	94	94	-	No
5200187	18017	6.93 ± 0.08	0 ± 0	1.06 ± 0.05	0.01 ± 0	94	98	-	No
5200544	13019	0.72 ± 0.04	0 ± 0	0.2 ± 0.02	0 ± 0			-	No
5200689	24024	5.71 ± 0.06	0 ± 0	0.55 ± 0.07	0 ± 0			-	No
5200787	15025	- ± 118.59	- ± -	18.84 ± -	0.76 ± 0.02	95	95	-	No
5201088	17025	32.18 ± 0.22	0.02 ± 0	2.47 ± 0.01	0.03 ± 0	95	99	-	No

Appendix C

Kepler GO Proposals and working group surveys

Table C.1: Data sourced from the following proposals

KASOC Proposal ID	Proposal Description
GO10008	Defining the Dependencies of Rotation for Old Cool Stars.
GO20013	Eclipsing Binaries in the Old Open Clusters NGC 6791
GO20044	Age-Sensitive Detatched Eclipsing Binaries in Open Star Clusters NGC 6791 and NGC 6819
GO20053	Dynomo Parameters in Young Suns: A Kepler Study of Differential Rotation and Active Region Decay Rates in NGC 6811 (1Gyr) and NGC 6819 (2.5 Gyr)
GO20056	Photometry of Variable Hot SubDwarf Stars in NGC 6791
GO30012	Eclipsing Binaries in the Old Open Cluster NGC 6791
Go30022	Stellar Evolution in NGC 6791
GO30037	Improved Ages From Eclipsing Binaries in Open Star Clusters NGC 6791 and NGC 6819
GO40028	Studying G-Mode Subdwarf B Pulsators in Open Clusters Using Kepler
GO40033	The APOGEE-Kepler Red Giant Project: A Treasury for Stellar Popullation and Stellar Physics Studies
GO40035	Spin Synchronization and Asteroseismology of the SDB DB Binary B4 in NGC 6791
GO40036	Precision Star Ages Using Detached Eclipsing Binaries in the Kepler Star Clusters
GO40043	Evolution of Critical Magnetic Cycle Parameters with Stellar Age: Differential Rotation and Active Region Decay Rates in Kepler Clusters NGC 6811 (1 Gyr) and 6819 (2.5 Gyr)
GO40064	Eclipsing Binaries and the Spatial Extent of the Old Cluster NGC 6791
P01_27	Solar-like Oscillations in Stars from the Open Clusters NGC 6811 and NGC 6866
P01_28	Asteroseismology on the bright young clusters NGC6811 and NGC6866
P01_29	Solar-like oscillations in the 2.5 Gyr cluster NGC6819
P01_32	Red giants in the metal-rich open cluster NGC6791
Q6_WG02	Oscillations in Clusters
Q7_WG02	Oscillations in Clusters
Q9_WG02	Oscillations in Clusters
Q11_WG02	Oscillations in Clusters
Q7_WG08	Red Giants
Q11_WG08	Red Giants

References

Aerts C., Christensen-Dalsgaard J., Cunha M. et al. The Current Status of Asteroseismology, 2008, Sol Phys, 251, 3

Aerts C., Christensen-Dalsgaard J., Kurtz D. W., 2010, Asteroseismology, Asteroseismology, Springer Dordrewcht Heidelberg London New York, pp. 1–866

Anthony-Twarog B. J., Deliyannis C. P., Twarog B. A. A uvbyCaHβ Analysis of the Old Open Cluster, NGC 6819, 2014, AJ, 148, 51

Appourchaux T., Michel E., Auvergne M. et al. CoRoT sounds the stars: p-mode parameters of Sun-like oscillations on HD 49933, 2008, A&A, 488, 705

Arentoft T., Kjeldsen H., Bedding T. R. et al. A Multisite Campaign to Measure Solar-like Oscillations in Procyon. I. Observations, Data Reduction, and Slow Variations, 2008, ApJ, 687, 1180

Barban C., Michel E., Martic M. et al. Solar-like oscillations of Procyon A: stellar models and time series simulations versus observations, 1999, A&A, 350, 617

Barbaro G., Pigatto L. Red giants in old open clusters - A test for stellar evolution, 1984, A&A, 136, 355

Barclay T., Burke C. J., Howell S. B. et al. A Super-Earth-sized Planet Orbiting in or Near the Habitable Zone around a Sun-like Star, 2013a, ApJ, 768, 101

Barclay T., Rowe J. F., Lissauer J. J. et al. A sub-Mercury-sized exoplanet, 2013b, Nature, 494, 452

Barge P., Baglin A., Auvergne M. et al. Transiting exoplanets from the CoRoT space mission. I. CoRoT-Exo-1b: a low-density short-period planet around a G0V star, 2008, A&A, 482, L17

Basu S., Grundahl F., Stello D. et al. Sounding Open Clusters: Asteroseismic Constraints from Kepler on the Properties of NGC 6791 and NGC 6819, 2011, ApJ, 729, L10

Bazot M., Ireland M. J., Huber D. et al. The radius and mass of the close solar twin 18 Scorpii derived from asteroseismology and interferometry, 2011, A&A, 526, L4

Beck P. G., Kambe E., Hillen M. et al. Detection of solar-like oscillations in the bright red giant stars γ Psc and θ^1 Tau from a 190-day high-precision spectroscopic multisite campaign, 2014, ArXiv e-prints

Bedding T. R. Solar-like Oscillations: An Observational Perspective, 2011, Arxiv e-print

Bedding T. R., Butler R. P., Kjeldsen H. et al. Evidence for Solar-like Oscillations in β Hydri, 2001, ApJ, 549, L105

Bedding T. R., Huber D., Stello D. et al. Solar-like Oscillations in Low-luminosity Red Giants: First Results from Kepler, 2010a, ApJ, 713, L176

Bedding T. R., Kjeldsen H. Solar-like Oscillations, 2003, PASA, 20, 203

Bedding T. R., Kjeldsen H. Scaled oscillation frequencies and échelle diagrams as a tool for comparative asteroseismology, 2010, Comm in Astero, 161, 3

Bedding T. R., Kjeldsen H., Arentoft T. et al. Solar-like Oscillations in the G2 Subgiant β Hydri from Dual-Site Observations, 2007, ApJ, 663, 1315

Bedding T. R., Kjeldsen H., Campante T. L. et al. A Multi-Site Campaign to Measure Solar-Like Oscillations in Procyon. II. Mode Frequencies, 2010b, ApJ, 713, 935

Bedding T. R., Kjeldsen H., Reetz J. et al. Measuring stellar oscillations using equivalent widths of absorption lines, 1996, MNRAS, 280, 1155

Bedding T. R., Mosser B., Huber D. et al. Gravity modes as a way to distinguish between hydrogen- and helium-burning red giant stars, 2011, Nature, 471, 608

Benomar O., Belkacem K., Bedding T. R. et al. Asteroseismology of Evolved Stars with Kepler: A New Way to Constrain Stellar Interiors Using Mode Inertias, 2014, ApJ, 781, L29

Bethe H. A. Energy Production in Stars, 1939, Physical Review, 55, 434

Boesgaard A. M., Jensen E. E. C., Deliyannis C. P. Abundances in Turnoff Stars in the Old, Metal-Rich Open Cluster, NGC 6791, 2009, AJ, 137, 4949

Borucki W. J., Koch D., Basri G. et al. Kepler Planet-Detection Mission: Introduction and First Results, 2010, Science, 327, 977

Borucki W. J., Koch D. G., Batalha N. et al. Kepler-22b: A 2.4 Earth-radius Planet in the Habitable Zone of a Sun-like Star, 2012, ApJ, 745, 120

Bouchy F., Bazot M., Santos N. C. et al. Asteroseismology of the planet-hosting star μ Arae. I. The acoustic spectrum, 2005, A&A, 440, 609

Bouchy F., Carrier F. P-mode observations on α Cen A, 2001, A&A, 374, L5

Bragaglia A., Carretta E., Gratton R. G. et al. Metal Abundances of Red Clump Stars in Open Clusters. I. NGC 6819, 2001, AJ, 121, 327

Brogaard K., Bruntt H., Grundahl F. et al. Age and helium content of the open cluster NGC 6791 from multiple eclipsing binary members. I. Measurements, methods, and first results, 2011, A&A, 525, A2

Brogaard K., VandenBerg D. A., Bruntt H. et al. Age and helium content of the open cluster NGC 6791 from multiple eclipsing binary members. II. Age dependencies and new insights, 2012, A&A, 543, A106

Broomhall A.-M., Miglio A., Montalbán J. et al. Prospects for asteroseismic inference on the envelope helium abundance in red giant stars, 2014, MNRAS, 440, 1828

Brown T. M., Gilliland R. L., Noyes R. W. et al. Detection of possible p-mode oscillations on Procyon, 1991, ApJ, 368, 599

Buzasi D., Catanzarite J., Laher R. et al. The Detection of Multimodal Oscillations on α Ursae Majoris, 2000, ApJ, 532, L133

Carraro G., Villanova S., Demarque P. et al. NGC 6791: An Exotic Open Cluster or the Nucleus of a Tidally Disrupted Galaxy?, 2006, ApJ, 643, 1151

Carrier F., Bouchy F., Meynet G. et al., 2002, in Astronomical Society of the Pacific Conference Series, Vol. 259, IAU Colloq. 185: Radial and Nonradial Pulsationsn as Probes of Stellar Physics, Aerts C., Bedding T. R., Christensen-Dalsgaard J., eds., P-Mode Observations on α Cen A with CORALIE, p. 460

Carrier F., De Ridder J., Baudin F. et al. Non-radial oscillations in the red giant HR 7349 measured by CoRoT, 2010, A&A, 509, A73

Carrier F., Kjeldsen H., Bedding T. R. et al. Solar-like oscillations in the metal-poor subgiant ν Indi. II. Acoustic spectrum and mode lifetime, 2007, A&A, 470, 1059

Casagrande L., Flynn C., Portinari L. et al. The helium abundance and ΔY/ΔZ in lower main-sequence stars, 2007, MNRAS, 382, 1516

Castellani M., Castellani V. Mass loss in globular cluster red giants - an evolutionary investigation, 1993, ApJ, 407, 649

Chaplin W. J., Appourchaux T., Arentoft T. et al. AsteroFLAG - from the Sun to the stars, 2008, Journal of Physics Conference Series, 118, 012048

Chaplin W. J., Kjeldsen H., Christensen-Dalsgaard J. et al. Ensemble Asteroseismology of Solar-Type Stars with the NASA Kepler Mission, 2011, Science, 332, 213

Christensen-Dalsgaard J., 2014, Asteroseismology, Asteroseismology of red giants, Springer, p. 194

Christensen-Dalsgaard J., Bedding T. R., Kjeldsen H. Modeling solar-like oscillations in eta Bootis, 1995, ApJ, 443, L29

Christiansen J., Van Cleve J., 2011, Kepler Data Characteristics Handbook, Kepler Data Characteristics Handbook, NASA Ames Research Centre

Corsaro E., Stello D., Huber D. et al. Asteroseismology of the Open Clusters NGC 6791, NGC 6811, and NGC 6819 from 19 Months of Kepler Photometry, 2012, ApJ, 757, 190

Cunha M. S., Metcalfe T. S. Asteroseismic Signatures of Small Convective Cores, 2007, ApJ, 666, 413

de Marchi F., Poretti E., Montalto M. et al. Variable stars in the open cluster NGC 6791 and its surrounding field, 2007, A&A, 471, 515

De Ridder J., Barban C., Baudin F. et al. Non-radial oscillation modes with long lifetimes in giant stars, 2009, Nature, 459, 398

De Ridder J., Barban C., Carrier F. et al. Discovery of solar-like oscillations in the red giant ε Ophiuchi, 2006, A&A, 448, 689

di Mauro M. P., Cardini D., Catanzaro G. et al. Solar-like oscillations from the depths of the red-giant star KIC 4351319 observed with Kepler, 2011, MNRAS, 415, 3783

Dick S. J., 1996, The Biological Universe, The Biological Universe, Cambridge, UK: Cambridge University Press, June 1996.

Dziembowski W. Light and radial velocity variations in a nonradially oscillating star, 1977, Actaa, 27, 203

Eddington A. S. Stars, Gaseous, On the pulsations of a gaseous star, 1918, MNRAS, 79, 2

Eddington A. S., 1926, The Internal Constitution of the Stars, The Internal Constitution of the Stars, Cambridge: Cambridge University Press, 1926

Edmonds P. D., Gilliland R. L. K Giants in 47 Tucanae: Detection of a New Class of Variable Stars, 1996, ApJ, 464, L157

Epstein C. R., Elsworth Y. P., Johnson J. A. et al. Testing the Asteroseismic Mass Scale Using Metal-poor Stars Characterized with APOGEE and Kepler, 2014, ApJ, 785, L28

Fletcher S. T., Chaplin W. J., Elsworth Y. et al., 2006, in ESA Special Publication, Vol. 624, Proceedings of SOHO 18/GONG 2006/HELAS I, Beyond the spherical Sun, Frequency, splitting, linewidth and amplitude estimates of low-l p modes of alpha Cen A: analysis of WIRE photometry

Flower P. J. Transformations from Theoretical Hertzsprung-Russell Diagrams to Color-Magnitude Diagrams: Effective Temperatures, B-V Colors, and Bolometric Corrections, 1996, ApJ, 469, 355

Foster B. O., 1854, The History of Rome, Book 21, The History of Rome, Book 21, Reimer & Hirsel

Frandsen S., Carrier F., Aerts C. et al. Detection of Solar-like oscillations in the G7 giant star xi Hya, 2002, A&A, 394, L5

Freeman K., Bland-Hawthorn J. The New Galaxy: Signatures of Its Formation, 2002, ARA&A, 40, 487

Frinchaboy P. M., Thompson B., Jackson K. M. et al. The Open Cluster Chemical Analysis and Mapping Survey: Local Galactic Metallicity Gradient with APOGEE Using SDSS DR10, 2013, ApJ, 777, L1

García R. A., Hekker S., Stello D. et al. Preparation of Kepler light curves for asteroseismic analyses, 2011, MNRAS, 414, L6

Gilliland R. L., Brown T. M., Christensen-Dalsgaard J. et al. Kepler Asteroseismology Program: Introduction and First Results, 2010, PASP, 122, 131

Gilliland R. L., Brown T. M., Kjeldsen H. et al. A search for solar-like oscillations in the stars of M67 with CCD ensemble photometry on a network of 4 M telescopes, 1993, AJ, 106, 2441

Gilliland R. L., McCullough P. R., Nelan E. P. et al. Asteroseismology of the Transiting Exoplanet Host HD 17156 with Hubble Space Telescope Fine Guidance Sensor, 2011, ApJ, 726, 2

Girardi L. A secondary clump of red giant stars: why and where, 1999, MNRAS, 308, 818

Girardi L., Groenewegen M. A. T., Weiss A. et al. Fine structure of the red giant clump from HIPPARCOS data, and distance determinations based on its mean magnitude, 1998, MNRAS, 301, 149

Gizis J. Simultaneous Spitzer and Kepler K2 Observa tions of a Bright, Nearby L8 dwarf, 2014, Spitzer Proposal, 10167

Gosnell N. M., Pooley D., Geller A. M. et al. An Unexpected Discovery in the Rich Open Cluster NGC 6819 Using XMM-Newton, 2012, ApJ, 745, 57

Gough D. O., 1993, in Astrophysical Fluid Dynamics - Les Houches 1987, Zahn J.-P., Zinn-Justin J., eds., Linear adiabatic stellar pulsation., Linear adiabatic stellar pulsation., pp. 399–560

Grec G., Fossat E., Pomerantz M. A. Full-disk observations of solar oscillations from the geographic South Pole - Latest results, 1983, Sol Phys, 82, 55

Grundahl F., Christensen-Dalsgaard J., Kjeldsen H. et al., 2009, in Astronomical Society of the Pacific Conference Series, Vol. 416, Solar-Stellar Dynamos as Revealed by Helio- and Asteroseismology: GONG 2008/SOHO 21, Dikpati M., Arentoft T., González Hernández I., Lindsey C., Hill F., eds., The Stellar Observations Network Group - the Prototype, p. 579

Hartman J. D., Stanek K. Z., Gaudi B. S. et al. Pushing the Limits of Ground-based Photometric Precision: Submillimagnitude Time-Series Photometry of the Open Cluster NGC 6791, 2005, AJ, 130, 2241

Hekker S., Arentoft T., Kjeldsen H. et al. Oscillations in Procyon A: First results from a multi-site campaign, 2008, Journal of Physics Conference Series, 118, 012059

Hekker S., Basu S., Stello D. et al. Asteroseismic inferences on red giants in open clusters NGC 6791, NGC 6819, and NGC 6811 using Kepler, 2011a, A&A, 530, A100

Hekker S., Elsworth Y., De Ridder J. et al. Solar-like oscillations in red giants observed with Kepler: comparison of global oscillation parameters from different methods, 2011b, A&A, 525, A131

Hekker S., Gilliland R. L., Elsworth Y. et al. Characterization of red giant stars in the public Kepler data, 2011c, MNRAS, 414, 2594

Hekker S., Kallinger T., Baudin F. et al. Characteristics of solar-like oscillations in red giants observed in the CoRoT exoplanet field, 2009, A&A, 506, 465

Hoaglin D. C., Mosteller F., Tukey J. W., 1983, Understanding robust and exploratory data anlysis, Understanding robust and exploratory data anlysis. John Wiley and Sons Inc

Hole K. T., Geller A. M., Mathieu R. D. et al. WIYN Open Cluster Study. XXIV. Stellar Radial-Velocity Measurements in NGC 6819, 2009, AJ, 138, 159

Huber D. Asteroseismology of Eclipsing Binary Stars in the Kepler Era, 2014, Arxiv e-prints

Huber D., Bedding T. R., Arentoft T. et al. Solar-like Oscillations and Activity in Procyon: A Comparison of the 2007 MOST and Ground-based Radial Velocity Campaigns, 2011a, ApJ, 731, 94

Huber D., Bedding T. R., Stello D. et al. Testing Scaling Relations for Solar-like Oscillations from the Main Sequence to Red Giants Using Kepler Data, 2011b, ApJ, 743, 143

Huber D., Bedding T. R., Stello D. et al. Asteroseismology of Red Giants from the First Four Months of Kepler Data: Global Oscillation Parameters for 800 Stars, 2010, ApJ, 723, 1607

Huber D., Stello D., Bedding T. R. et al. Automated extraction of oscillation parameters for Kepler observations of solar-type stars, 2009, Comm in Astero, 160, 74

Janes K. A. DDO and UBV photometry of red giant stars in NGC 6791, 1984, PASP, 96, 977

Jeffery C. S., Ramsay G. K2 observations of the pulsating subdwarf B star EQ Piscium: an sdB+dM binary, 2014, ArXiv e-prints

Jendreieck A., Weiss A., Silva Aguirre V. et al. Red giant oscillations: Stellar models and mode frequency calculations, 2012, Astronomische Nachrichten, 333, 939

Jenkins J. M., Caldwell D. A., Chandrasekaran H. et al. Overview of the Kepler Science Processing Pipeline, 2010, ApJ, 713, L87

Jensen E., Boesgaard A. M., Deliyannis C. P., 2006, in Bulletin of the American Astronomical Society, Vol. 38, American Astronomical Society Meeting Abstracts, The Composition of the Old, Metal-Rich Open Cluster, NGC 6791, p. 165

Kallinger T., Guenther D. B., Weiss W. W. et al. MOST found evidence for solar-type oscillations in the K2 giant star HD 20884, 2008, Comm in Astero, 153, 84

Kallinger T., Mosser B., Hekker S. et al. Asteroseismology of red giants from the first four months of Kepler data: Fundamental stellar parameters, 2010, A&A, 522, A1

Kallinger T., Zwintz K., Pamyatnykh A. A. et al. Pulsation of the K 2.5 giant star GSC 09137-03505?, 2005, A&A, 433, 267

Karoff C., 2008, Observational Asteroseismology. PhD thesis, Department of Physics and Astronomy

Karttunen H., Krüger P., Oja H., Poutanen M., Donner K. J., eds., 2007, Fundamental Astronomy, Fundamental Astronomy. Springer

Kawaler S. D., 2012, in American Astronomical Society Meeting Abstracts, Vol. 220, American Astronomical Society Meeting Abstracts 220, Studying the Evolution of Stars (and their Planets) beyond the Helium Core Flash via Kepler Asteroseismology, p. 419.04

Kippenhahn R., Weigert A., 1994, Stellar Structure and Evolution, XVI, 468 pp. 192, Stellar Structure and Evolution, Springer-Verlag Berlin Heidelberg New York. Also Astronomy and Astrophysics Library

Kjeldsen H., Bedding T. R. Amplitudes of stellar oscillations: the implications for asteroseismology., 1995, A&A, 293, 87

Kjeldsen H., Bedding T. R., Baldry I. K. et al. Confirmation of Solar-like Oscillations in η Bootis, 2003, AJ, 126, 1483

Kjeldsen H., Bedding T. R., Christensen-Dalsgaard J., 2008, in American Institute of Physics Conference Series, Vol. 1043, American Institute of Physics Conference Series, Mioc V., Dumitrche C., Popescu N. A., eds., Asteroseismology-Studying stellar structure, pp. 365–372

Kjeldsen H., Bedding T. R., Viskum M. et al. Solarlike oscillations in eta Boo, 1995, AJ, 109, 1313

Kuehn C. A., Drury J., Bellamy B. et al., 2015, in American Astronomical Society Meeting Abstracts, Vol. 225, American Astronomical Society Meeting Abstracts, Asteroseismology of Stars in NGC 6791 Using Kepler "Superstamps", p. 310.06

Lebreton Y., Goupil M. J. Asteroseismology for "à la carte" stellar age-dating and weighing. Age and mass of the CoRoT exoplanet host HD 52265, 2014, A&A, 569, A21

Lebreton Y., Montalbán J., 2009, in IAU Symposium, Vol. 258, IAU Symposium, Mamajek E. E., Soderblom D. R., Wyse R. F. G., eds., Stellar ages from asteroseismology, pp. 419–430

Lenz P., Breger M. Period04 User Guide, 2005, Comm in Astero, 146, 53

Lissauer J. J., Fabrycky D. C., Ford E. B. et al. A closely packed system of low-mass, low-density planets transiting Kepler-11, 2011, Nature, 470, 53

Marigo P., Girardi L., Bressan A. et al. Evolution of asymptotic giant branch stars. II. Optical to far-infrared isochrones with improved TP-AGB models, 2008, A&A, 482, 883

Martić M., Schmitt J., Lebrun J.-C. et al. Evidence for global pressure oscillations on Procyon, 1999, A&A, 351, 993

Mathur S., García R. A., Régulo C. et al., 2009, in American Institute of Physics Conference Series, Vol. 1170, American Institute of Physics Conference Series, Guzik J. A., Bradley P. A., eds., Analysing Solar-like Oscillations with an Automatic Pipeline, pp. 540–542

Mathur S., Garcia R. A., Regulo C. et al. An automatic pipeline analysing solar-like oscillating targets tested on CoRoT and simulated data, 2010, Arxiv e-printe-prints

Matthews J. M. One small satellite, so many light curves: Examples of δ Scuti asteroseismology from the MOST space mission^1, 2007, Comm in Astero, 150, 333

Mayor M., Queloz D. A Jupiter-mass companion to a solar-type star, 1995, Nature, 378, 355

Metcalfe T. S., 2009, in Astronomical Society of the Pacific Conference Series, Vol. 416, Solar-Stellar Dynamos as Revealed by Helio- and Asteroseismology: GONG 2008/SOHO 21, Dikpati M., Arentoft T., González Hernández I., Lindsey C., Hill F., eds., Asteroseismology and the Solar-Stellar Connection, p. 567

Michel E., Baglin A., Weiss W. W. et al. First asteroseismic results from CoRoT, 2008, Comm in Astero, 157, 69

Miglio A., Brogaard K., Stello D. et al. Asteroseismology of old open clusters with Kepler: direct estimate of the integrated red giant branch mass-loss in NGC 6791 and 6819, 2012, MNRAS, 419, 2077

Miglio A., Chiappini C., Morel T. et al. Galactic archaeology: mapping and dating stellar populations with asteroseismology of red-giant stars, 2013, MNRAS, 429, 423

Miglio A., Girardi L., Rodrigues T. S. et al. Solar-like oscillating stars as standard clocks and rulers for Galactic studies, 2014, ArXiv e-prints

Miglio A., Montalbán J., Eggenberger P. et al., 2009, in American Institute of Physics Conference Series, Vol. 1170, American Institute of Physics Conference Series, Guzik J. A., Bradley P. A., eds., Asteroseismology of red-clump stars with CoRoT and Kepler, pp. 132–136

Miglio A., Montalbán J., Noels A., 2012, Red Giants as Probes of the Structure and Evolution of the Milky Way, Asteroseismology of Red Giants as a Tool for Studying Stellar Populations: First Steps, Springer, p. 11

Milliman K. E., Mathieu R. D., Geller A. M. et al. WIYN Open Cluster Study. LX. Spectroscopic Binary Orbits in NGC 6819, 2014, AJ, 148, 38

Montalbán J., Miglio A., Noels A. et al. Testing Convective-core Overshooting Using Period Spacings of Dipole Modes in Red Giants, 2013, ApJ, 766, 118

Monteiro H., Dias W. S., Caetano T. C. Fitting isochrones to open cluster photometric data. A new global optimization tool, 2010, A&A, 516, A2

Mosser B., 2013, in European Physical Journal Web of Conferences, Vol. 43, European Physical Journal Web of Conferences, Red giant seismology: Observations, p. 3003

Mosser B., Belkacem K., Goupil M.-J. et al. Red-giant seismic properties analyzed with CoRoT, 2010, A&A, 517, A22

Mosser B., Maillard J. P., Mekarnia D. et al. New limit on the p-mode oscillations of Procyon obtained by Fourier transform seismometry, 1998, A&A, 340, 457

Nordlund A., Spruit H. C., Ludwig H.-G. et al. Is stellar granulation turbulence?, 1997, A&A, 328, 229

Oliveira A. F., Monteiro H., Dias W. S. et al. Fitting isochrones to open cluster photometric data. III. Estimating metallicities from UBV photometry, 2013, A&A, 557, A14

Pietrinferni A., Cassisi S., Salaris M. et al. A Large Stellar Evolution Database for Population Synthesis Studies. I. Scaled Solar Models and Isochrones, 2004, ApJ, 612, 168

Platais I., Cudworth K. M., Kozhurina-Platais V. et al. A New Look at the Old Star Cluster NGC 6791, 2011, ApJ, 733, L1

Ramírez I., Meléndez J. The Effective Temperature Scale of FGK Stars. II. T_{eff}:Color:[Fe/H] Calibrations, 2005, ApJ, 626, 465

Retter A., Bedding T. R., Buzasi D. L. et al. Oscillations in Arcturus from WIRE Photometry, 2003, ApJ, 591, L151

Roth G. D., 2009, Handbook of Practical Astronomy, Handbook of Practical Astronomy, Springer

Ryan S. G., Norton A. J., 2010, Stellar Evolution and Nucleosynthesis, Stellar Evolution and Nucleosynthesis. Cambridge University press

Salaris M., Cassisi S., 2005, Evolution of Stars and Stellar Populations, Evolution of Stars and Stellar Populations. John Wiley and Sons Inc

Sandquist E. L., 2013, in American Astronomical Society Meeting Abstracts, Vol. 221, American Astronomical Society Meeting Abstracts #221, Precision Age Determination for Kepler Open Clusters Using Eclipsing Binaries, p. 321.03

Schou J., Buzasi D. L., 2001, in ESA Special Publication, Vol. 464, SOHO 10/GONG 2000 Workshop: Helio- and Asteroseismology at the Dawn of the Millennium, Wilson A., Pallé P. L., eds., Observations of p-modes in α Cen, pp. 391–394

Silva Aguirre V., Casagrande L., Basu S. et al. Determining distances using asteroseismic methods, 2013, Astronomische Nachrichten, 334, 22

Silva Aguirre V., Casagrande L., Basu S. et al. Verifying Asteroseismically Determined Parameters of Kepler Stars Using Hipparcos Parallaxes: Self-consistent Stellar Properties and Distances, 2012, ApJ, 757, 99

Soderblom D. R. The Ages of Stars, 2010, ARA&A, 48, 581

Stahler S. W., Palla F., 2004, The Formation of Stars, The Formation of Stars, WILEY-VCH Verlag GmbH & Co. KGaA

Steffen J. H., Fabrycky D. C., Ford E. B. et al., 2011, in Bulletin of the American Astronomical Society, Vol. 43, American Astronomical Society Meeting Abstracts #217, Kepler Systems That Show Multiple Transiting Objects

Stello D., Basu S., Bedding T. R. et al. Solar-like oscillations in cluster stars, 2010a, Astro No, DeNachrichten, 331, 985

Stello D., Basu S., Bruntt H. et al. Detection of Solar-like Oscillations from Kepler Photometry of the Open Cluster NGC 6819, 2010b, ApJ, 713, L182

Stello D., Bruntt H., Kjeldsen H. et al. Multisite campaign on the open cluster M67 - II. Evidence for solar-like oscillations in red giant stars, 2007, MNRAS, 377, 584

Stello D., Bruntt H., Preston H. et al. Oscillating K Giants with the WIRE Satellite: Determination of Their Asteroseismic Masses, 2008, ApJ, 674, L53

Stello D., Chaplin W. J., Basu S. et al. The relation between $\Delta\nu$ and ν_{max} for solar-like oscillations, 2009, MNRAS, 400, L80

Stello D., Compton D. L., Bedding T. R. et al. Non-radial Oscillations in M-giant Semi-regular Variables: Stellar Models and Kepler Observations, 2014, ApJ, 788, L10

Stello D., Gilliland R. L. Solar-like Oscillations in a Metal-poor Globular Cluster with the Hubble Space Telescope, 2009, ApJ, 700, 949

Stello D., Huber D., Bedding T. R. et al. Asteroseismic Classification of Stellar Populations among 13,000 Red Giants Observed by Kepler, 2013, ApJ, 765, L41

Stello D., Huber D., Kallinger T. et al. Amplitudes of Solar-like Oscillations: Constraints from Red Giants in Open Clusters Observed by Kepler, 2011a, ApJ, 737, L10

Stello D., Meibom S., Gilliland R. L. et al. An Asteroseismic Membership Study of the Red Giants in Three Open Clusters Observed by Kepler: NGC 6791, NGC 6819, and NGC 6811, 2011b, ApJ, 739, 13

Stetson P. B., Bruntt H., Grundahl F. Homogeneous Photometry. III. A Star Catalog for the Open Cluster NGC 6791, 2003, PASP, 115, 413

Street R. A., Horne K., Lister T. A. et al. Variable stars in the field of open cluster NGC 6819 - II, 2005, MNRAS, 358, 795

Suárez J. C., Garrido R., Balona L. A., Christensen-Dalsgaard J., eds., 2013, Advances in Solid State Physics, Vol. 31, Stellar Pulsations. Springer

Tarrant N. J., Chaplin W. J., Elsworth Y. et al. Asteroseismology of red giants: photometric observations of Arcturus by SMEI, 2007, MNRAS, 382, L48

Tarrant N. J., Chaplin W. J., Elsworth Y. et al. Oscillations in β Ursae Minoris. Observations with SMEI, 2008,
aap, 483, L43

Tassoul M. Asymptotic approximations for stellar nonradial pulsations, 1980, ApJS, 43, 469

Tassoul M. Second-order asymptotic approximations for stellar nonradial acoustic modes, 1990, ApJ, 358, 313

Torres G. On the Use of Empirical Bolometric Corrections for Stars, 2010, AJ, 140, 1158

Ulrich R. K. Determination of stellar ages from asteroseismology, 1986, ApJ, 306, L37

van den Berg M., Verbunt F., Tagliaferri G. et al. A Chandra X-Ray Study of the Interacting Binaries in the Old Open Cluster NGC 6791, 2013, ApJ, 770, 98

Verner G. A., Elsworth Y., Chaplin W. J. et al. Global asteroseismic properties of solar-like oscillations observed by Kepler: a comparison of complementary analysis methods, 2011, MNRAS, 415, 3539

Verner G. A., Roxburgh I. W. A power-spectrum autocorrelation technique to detect global asteroseismic parameters, 2011, Arxiv e-printe-prints

Walker G., Matthews J., Kuschnig R. et al. The MOST Asteroseismology Mission: Ultraprecise Photometry from Space, 2003, PASP, 115, 1023

Wang G., Jiang X., Wang H. et al., 2014, in Society of Photo-Optical Instrumentation Engineers (SPIE) Conference Series, Vol. 9145, Society of Photo-Optical Instrumentation Engineers (SPIE) Conference Series, Introduction of Chinese SONG telescope, p. 10

White T. R., Bedding T. R., Gruberbauer M. et al. Solving the Mode Identification Problem in Asteroseismology of F Stars Observed with Kepler, 2012, ApJ, 751, L36

Worthey G., 2010, in Bulletin of the American Astronomical Society, Vol. 42, American Astronomical Society Meeting Abstracts #215, Color Color Relations and NGC 6791, p. 425.13

Wu T., Li Y., Hekker S. Asteroseismic Study on Cluster Distance Moduli for Red Giant Branch Stars in NGC 6791 and NGC 6819, 2014, ApJ, 786, 10

Yang S.-C., Sarajedini A., Deliyannis C. P. et al. WIYN Open Cluster Study LII: Wide-field CCD Photometry of the Old Open Cluster NGC 6819, 2013, ApJ, 762, 3